I. ANTIMICROBIAL PHOTODYNAMIC INACTIVATION TARGETING MULTIDRUG RESISTANCE WITH GALLIUM-HEMOGLOBIN-COATED SILVER NANOPARTICLES II. SYNTHESIS AND PROPERTIES OF MAGNETIC GOLD NANOPARTICLES

by

Lu Lin

A Dissertation

Submitted to the Faculty of Purdue University

In Partial Fulfillment of the Requirements for the degree of

Doctor of Philosophy

Department of Chemistry

West Lafayette, Indiana

August 2019

THE PURDUE UNIVERSITY GRADUATE SCHOOL
STATEMENT OF COMMITTEE APPROVAL

Dr. Alexander Wei, Chair

Department of Chemistry

Dr. Chittaranjan Das

Department of Chemistry

Dr. Andy Tao

Department of Chemistry

Dr. Gregory Knipp

Department of Industrial and Physical Pharmacy

Approved by:

Dr. Christine Hrycyna

Head of the Graduate Program

In Loving Memory of My Grandfather

ACKNOWLEDGMENTS

I would like to acknowledge my committee members for their guidance during graduate school, especially my research advisor Prof. Alex Wei for giving me the opportunity to gain exposure to different areas of research.

A very special gratitude goes out to all the collaborators I have worked with: Dr. Naveen Kadasala, Dr. Ana Morales, Dr. Christopher Gilpin, Prof. Marisol Sepulveda, Dr. Mayank Srivastava, Dr. Jiejun Gao, Dr. Neil Dilley, Prof. Bennett Elzey, Prof. Mohamed Seleem and Nader Abutaleb. With a special mention to the following: Arlene Rothwell, Robert Seiler, Laurie Mueller, Paul Bower, Sandra Torregrosa-Allen, Melanie Currie, Kathy Ragheb, Prof. Paul Robinson, Dr. Uma Aryal, Vicki Hedrick, Dr. Andy Schaber, Prof. Haiyan Wang, Dr. Jian Jie, Prof. Kavita Shah and Dr. Keith Viccaro for their unfailing technical support and assistance.

I am also grateful to the encouragement and guidance I received from Prof. Sharon Akabas and Prof. Nataki Douglas while I was applying for graduate school.

My sincere thanks to my fellow lab mates from Wei group. You guys were always there in WTHR 430 to cheer me up during the tough times in graduate school. Sharing laboratory with all of you during last four years is one of the most memorable experiences in my life.

Finally, last but foremost, to Steven, the love of my life, and all my family in US and back home in China. Your love and support are the ultimate motivation to keep me going and remain strong.

TABLE OF CONTENTS

LIST OF TABLES

LIST OF SCHEMES

LIST OF FIGURES

ABSTRACT

Author: Lin, Lu. PhD
Institution: Purdue University
Degree Received: August 2019
Title: I. Gallium-hemoglobin Coated Silver Nanoparticles for Antimicrobial Photodynamic Therapy Against Bacterial Pathogens II. Synthesis and Properties of Magnetic Gold Nanoparticles
Committee Chair: Alexander Wei

I. Gallium-hemoglobin Coated Silver Nanoparticles for Antimicrobial Photodynamic Therapy Against Bacterial Pathogens

One of the mechanisms for bacterial pathogens' hemin acquisition is through cell-surface hemin receptors (CSHRs), which are responsible for rapid hemin recognition. GaPpIX, as a hemin analog, can be rapidly taken up by CSHR-expressing bacteria, such as *Staphylococcus aureus* (*S.aureus)*. Previous works shown that GaPpIX has aPDI activity at micromolar level of concentration following 10 seconds of 405-nm light exposure using LED array. The photosensitizing ability of GaPpIX can be further enhanced by incorporating with hemoglobin (GaHb) and 10 nm silver nanoparticles (AgNP). The results suggested a higher aPDI activity of GaHb-AgNP than any of its components against MRSA strains and neglectable cytotoxicity against keratinocytes. GaHb-AgNPs were also found having aPDI activity against intracellular MRSA and *Mycobacterium abscessus* but not effective against *S. aureus* biofilm. GaHb-AgNPs have no significant toxicity toward macrophages with concentrations lower than 22.64 μg/mL.

II. Synthesis and Properties of Magnetic Gold Nanoparticles

Superparamagnetic gold nanoparticles support hybrid magnetic and plasmonic properties that can be exploited for a variety of applications. In this paper we present new insights on the

synthesis of magnetic gold nanoparticles (MGNPs) with an emphasis on efficiency, scalability, and waste reduction, supported by a comprehensive analysis of their physical and materials properties. Aqueous suspensions of colloidal Fe_3O_4 are conditioned with 5-kDa polyethylene glycol and L-histidine to mediate the nucleation and growth of gold by a mild reducing agent. Isotropic MGNPs on the order of 100 nm can be synthesized using scalable reaction conditions with Au:Fe mole ratios as low as 1:2 and cleansed with generally regarded as safe (GRAS) chemicals for the removal of residual iron oxide. High-resolution energy-dispersive x-ray imaging of individual MGNCs revealed these to be ultrafine composites of gold and SPIO rather than core–shell structures. The attenuated total reflectance infrared (ATR-IR) spectroscopy and Raman spectroscopy indicated that the cleansing step does change the optical properties of the synthesized MGNPs. Magnetometry of MGNCs in bulk powder form confirmed their superparamagnetic nature, with bulk moments between 6 to 7 emu/g.

CHAPTER 1. ANTIMICROBIAL PHOTODYNAMIC INACTIVATION TARGETING MULTIDRUG RESISTANCE WITH GALLIUM-HEMOGLOBIN-COATED SILVER NANOPARTICLES

This chapter is based on our work published on *ACS Infect. Dis. 2018, 4, 1564−1573*

1.1 Introduction

1.1.1 Multidrug-Resistant Bacteria

The rise of drug-resistant bacteria is a growing challenge to biosecurity and public health. The Infectious Diseases Society of America (IDSA) recognizes antimicrobial resistance as "one of the greatest threats to human health worldwide".[1] If the bacteria survive an encounter with antibiotics, they are given the opportunity to develop resistance by adapting cell structure or metabolism to neutralize the antibiotic in the future. Bacteria can acquire resistance by modification of present genetic material or by gaining new genetic material.[2] Once resistance is acquired, it can also share its genes vertically with descendent bacteria or horizontally with unrelated bacteria.[2] More strains of bacteria have become antibiotic-resistant, and some have even become resistant to multiple antibiotics and chemotherapeutic agents. The emergence of multidrug-resistant (MDR) bacteria is posing a critical threat to all aspects of modern medicine. Firstly, patients infected with MDR bacteria tend to have far worse outcomes compared to the patients infected with more susceptible organisms. As a result, MDR bacteria threaten to compromise many modern therapies such as cancer care, organ transplantation, and surgical procedures.[3] Secondly, these infections are usually associated with enormous additional cost. In the US, the added costs of infections caused by MDR bacteria are estimated to be at least $21 billion per year more than that due to susceptible organisms.[1]

There are many reasons for the rise of drug-resistant bacteria, such as inappropriate or excessive prescription of antibiotics and the overuse of antibiotics on livestock. These factors induce microbes to adopt various mechanisms to counter external chemical threats. Some strains have become resistant to most first-line antibiotic agents. The most famous example is the methicillin-resistant *Staphylococcus aureus* (MRSA). Many MRSA strains are resistant not only to methicillin but also to amoxicillin, penicillin, oxacillin, and many other common antibiotics.[1] MRSA is also found to be resistant to disinfectants, and therefore is a major source of hospital-acquired infections that are responsible for over 11,000 deaths and 80,000 infections every year.[1] Vancomycin has been resurrected as a final defense against MRSA infections, however vancomycin-resistant *Staphylococcus aureus* (*S. aureus*) is now quite common and there are almost no alternative treatment options available.[1, 4-5]

Direct resistance to antibiotics is not the only mechanism for bacteria like *S. aureus* to survive against antibiotic therapies. Although *S. aureus* is considered to be an extracellular pathogen, it is becoming increasingly apparent that intracellular reservoirs of *S. aureus* are potentially responsible for relapses of infection after antimicrobial therapy.[6-7] Many *in vitro* studies have shown that *S. aureus* is capable of invading a number of non-professional phagocytic cells, as well as keratinocytes, fibroblasts, endothelial, and epithelial cells.[8-12] Professional phagocytes such as neutrophils, macrophages and dendritic cells are designed to ingest and kill microbes. *In vitro* studies confirmed that *S. aureus* is one of several types of microbial pathogens that can induce the expression of antiapoptotic genes and employ cytoprotective mechanisms to survive phagocytosis by neutrophils and macrophages.[13-14] The role of the host cells in this process is to provide a refuge that promotes intracellular growth of *S. aureus,* and contributing to its dissemination during a relapse infection until they are sacrificed through apoptosis.[15] When translocated inside the

mammalian cells, bacteria are able to evade the host immune response as well as many antibiotics due to low cell permeability.[16] These challenges have motivated efforts to target intracellular bacteria using vehicles like liposomes and nanoparticles to carry bactericidal agents.[17-18]

Another important contribution to microbial survival in hostile environments is the capability of pathogens to form biofilms. A biofilm is a sessile microbial community in which cells are attached to a surface or to other cells, embedded in a protective extracellular biopolymer. It was observed that bacterial cells inside the biofilm are thousands of times more resistant to conventional antibiotics than free-living (planktonic) forms.[19] Biofilm growth plays an important role during infection by evading several clearance mechanisms by the host. Examples of failed clearance strategies include antimicrobial agents, shear stress, host phagocytic elimination, and host radical and protease defense. In contrast to inheritable antibiotic resistance mechanisms, biofilm-associated antibiotic resistance is due to susceptible bacteria having a dormant phenotype, which decreases their sensitivity.[20] While low metabolic rates may partially explain the antimicrobial resistance of biofilm-forming bacteria, the biofilm matrix may also simply impede drug access to actively growing cells by acting as a diffusion barrier.[21] For example, chlorine, a commonly used disinfectant, did not reach >20% of the bulk media's initial concentration within a mixed *Klebsiella pneumoniae* and *Pseudomonas aeruginosa* biofilm, as measured by a chlorine-detecting microelectrode. Moreover, the penetration profile suggested that chlorine was neutralized within the matrix. Biofilm development also has the potential for seeding dispersal; detached micro-colonies may migrate from the original infection site to uninfected regions of the host.[22] As such, biofilm growth is an enduring source of bacteria that can persist in the presence of antimicrobial agents and the host immune response, while enabling continuous dissemination. Therefore, there is a need for effective treatment options to battle biofilm-associated infections.

Rapid growing mycobacterial (RGM) species are increasingly being recognized as vector of various superficial and deep infections in human beings. One species that is frequently isolated from clinical skin specimens is *Mycobacterium abscessus* (*M. abscessus*).[23] *M. abscessus* is ubiquitous in soil and water, and is the most common non-tuberculous mycobacterium that can cause complicated skin and soft tissue infections (SSTIs).[24] Many strains of *M. abscessus* not only resist antibiotics, but also have high tolerance to disinfectants and can cause of postsurgical and postprocedural infections.[25-26] The drug resistance of *M. abscessus* arises from both intrinsic and acquired resistance, and has become a serious health issue that is in need for effective methods of treatment.[26]

1.1.2 Antibacterial Photodynamic Inactivation

As more bacteria strains have become resistant to antibiotics, there are fewer antibiotic treatments available, driving the need to find novel approaches to combat MDR bacteria. Antibacterial photodynamic inactivation (aPDI) has attracted increasing attention because it offers several potential advantages over antibiotics. aPDI utilizes a photochemical mechanism for killing or inactivating microorganisms, based on the conversion of molecular oxygen into excited-state singlet oxygen ($^1O_2$) or reactive oxygen species (ROS) using exogenous compounds known as photosensitizers (PS). Firstly, aPDI can have low cytotoxicity if the PS is taken up preferentially by the target cell relative to non-target cells, with irradiation confined to the infected area. Secondly, $^1O_2$ is not affected by most drug resistance mechanisms.[27] This may be because its high reactivity short lifetime does not provide the bacteria enough time to develop resistance. Lastly, ROS generated by aPDI can attack multiple cell structures and disrupt different metabolic pathways.[28] Therefore, aPDI has great potential to circumvent MDR with low collateral toxicity.

In aPDI, cell damage and death are the results of oxidative stress that is induced by irradiation with light at a resonant wavelength, usually within the visible wavelength range (400 nm to 700 nm), corresponding to a light penetration depth from 0.1 cm to 1 cm.[29-32] PS is irradiated to generate excited-state singlet (^{1}PS) in or on the surface of the bacteria, and can return to the ground state by fluorescence or heat emission. However, the excited-state PS can also undergo intersystem crossing to a longer-lived triplet state (^{3}PS), from which $^1O_2$ or ROS are formed.[29]

There are two types of photochemical mechanisms for converting oxygen into $^1O_2$ or ROS (Figure 1.1). Type I reactions generate radicals by electron transfer from ^{3}PS to molecular oxygen, which can react with other molecules and give rise to cytotoxic ROS. In type II reactions, ^{3}PS reacts with oxygen (a ground-state triplet) by energy transfer to generate the highly reactive singlet oxygen. Type I and type II reactions are believed to happen simultaneously, and the ratio of occurrence between the two depends on the type of PS and its microenvironment.[33] However, because singlet oxygen has a short lifetime in biological systems and a short radius of action (0.02 μm), the type II reaction usually induces localized damage, which makes it suitable for treating bacterial infections with minimal harm to nearby cells or tissues.[34]

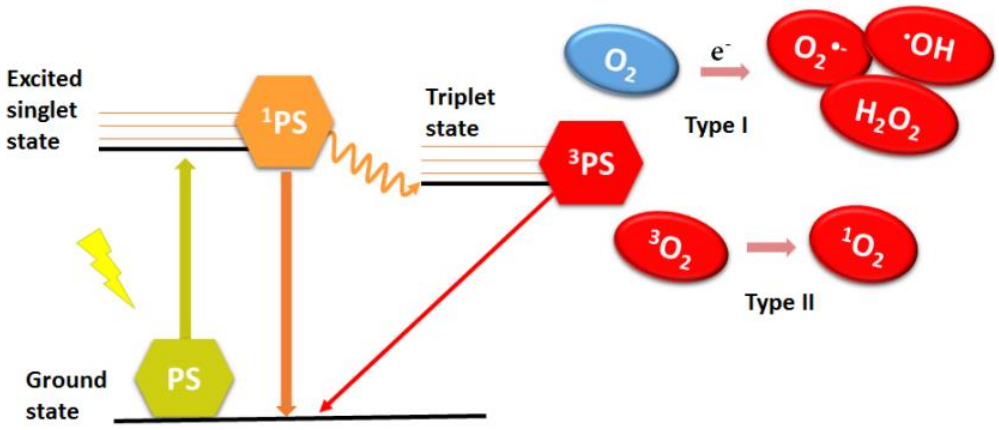

Figure 1.1. Type I and II mechanisms of photodynamic inactivation. Adapted from Liu et al. [33]

1.1.3 Photosensitizers

Many PS have been investigated as agents for photodynamic therapy. Photofrin and hematoporphyrin (Figures 1.2a and b) are the first generation of PS approved for medical use.[34] Photofrin has low dark toxicity and is widely used, but can cause skin photosensitivity that requires patients to avoid strong sunlight for weeks.[35] Second-generation photosensitizers are capable of generating $^1O_2$ with higher efficiency, such as verteporfin, texaphyrin, and temoporfin (Figure 1.2c-e).[34]

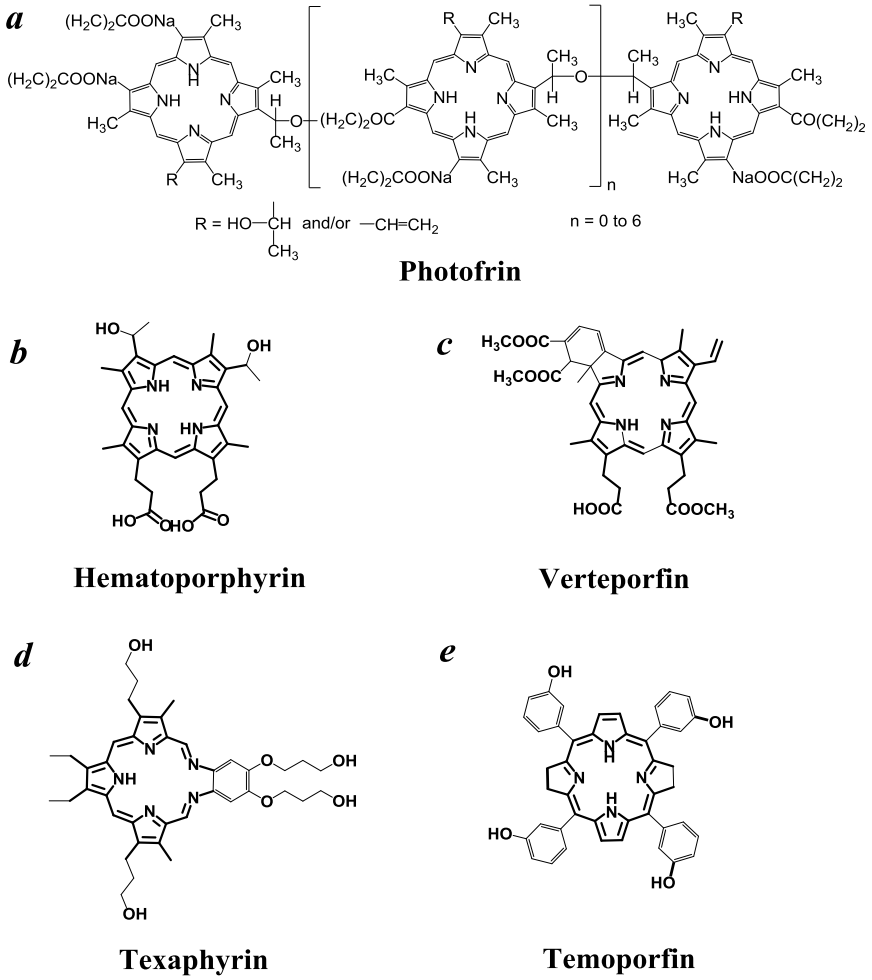

Figure 1.2. Molecular structures of (a) photofrin, (b) hematoporphyrin, (c) verteporfin, (d) texaphyrin and (e) temoporfin.

PS have been explored extensively for antibacterial PDI. For example, treatment of wild-type *Staphylococcus aureus* and MRSA with Zn(II)–phthalocyanine (0.1 μM; Figure 1.3a) and irradiation at 600–700 nm (15 J/cm^2) resulted in a 4–5 $\log_{10}$ reduction in each case.[36] The efficiency and selectivity of aPDI treatment was unaffected by the presence of serum proteins. In another study, methylene blue (Figure 1.3b) was tested on antibiotic-resistant biofilm harvested from the endotracheal tube of infected patients.[37] Over 99.9% ($P < 0.005$) reduction in biofilm was observed after irradiation at 664 nm (216 J/cm^2) in the presence of methylene blue (500 μg/mL).[37] Methylene blue (50 μg/mL, 163.8 J/cm^2) was also effective in inactivating both Gram-positive and negative bacteria, especially periodontopathic bacteria.[34, 38] Treatment of *S. aureus* and MRSA with Ru(II)-based PS (0.3–12 μM; Figure 1.3c) and irradiation with 530 nm light (90 J/cm^2) resulted in over 7 $\log_{10}$ reduction (> 99.99999%) under both normoxic and hypoxic conditions.[39]

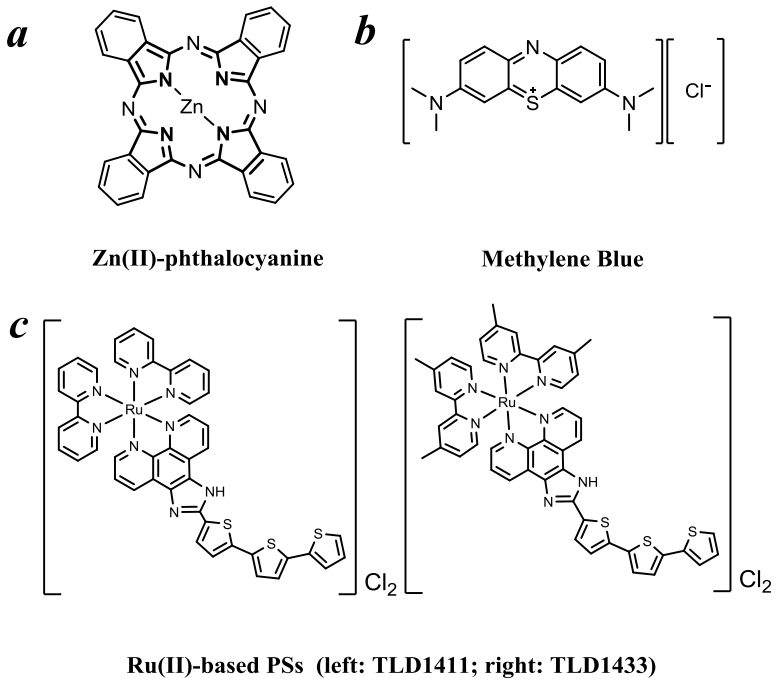

Figure 1.3. Molecular structures of (a) Zn(II)–phthalocyanine, (b) methylene blue and (c) Ru(II)-based PS (left: TLD 1411; right: TLD1433) .

Porphyrin and its derivatives have shown exceptional broad spectrum of aPDI. For example, a study compared chlorin e6 with *meso*-tetrahydroporphyrin (Figure 1.4a and b) by testing both of them on Gram-positive and negative bacteria. The results shown that only the porphyrin derivative was effective in both types of bacteria.[40] Another derivative, tetra(*N*-methyl-4-pyridyl)porphyrin (TMPyP), caused over 6 $\log_{10}$ reduction (99.9999%) in Gram-positive strains of *S.aureus* (MSSA and MRSA), and two Gram-negative strains of *E.coli* and *P.aeruginosa.*[28]

5-aminolevulinic acid (ALA; Figure 1.4d) is the precursor in porphyrin synthesis in both eukaryotes and bacteria.[41-42] ALA has been applied as a prodrug for the in situ production of protoporphyrin IX (PpIX) for aPDI.[43] ALA has the advantage of being administered more easily than PpIX because of its low molecular weight and solubility in water.[43-44] However, ALA was also reported to cause pain during treatment, and requiring prolonged incubation time (4–6 hours) for its conversion into PpIX before aPDI could be administered.[44-45]

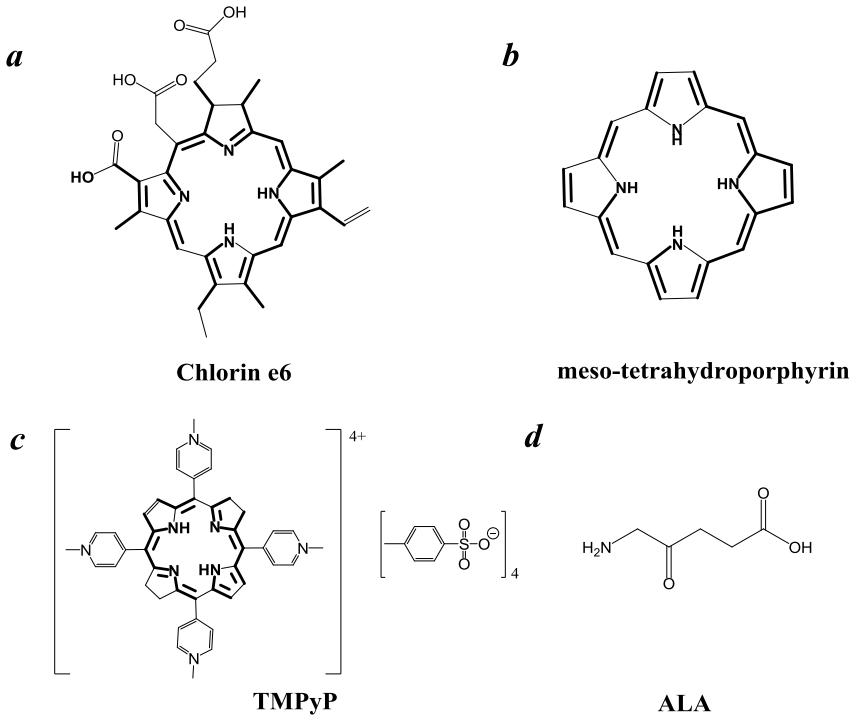

Figure 1.4. Molecular structures of (a) chlorin e6, (b) meso-tetrahydroporphyrin, (c) TMPyP and (d) ALA.

1.1.4 Iron-Dependent Uptake of Hemin and Ga(III)-Protoporphyrin IX (GaPpIX)

Porphyrins are involved in many biological processes in living organisms.[46] Naturally occurring porphyrins are mostly derived from PpIX (Figure 1.5). Metallated protoporphyrins that mimic hemin (FePpIX), a photochemically inactive species, are more effective than non-metallated porphyrins for aPDI. Stojiljkovic found that gallium–substituted protoporphyrin (GaPpIX) has the lowest MIC against *S. aureus* compared with PpIX and other metal complexes (FePpIX, MnPpIX, MgPpIX and ZnPpIX).[47] There are many more studies on the antibacterial activity of GaPpIX, however there is hardly any work on GaPpIX as an aPDI agent.[48-49] In this chapter we are focusing on the aPDI activities of GaPpIX, its complex with hemoglobin (GaHb), and also with Ag nanoparticles (GaHb-AgNP).

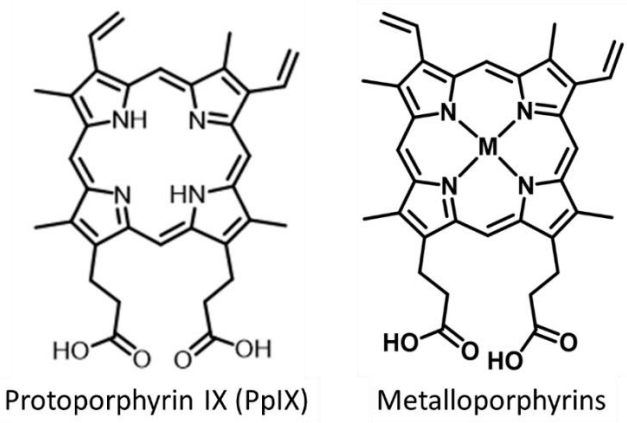

Figure 1.5. Molecular structures of protoporphyrin IX (PpIX) and metalloporphyrin

The heme molecule is one of the most important enzyme co-factors in nature. It plays key roles in oxygen transport, nitric oxide synthesis, and electron transfer.[50-54] PpIX coordinates with an Fe(II) atom at the center, which is vital for heme's electron transfer and redox properties.[42] Hemin, the oxidized from of heme (Fe(III)PpIX), serves as an iron source for many bacterial pathogens, and are taken up by Gram-positive and Gram-negative bacteria through specific hemin acquisition

pathways.[51, 55-56] Bacteria can be divided into two types according to their heme acquisition mechanisms. Type 1 bacteria are known to express cell-surface hemin receptors (CSHRs), which support the direct acquisition of hemin. Type 2 bacteria can acquire heme by the secretion and recovery of extracellular proteins called hemophores, which introduces additional steps to the hemin acquisition process (Figure 1.6).[57-58] The hemophore harvesting strategy enables bacteria to sample a larger volume for scavenging hemin, but additional time is required for hemophore release and retrieval, and is a slower process compared to the Type 1 pathway.

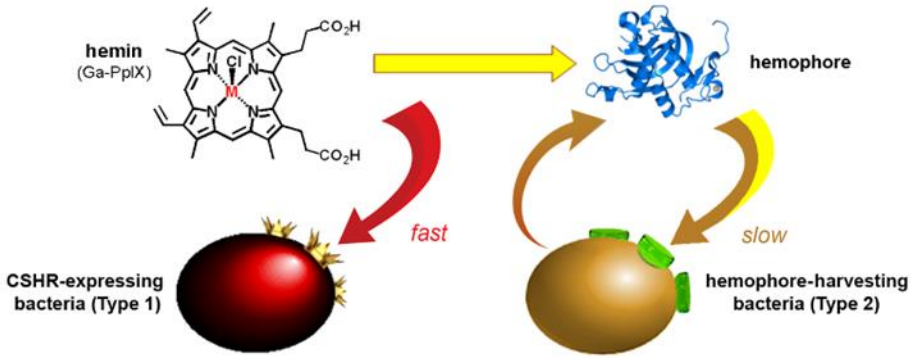

Figure 1.6. CSHR-expressing bacteria (Type 1) and hemophore-harvesting bacteria (Type 2).[58-59]

Previous work in our laboratory has shown that when hemin derivatives are conjugated to glass slides, select Gram-positive bacteria such as *S. aureus* and *Bacillus anthracis* could be captured and detected within 15 min, while most other bacteria took over 30 min before a signal would be attained.[58] The reason for the significant differences in capture rate is that *S. aureus* and *B. anthracis* are both Type 1 bacteria, and can acquire hemin directly using the receptor proteins expressed on their outer cell walls. Both species produce iron-regulated surface determinants (Isd), a family of CSHRs which are believed to be the main factors for rapid hemin uptake (Figure 1.7).[42, 60-61]

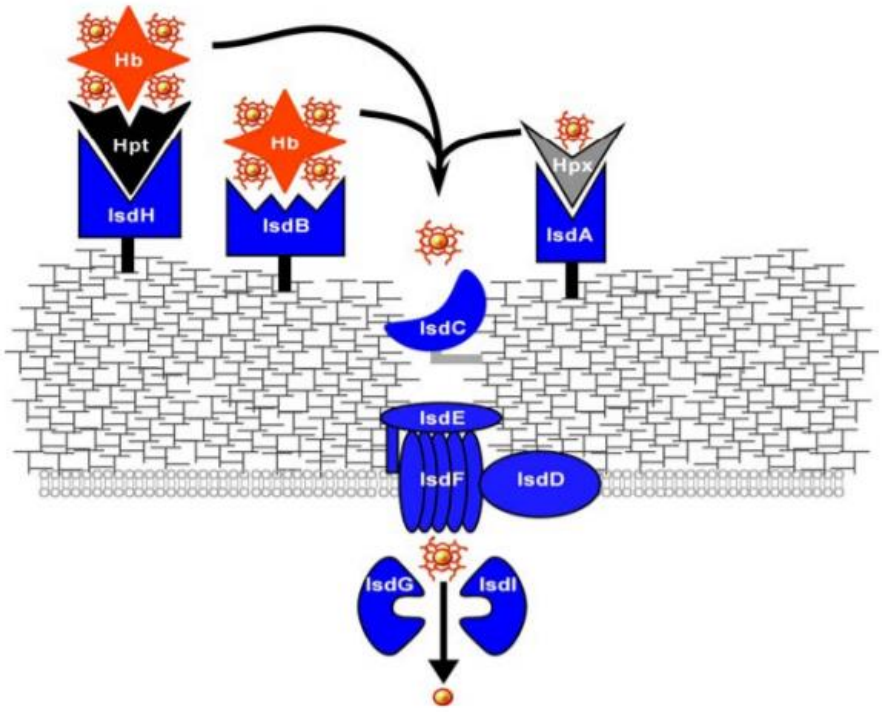

Figure 1.7. A model for Isd-mediated heme-iron transport and utilization by *S. aureus.* Adapted from Skaar *et al.*[61]

A study in our laboratory further confirmed that the rapid uptake of GaPpIX by Type 1 bacteria such as *S. aureus* is regulated by CSHRs. 405–nm excitation of GaPpIX can produce a strong luminescence with emission bands that are blue shifted relative to those of PpIX (Figure 1.8), which made it possible to visualize GaPpIX uptake through confocal fluorescence microscopy. *S. aureus* (PC1203) was compared against *Yersinia enterocolitica* (WA-314), a Type 2 bacteria that utilizes the hemophore HasA to capture and deliver the heme to the surface receptor HemR.[58-59] Due to the indirect type 2 uptake mechanism, *Y. enterocolitica* was much slower than *S. aureus* in taking up GaPpIX. After being incubated with 8.8 μM GaPpIX for different time intervals, the bacteria were examined using confocal microscopy, which revealed *S. aureus* to be rapidly and strongly labelled by GaPpIX within the first 15 min, whereas the labeling of *Y. enterocolitica* was initially weak and gradually increased over time (Figure 1.9).[62]

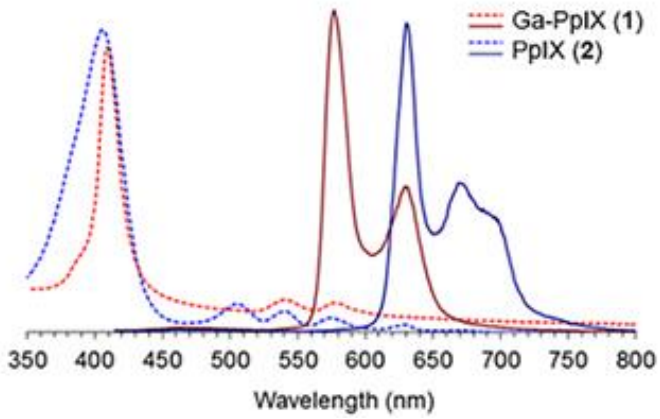

Figure 1.8. Absorbance (---) and emission (—) spectra for GaPpIX (8 μM in DMSO, red) with comparison to PpIX (blue).[62]

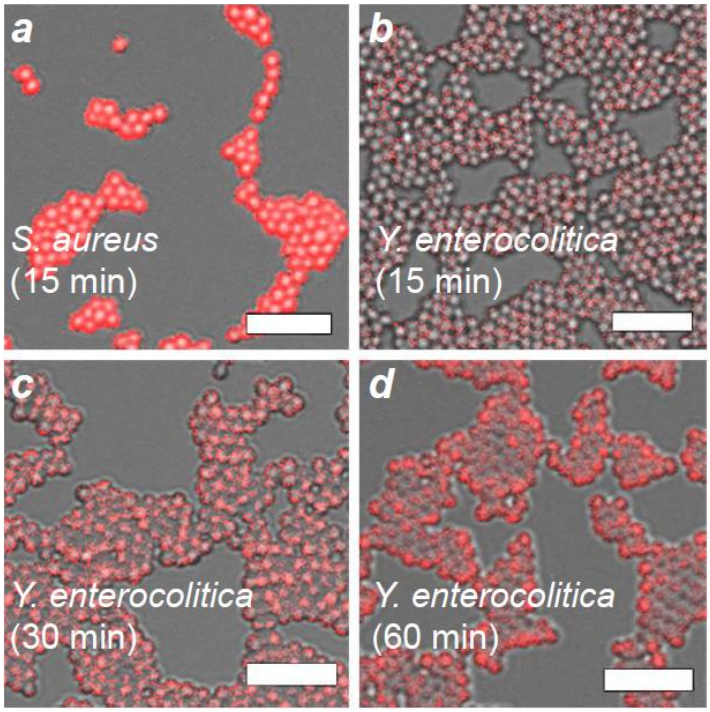

Figure 1.9. Confocal fluorescence microscopy of GaPpIX uptake (bar = 5 μm). (a) *S. aureus* (PC1203) after 15 min exposure; (b–d) *Y. enterocolitica* (WA-314, ovoid form) after 15, 30, and 60 min incubation.[62]

We further explored the uptake rate of GaPpIX by *S. aureus* using flow cytometry. *S. aureus* cell suspensions were cultured in iron-deficient media before being mixed with GaPpIX in PBS.

The mixtures were incubated at room temperature for fixed time intervals between 10 s to 40 min. followed by fixation using 4 % paraformaldehyde and subjected to flow cytometry (Figure 1.10). During the analysis, the bacteria population was identified based on cell size (forward scatter) and granularity (side scatter). The results showed that there was no significant change in fluorescence density between each data point, which indicates no fluorescence buildup in the bacteria over time. Our observation suggests that the uptake of GaPpIX by CSHRs is likely diffusion-limited. Our results did not provide evidence for activation of bacterial efflux pumps, a mechanism for bacteria to protect themselves from acute iron toxicity by removing excessive hemin, within the time scale of aPDI.[63]

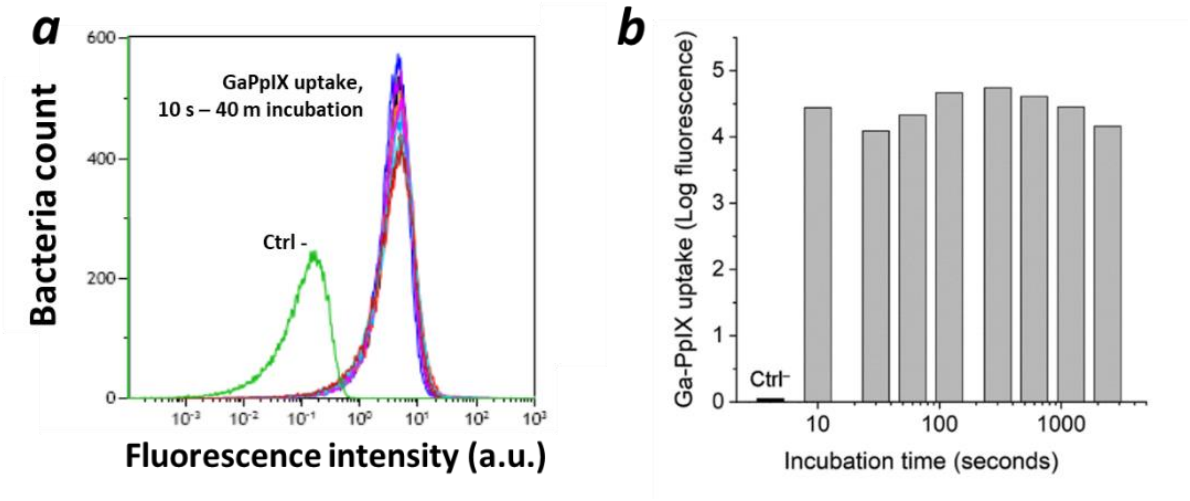

Figure 1.10. Flow cytometry of *S. aureus* treated with GaPpIX. (a) Spectra of fluorescent intensity; (b) fluorescence intensity as a function of incubation time. Ctrl⁻ means equal volume of PBS without GaPpIX.

The Isd family of receptor proteins (the probable CSHRs for *S. aureus*) are known to be regulated by the ferric uptake regulator (*fur)* gene. Iron-deficient conditions induce *fur* expression, resulting in elevated Isd expression.[64-65] We confirmed the increased expression of CSHR by culturing *S. aureus* in iron-limited conditions, which resulted in much greater uptake of GaPpIX

compared to *S. aureus* cultured in standard conditions (Figure 1.11).[62] The iron-deficient condition is clinically relevant because humans and other organisms sequester iron to limit acquisition by bacterial pathogens, a response called nutritional immunity, which is an effective antimicrobial strategy that restricts bacterial growth.[42] For this reason, bacteria have developed tactics such as hemin harvesting to overcome iron deficiency, giving rise to opportunities for exploiting hemin uptake for pathogen-specific aPDI.

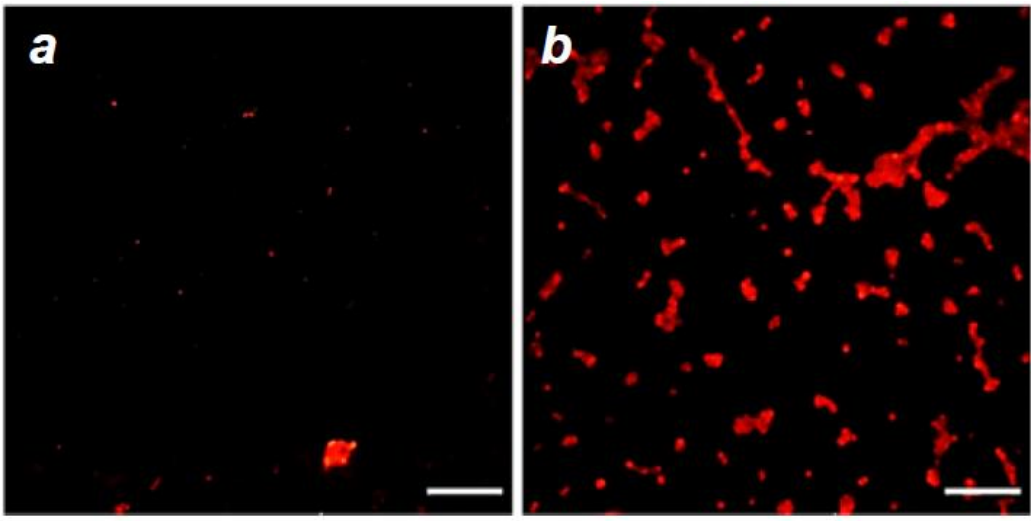

Figure 1.11. Fluorescence images of *S. aureus* (PC1203) treated with GaPpIX (bar = 10 μm). Bacteria were cultured in either (*a*) standard media or (*b*) iron-challenged media prior to exposure to Ga-PpIX for 15 min, with the latter showing stronger fluorescence intensities.[62]

1.1.5 GaPpIX has Rapid and Robust aPDI Activity

Earlier work in our lab has shown that when using visible light, GaPpIX is an effective and fast-acting aPDI agent against laboratory strain of *S. aureus* (PC1203) and also clinical isolates of MRSA. The aPDI potency of GaPpIX was established using a light-emitting diode (LED) array with monochromatic emission at 405-nm (1.40 J/cm^2) to irradiate bacteria treated with GaPpIX, TMPyP, and PpIX as reference PS. The aPDI activity of GaPpIX against *S. aureus* is rapid, with

antimicrobial action (>99.9%) at 59 nM after 10 sec of irradiation, a 2000-fold increase in potency relative to GaPpIX dark toxicity (data not shown here).[66] Total eradication (>6 $\log_{10}$ reduction) was observed at 235 nM (Figure 1.12a). By comparison, the aPDI activity of TMPyP and PpIX were 8 and 32-fold less potent than that of GaPpIX. GaPpIX also showed similar potency against several clinical isolates of MRSA using the same condition (Figure 1.12b).[66] No significant cytotoxicity was found against kidney cells (HEK 293) or skin cells (HaCaT), up to 20 μM of GaPpIX.

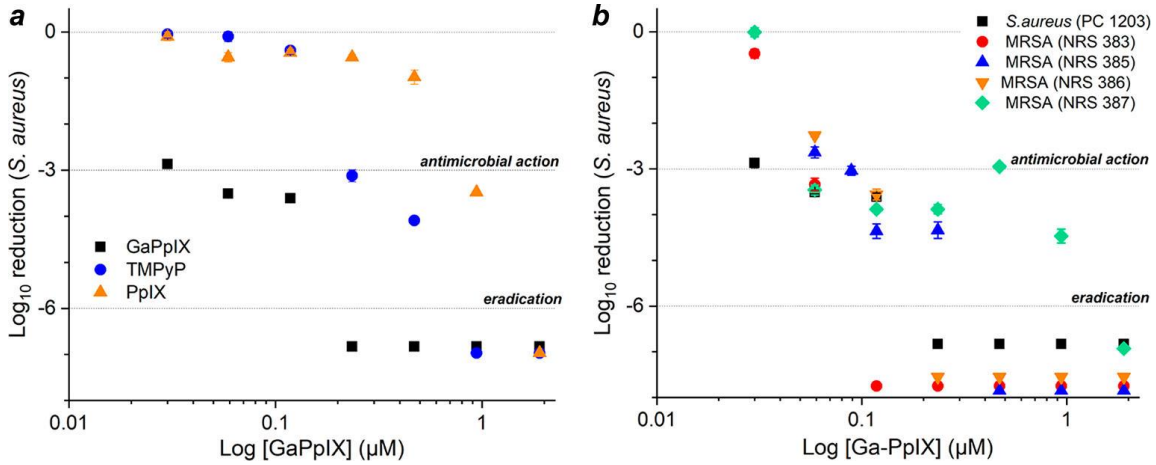

Figure 1.12. (a) Antimicrobial photodynamic inactivation of a laboratory strain of *S. aureus* (PC1203) using GaPpIX, TMPyP, or PpIX, with 10-s exposure to 405-nm light from a LED array (1.4 J/cm^2). (b) aPDI activity of GaPpIX against several clinical isolates of MRSA (NRS 383, NRS 385, NRS 386 and NRS 387). Adapted from Morales *et al*.[66]

1.1.6 AgNP as a PDI-Enhancing Agent

The antimicrobial efficacy of silver has been well known for centuries.[67] Silver exhibits low toxicity to mammalian cells, but is highly toxic to most bacteria. Although silver-resistant bacteria have been more frequently reported, silver is still considered as one of the alternative treatments for the world wide emergence of antibiotic– and other biocide-resistant bacteria.[68-72] In primeval times, silver was used for making utensils, and dental alloy fillings, and was used to treat open

wounds and burns due to its antiseptic activity.[73-75] Silver ions can induce bacterial death by disrupting or inhibiting protein function, and by compromising the permeability of the bacterial cell wall (Figure 1.13). Some studies found that silver ions are able to inhibit bacterial replication by binding and denaturing the DNA.[76-77] Another mechanism of the antibacterial effect of silver ions on *E. coli* and *S. aureus* may be related to its affinity for thiol group on proteins, which interferes with DNA processing.[78]

Silver nanoparticles (AgNPs) have been found to be more potent bactericides than silver ions and other silver salts, possibly due to their extremely large surface area, which provides better contact with microorganisms.[79-80] Moreover, smaller AgNPs (1–10 nm) are known to be electroactive, which has been reported to enhance their reactivity.[80-82] AgNPs have a very broad range of antimicrobial activity and can kill both Gram-negative and Gram-positive bacteria, including MDR strains such as MRSA and ampicillin-resistant *E.coli* O157:H7.[83-84] It was proposed that AgNPs act against Gram-negative bacteria in two stages: first, AgNPs attach to the cell membrane surface and drastically disturb its permeability and resporation; second, AgNPs release silver ions to help further induce cell death.[82]

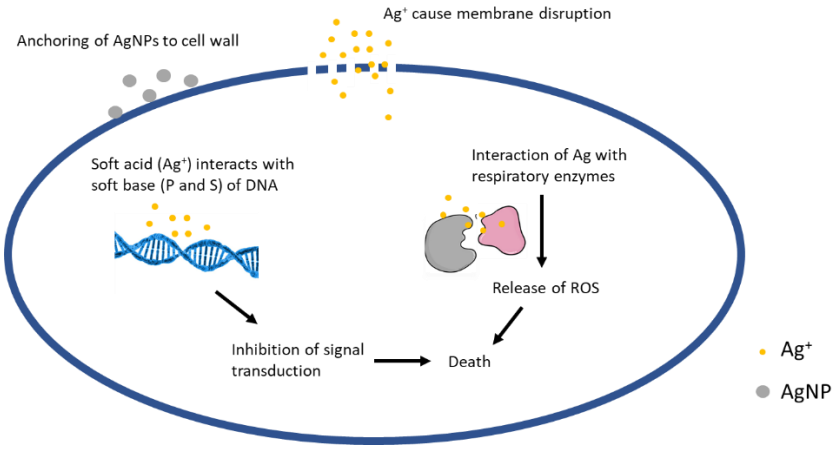

Figure 1.13. Schematic overview of antimicrobial interactions of AgNPs in bacteria.

AgNPs also exhibit a strong surface plasmon resonance (SPR), which is a desirable property for aPDI because the production of $^1O_2$ can be significantly increased due to the strong resonant coupling between the surface plasmon and PS, meaning that light-absorbing PS near metal nanoparticles have a stronger absorption cross section due to the localized surface plasmon.[85] The strength of plasmon–PS resonance coupling is highly sensitive to the spectral overlap between the molecular absorption and the surface plasmon bands of metal nanostructures.[85] One study showed that the resonant coupling between the absorption band of J-aggregate molecules (a self-organizable supramolecular dye) and the plasmonic band of AgNPs greatly enhanced the exciton lifetime, while the coupling with AuNPs yielded a reduced exciton lifetime.[86] Other studies on the aPDI activity of hybrid PS–AgNPs found a strong plasmon- resonant coupling between AgNPs and PS molecules, which increased singlet oxygen production by up to three orders of magnitude and resulted in highly efficient PDI against both Gram-positive and Gram-negative bacteria.[85, 87]

In order to enhance the aPDI activity of GaPpIX we chose to hybridize it with AgNPs, whose absorbance overlaps with that of GaPpIX absorbance centered at 405 nm. We expect the excitation of GaPpIX to be further amplified by AgNPs, further enhancing the production of $^1O_2$ and ROS. Our goal is to coat AgNPs with modified hemoglobin (Hb) in which hemin is substituted by GaPpIX, and to apply those toward aPDI treatment against bacteria that can cause skin infections. The reason for using Hb is that GaPpIX has poor solubility in water at physiological pH, although it is highly soluble in organic solvents such as DMSO.[88-89] As the native carrier of heme, Hb not only increases the solubility of GaPpIX and eliminates the use of organic solvent, but also targets the bacteria more specifically through its recognition by CSHRs.[90]

In this chapter, we discuss the development of GaHb-coated AgNPs, and investigate their aPDI effect against vectors of skin infections such as MRSA and *Mycobacteria abcessus*, and work toward the long-term goal of developing a topical agent for aPDI treatment of skin infection.

1.2 Results and Discussion

1.2.1 Characterization of GaHb

Hemoglobin (Hb) is a protein in red blood cells that carries oxygen. In humans, the most common type of hemoglobin is called Hb A, a non-covalent tetramer comprised of two α and two β globular subunits. Each subunit has a binding pocket that associated with a prosthetic heme group. In a high pH and low CO_2 environment, Hb exists in a relaxed form that is conducive for binding oxygen.[91] Oxidation of the iron atom from Fe^{2+} to Fe^{3+} reduces its atomic diameter, allowing it to pulled into the plane of the porphyrin ring.[92] This slight conformational shift also assists the binding of oxygen by the remaining three heme subunits within Hb.

During an infection, bacteria attempt to acquire heme iron for survival, as over 70% of the iron in the human body is in the form heme. As discussed previously, there is very little free heme in the body, with Hb being the most accessible form available to extracellular pathogens.[93] In order to scavenge hemin and Hb, bacteria often secrete hemolysin to lyse the red blood cell and release Hb. In some cases, such as *Mycobacteria*, they obtain Hb or hemin from vacuoles within macrophages. As described in section 1.1.4, free Hb can then be acquired directly by CSHR-expressing bacteria, then degraded for extraction of hemin from that. Other type of bacteria (mostly Gram-negative) rely on the extracellular hemophores to bind free Hb and return them to cells.

In our system, GaHb uses Hb as a carrier for GaPpIX, and also facilitates its acquisition by CSHR-expressing bacteria for targeted aPDI. We used a commercially available bovine Hb, which

has over 90% sequence homology with human Hb but costs significantly less.[94] Hemin was first removed by treating Hb with mild acid to produce apohemoglobin (apoHb, Figure 1.14), which was extracted using a literature procedure.[95] Removal of the hemin is reflected by the disappearance of the Soret band (λ_{max} ~ 400 nm) from the absorbance spectrum (Figure 1.15). At 0 ºC, 4 equiv. of GaPpIX was added to 1 equiv. of apoHb to produce GaHb. The Soret band (λ_{max} ~ 415 nm) reappeared with a slight redshift relative to free GaPpIX and Hb, consistent with previously reported results.[96]

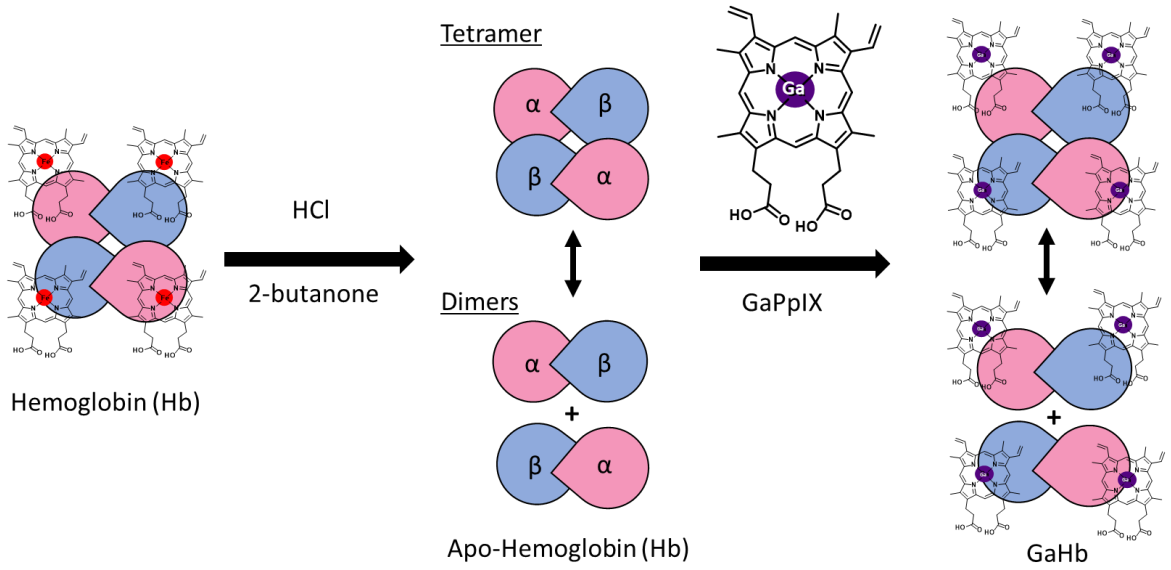

Figure 1.14. GaHb is prepared by removing hemin from hemoglobin then inserting GaPpIX.

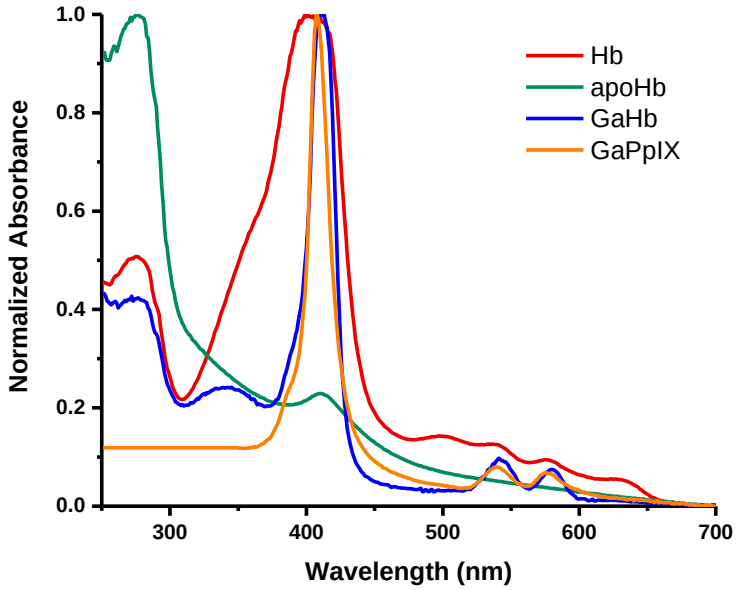

Figure 1.15. Absorbance spectra of Hb (red), apoHb (green), GaHb (blue), and GaPpIX (orange).

Hemoglobin in physiological conditions exists in a dimer–tetramer equilibrium (K_d ~3 μM),[97] and to a less significant extent a monomer–dimer equilibrium (K_d << 1 pM).[98] We believe apoHb and GaHb to exist mostly as αβ-dimer subunits in our experiments, according to previous literature.[99] The dissociation constant for hemin and the Hb αβ-subunit have been measured by Hargrove, with estimates in the range of 1.7–42 pM.[100] To determine whether Hb had a similar binding affinity for GaPpIX, we used fluorescence polarization to measure the dissociation constant between GaPpIX and apoHb dimer. Briefly, fluorescence polarization is a powerful tool to study changes in molecular orientation and mobility, with direct application toward the measurement of binding constants. In homogeneous solution, GaPpIX molecules are assumed to tumble isotropically; upon exposure to polarized light at 405 nm, those molecules whose absorption transition moments are aligned with the plane of excitation are excited preferentially with a characteristic lifetime associated with size-dependent tumbling. In the presence of a receptor

protein such as the apoHb αβ-subunit (~32 kDa), the tumbling rate of GaPpIX (0.67 kDa) decreases significantly upon binding, causing an increase in polarized signal. The changes are proportional to the fractional concentration of protein–ligand complex formed at the time of excitation, and can be modeled according to a Langmuir–Freundlich isotherm to obtain an effective association constant (K_a), which is inverted to yield the dissociation constant (K_d).[101]

We incubated the 100 nM of GaPpIX with different amounts of apoHb αβ-subunit for over 4 hours in phosphate buffered saline (PBS) at 4 ºC before measurement. The absorption density (q) was measured as a function of αβ-subunit concentration at 37 ºC (Figure 1.16). Our results gave a dissociation constant (K_d) of 24 nM; if both α and β units are assumed to bind GaPpIX equally, the actual K_d value is close 48 nM. This number is quite large compared with the K_d value of hemin-Hb dimer reported in the literature (1.7–42 pM), but there are several reasonable explanations for the discrepancy.[100] One could be the difference in assays: Hargrove and coworkers used apomyoglobin as the hemin receptor, and the rate constant was indirectly derived from the disappearance of apomyoglobin and the formation of holomyoglobin. In comparison, our K_d value was generated by measuring the changes of the fluorescence intensity (ΔI) of GaPpIX between bound and unbound states. Another reason could be that FePpIX bound Hb more tightly than GaPpIX.

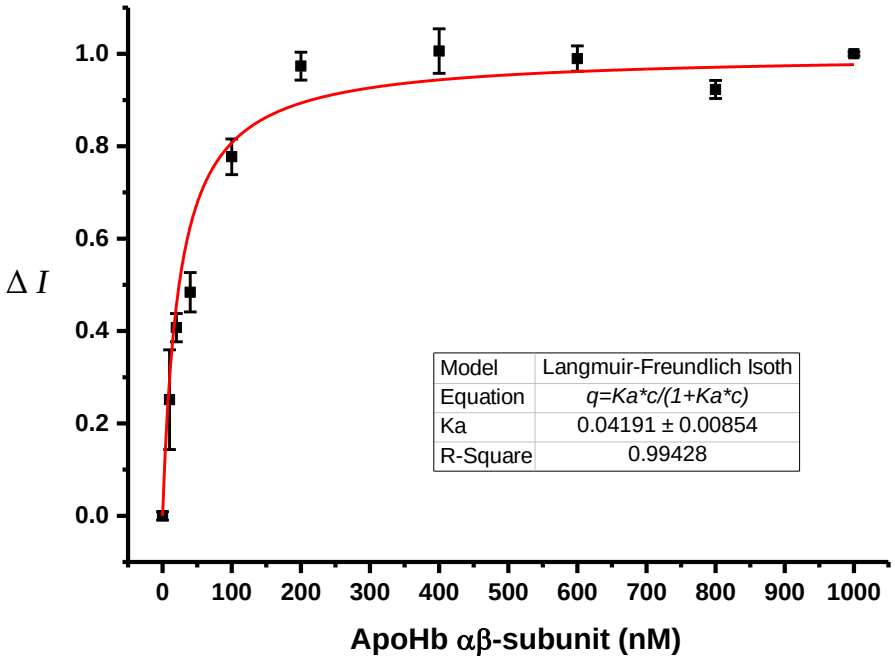

Figure 1.16. Normalized changes in fluorescence intensity (ΔI) of 100 nM GaPpIX versus concentration of apoHb αβ-subunits, fitted to a Langmuir–Freundlich isotherm. q is normalized changes of the fluorescence intensity; K_a is association constant in nM^{-1}; c is αβ-subunit concentration. Measurements were run in triplicate.

1.2.2 Coating and Characterization of AgNPs with GaHb

Commercially available, citrate-stabilized 10-nm AgNPs were mixed with GaHb in PBS (1 mg/mL) and incubated overnight at 4 °C. The next day, free GaHb molecules were removed from the mixture by centrifugation, followed by redispersion in 15 mM borate buffer (pH 8.5). GaHb-coated AgNPs showed a slight redshift in plasmon resonance compared with AgNPs before coating (Figure 1.17). We also observed a shoulder in the spectra of GaHb-AgNP around 450–500 nm, indicating a certain degree of aggregation (Figure 1.17).

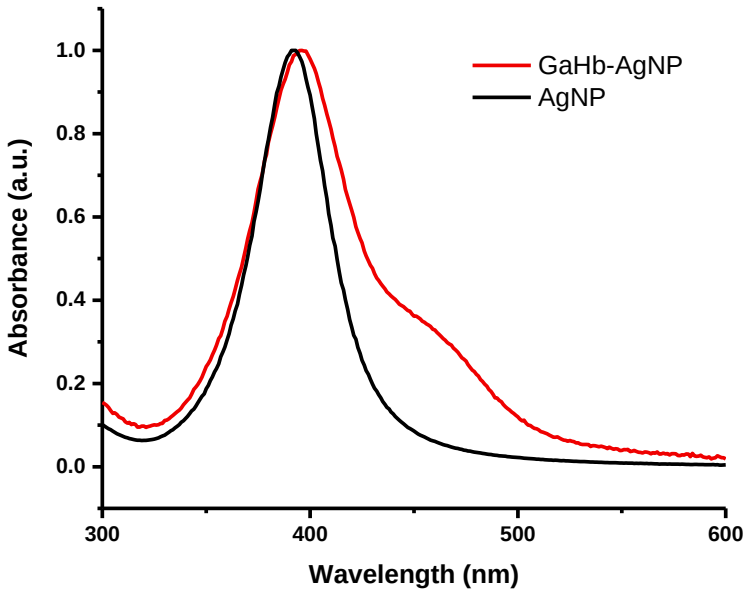

Figure 1.17. UV-visible spectra of 10-nm AgNP and GaHb-AgNP assembly.

We evaluated the hydrodynamic size and zeta potential of GaHb-AgNP using dynamic light scattering (DLS) (Figure 1.18 and Table 1.1). The surface zeta potential of AgNPs coated with GaHb shifted by +15 mV relative to citrate-stabilized AgNPs, whereas the mean hydrodynamic size increased from 14 nm to 17 nm. It is known that zeta potential of bovine Hb by itself at pH 8.5 is slightly anionic (-8 mV). When surface citrate was displaced by GaHb, the zeta potential of AgNPs became less negative, and behaved more like GaHb.

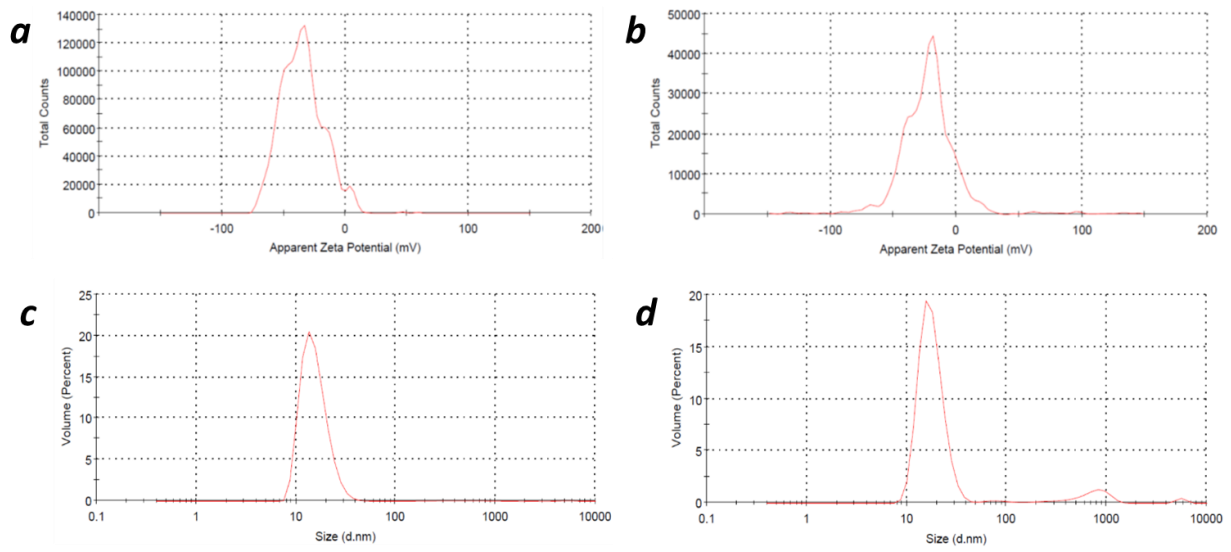

Figure 1.18. Zeta potentials for (a) AgNP; (b) GaHb-AgNP; DLS size distributions by volume for (c) AgNP; (d) GaHb-AgNP.

Table 1.1 Zeta potential and mean hydrodynamic sizes of AgNPs and GaHb-coated AgNPs.

	Zeta Potential (mV)	Mean hydrodynamic size (nm)
AgNP	–34.4	14
GaHb-AgNP	–19.0	17

We also examined GaHb-coated AgNPs by transmission electron microscopy (TEM), using negative staining with 1% phosphotungstic acid in order to resolve the protein coating. However, the images were not able to show a definite protein layer (Figure 1.19). This could due to the small size of AgNPs that the resolution of the instrument combined with negative staining were not enough to present the protein coating on each NP.

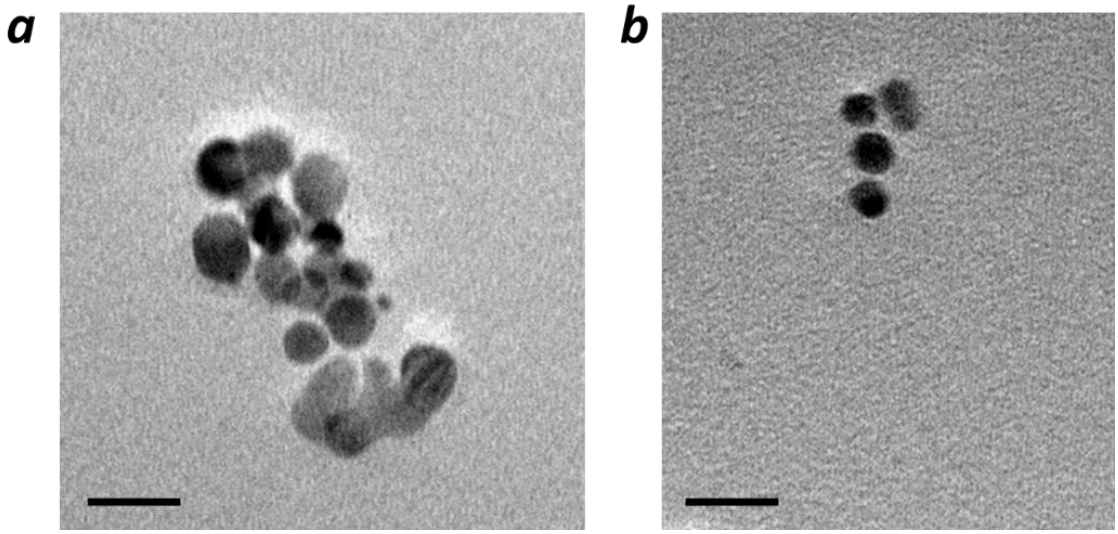

Figure 1.19. TEM image of (a) GaHb-AgNP and (b) AgNP. With 1% phosphotungstic acid staining, no significant negative contrast was shown in (a).

1.2.3 GaHb-AgNPs in aPDI against *S. aureus*

Previous studies in our group by Dr. Ana Morales showed that GaHb-AgNP was a fast-acting aPDI agent against a *S. aureus* laboratory strain (PC1203), as well as several MRSA clinical isolates, when using a monochromatic LED source (λ_{max} 405 nm, 1.4 J/cm^2). The synergistic effect between GaHb and AgNP was also confirmed: bacteria suspensions in 96-well plates were treated with aliquots of GaHb-AgNP, GaHb, AgNP and GaPpIX, followed immediately by a 10-second exposure to 405-nm LED light (140 mW/cm^2). The results showed that the aPDI activity of GaHb-AgNP was over 3 orders of magnitude more potent than the other treatments at equivalent AgNP or GaPpIX concentrations (Figure 1.20).

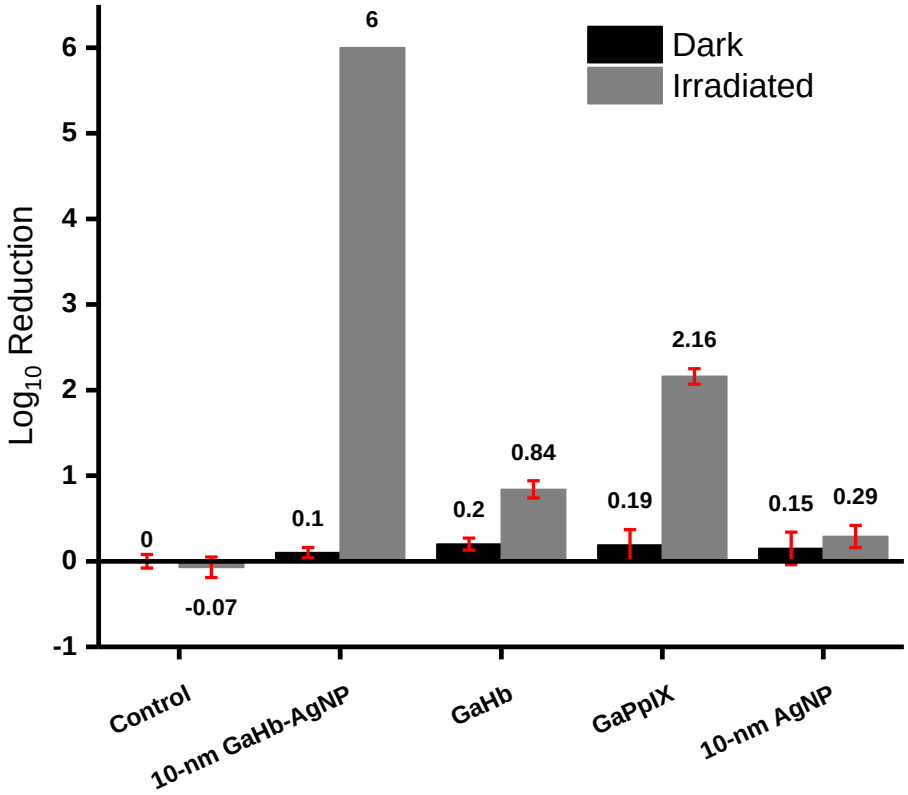

Figure 1.20. Log reduction in *S. aureus* cell viability when treated with PBS pH 7.4 (control), 10-nm GaHb-AgNP (5.7 µg/mL), GaHb (0.66 µg/mL), GaPpIX (27 ng/mL), and 10-nm AgNP (5 µg/mL), after a 10-s exposure to a 405-nm LED source (140 mW/cm2). All experiments were run in triplicate. Adapted from Morales *et al.*[102]

To determine whether GaHb-AgNPs were being internalized by *S. aureus*, we performed TEM analysis on sectioned bacteria to evaluate the location of GaHb-AgNPs using different incubation time (5 minutes, 30 minutes and 1 hour). In all case, AgNPs were consistently found to reside on the outside of the bacteria membrane (Figure 1.21).

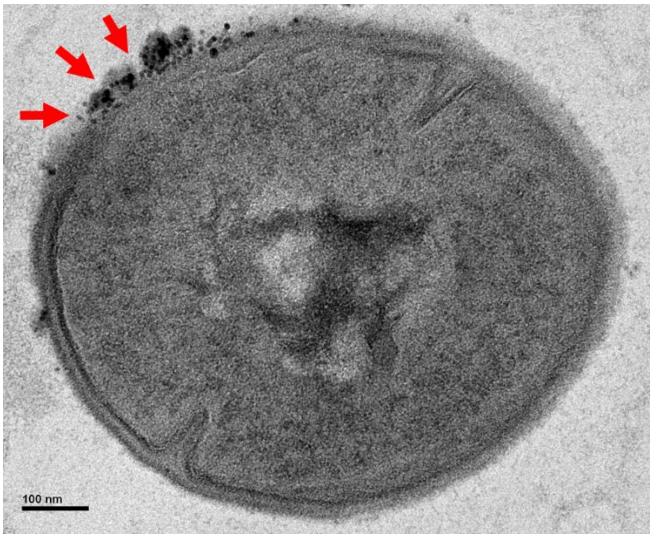

Figure 1.21. TEM image of *S. aureus* incubated for 1 hour with GaHb-AgNPs. Arrows indicate GaHb-AgNPs on the outer bacterial wall.

1.2.4 GaHb-AgNPs in aPDI against Intracellular MRSA

The relapse of *S. aureus* infection after a first round of antibiotic treatment has become a major health issue. *S. aureus* infections were originally considered to be strictly extracellular in nature, but more recent studies have found that multiple cell types can host *S. aureus* cell internally and provide them with an antibiotic-free environment to grow and multiply until lysis occurs.[103] An enrichment of macrophages is expected at the infection site. The main role of macrophages and neutrophils is to ingest and eliminate invading pathogens. While neutrophils have a very short life span and are unlikely to be useful carriers of intracellular pathogens, macrophages are much longer lived and can travel through the circulatory system from the original infection site, promoting the spread of secondary infections. In this study, we choose to investigate the aPDI effect of GaHb-AgNP on intracellular *S. aureus in macrophages.*

MRSA 300, a MDR strain that is closely associated with community outbreaks in the United States, was chosen to infect a murine macrophage cell line (J774). Cells were cultured in iron-deficient conditions and treated with gentamicin after infection to eliminate extracellular bacteria.

Infected macrophages were than exposed to GaHb-AgNPs at three different concentrations, followed either by immediate exposure to 405-nm LED light for 10 seconds (1.4 J/cm^2) or 24 hours incubation before the same light treatment. The results showed over 80% of intracellular MRSA were killed at 22.6 µg/mL GaHb-AgNP and over 90% kill at 45.3 µg/mL GaHb-AgNP, when irradiated immediately after treatment (Figure 1.22). A 24-hour delay in light exposure yielded a lower percentage kill, although the differences were within 10% when 22.6 µg/mL GaHb-AgNP was used. This could be a result of macrophage's efflux pump activity that cleared some GaHb-AgNPs out of the cell before aPDI could be applied.[16]

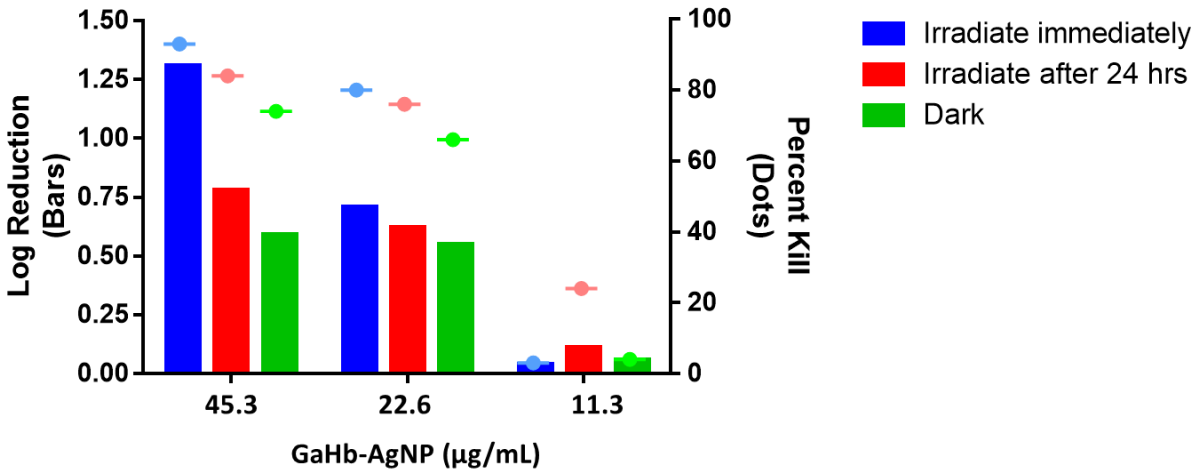

Figure 1.22. Percent and log reduction in intracellular MRSA cell viability when treated with 45.3 µg/mL, 22.6 µg/mL and 11.3 µg/mLof GaHb-AgNPs, after an immediate or 24-hour delayed exposure to 405-nm LED source (10 seconds, 140 mW/cm^2). Each condition was run in triplicate.

TEM analysis was used to characterize the fate of intracellular bacteria and their colocalization with GaHb-AgNPs (Figure 1.23). Due to the large volume of the bacteria solution required for TEM processing, it was not practical to apply aPDI conditions. Nevertheless, TEM image analysis confirmed the colocalization of intracellular MRSA and GaHb-AgNPs: even without 405-nm light

treatment, we observed a high density of AgNPs around the bacteria, some of which had damaged cell walls.

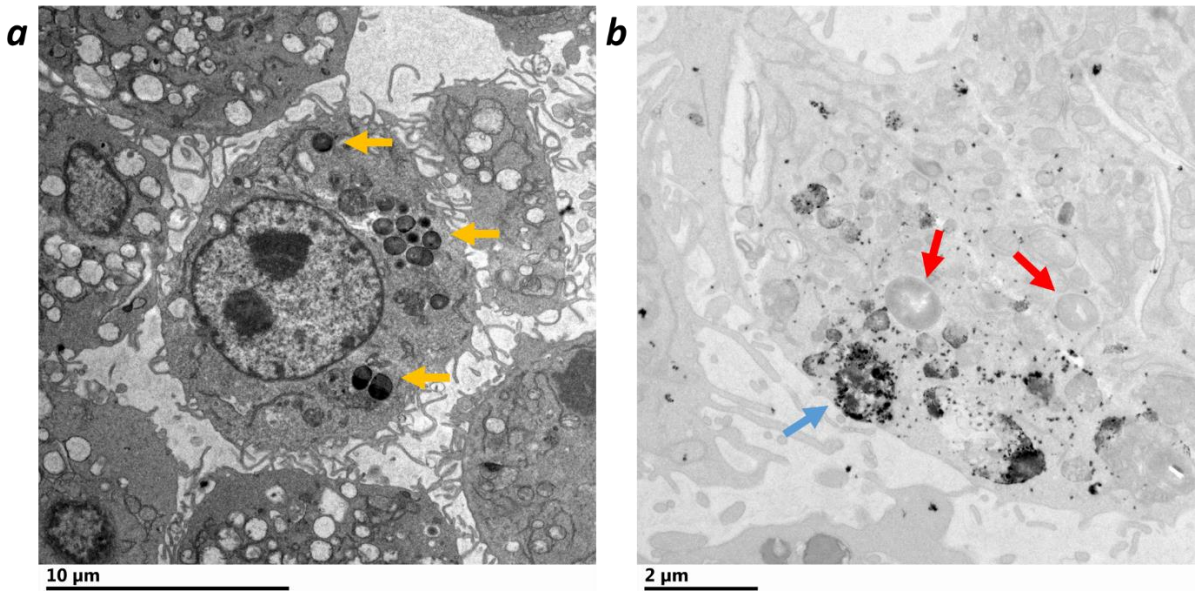

Figure 1.23. Co-localization of GaHb-AgNPs with intracellular MRSA cells observed by TEM. (a) J774 macrophages infected with MRSA (yellow arrows) without GaHb-AgNPs; (b) morphologically intact (red arrows) and damaged (blue arrow) intracellular MRSA after treated with 45.28 µg/mL GaHb-AgNPs for 16 hours.

1.2.5 GaHb-AgNPs in aPDI against Biofilms

Bacteria biofilm form are much more resistant to various antimicrobial treatments than planktonic bacteria and can also survive harsh conditions and withstand the host's immune system. *There are three major stages involved in the biofilm development: initial attachment, biofilm maturation, and dispersal.*[18] *Biofilm formation frequently occurs in the h*uman anterior nostrils, a common ecological niche for *S. aureus colonization.*. I*n the human population, about 20-25% have become persistently colonized by S. aureus. A potential antibiofilm agent that can either facilitate the dispersion of preformed biofilms or inhibit the formation of new biofilms is needed.*

In this study we examined the combined effect of GaHb-AgNP-mediated aPDI and vancomycin against pre-formed and mature *S. aureus* biofilms. Since one of the potential mechanisms for biofilm to be antibiotic-resistant is forming a diffusion barrier, we hypothesized that aPDI could synergize with antibiotic activity by weakening the barrier and therefore increase the permeability of antibiotics. MRSA 300 was cultured under conditions that produced a strongly adherent biofilm. GaHb-AgNP, vancomycin or both were added to the biofilm at concentrations ranging from 0.3 μg/mL to 64 μg/mL, followed by 10 seconds of 405-nm light exposure. The biofilm culture was incubated at 37 °C for 24 hours, then stained using 0.1% crystal violet. Unfortunately, the results showed hardly any reduction in biofilm mass after aPDI treatment with or without vancomycin (Figure 1.24).

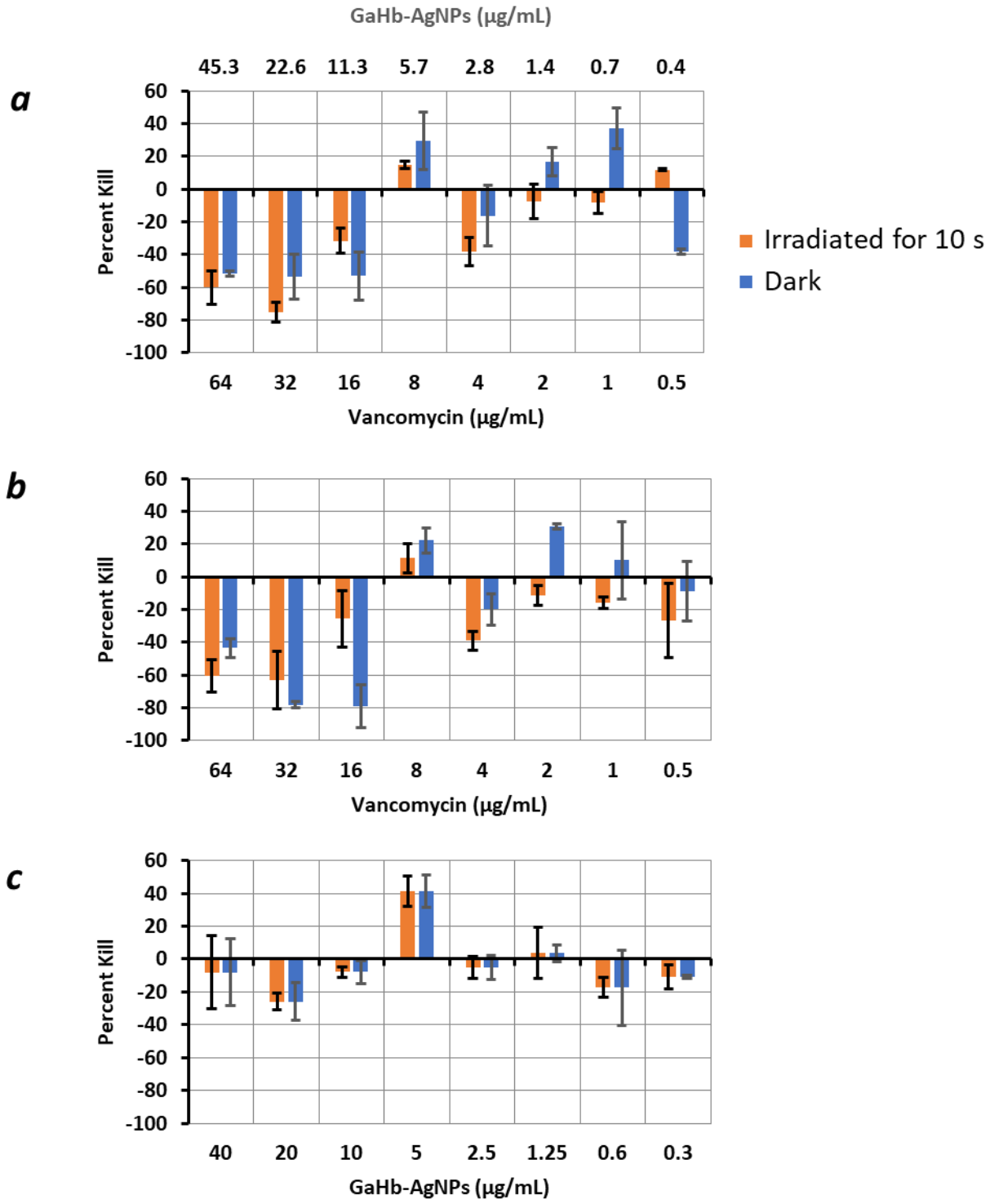

Figure 1.24. aPDI against MRSA biofilms treated with various concentrations of (a) GaHb-AgNPs and vancomycin; (b) vancomycin only; (c) GaHb-AgNPs only, after a 10-second exposure to 405-nm light (140 mW/cm2). Each treatment was conducted in triplicate.

We also investigated the effect of aPDI on the inhibition of *S. aureus* biofilm formation. Suspension of MRSA 300 bacteria were treated with GaHb, GaPpIX, GaHb-AgNP and AgNP at concentrations ranging from 0.6 to 40 μg/mL in units of AgNP or 3.5 to 233.5 ng/mL in units of GaPpIX, followed by 10 seconds of 405-nm light exposure. Treated cells were incubated at 37 °C for 24 hours, and biofilm mass was quantified using 0.1% crystal violet. Unfortunately, the percent inhibitions were again not significant for any of the treatments (Figure 1.25). Even when combined with vancomycin, no synergistic aPDI effect was observed (Figure 1.26). The minimum inhibitory concentration (MIC) of vancomycin to MRSA is known to be between 0.125 to 1 μg/mL, depending on the strain.[104] Thus, greater than 90% inhibition was observed when the concentration of vancomycin was over 0.25 μg/mL but barely any inhibition when using GaHb-AgNP only. Interestingly, we also observed that GaHb-AgNPs, when used at concentrations higher than 2.5 μg/mL in AgNP unit, actually promoted biofilm growth.

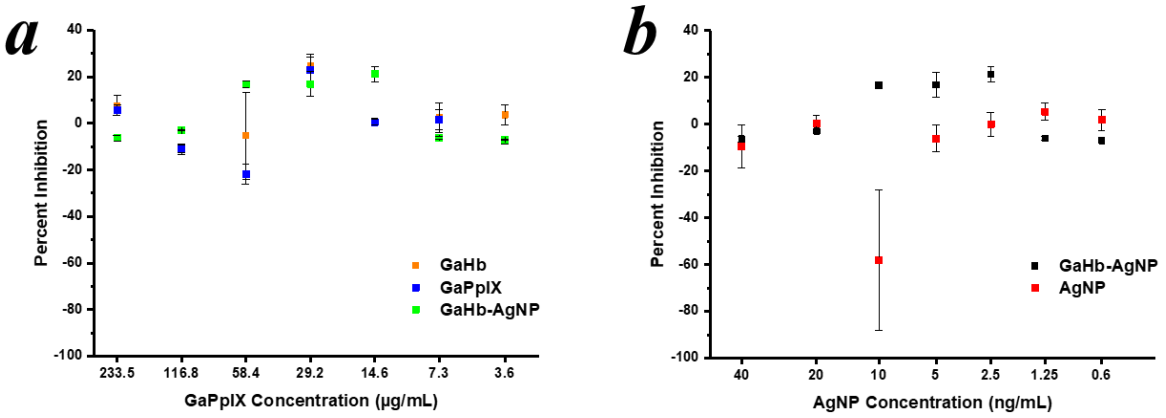

Figure 1.25. aPDI for MRSA biofilm inhibition when treated with various concentrations of (a) GaHb, GaPpIX, and GaHb-AgNP, and (b) GaHb-AgNP and AgNP after a 10-second exposure to a 405-nm light (140 mW/cm^2). Each treatment was conducted in triplicate.

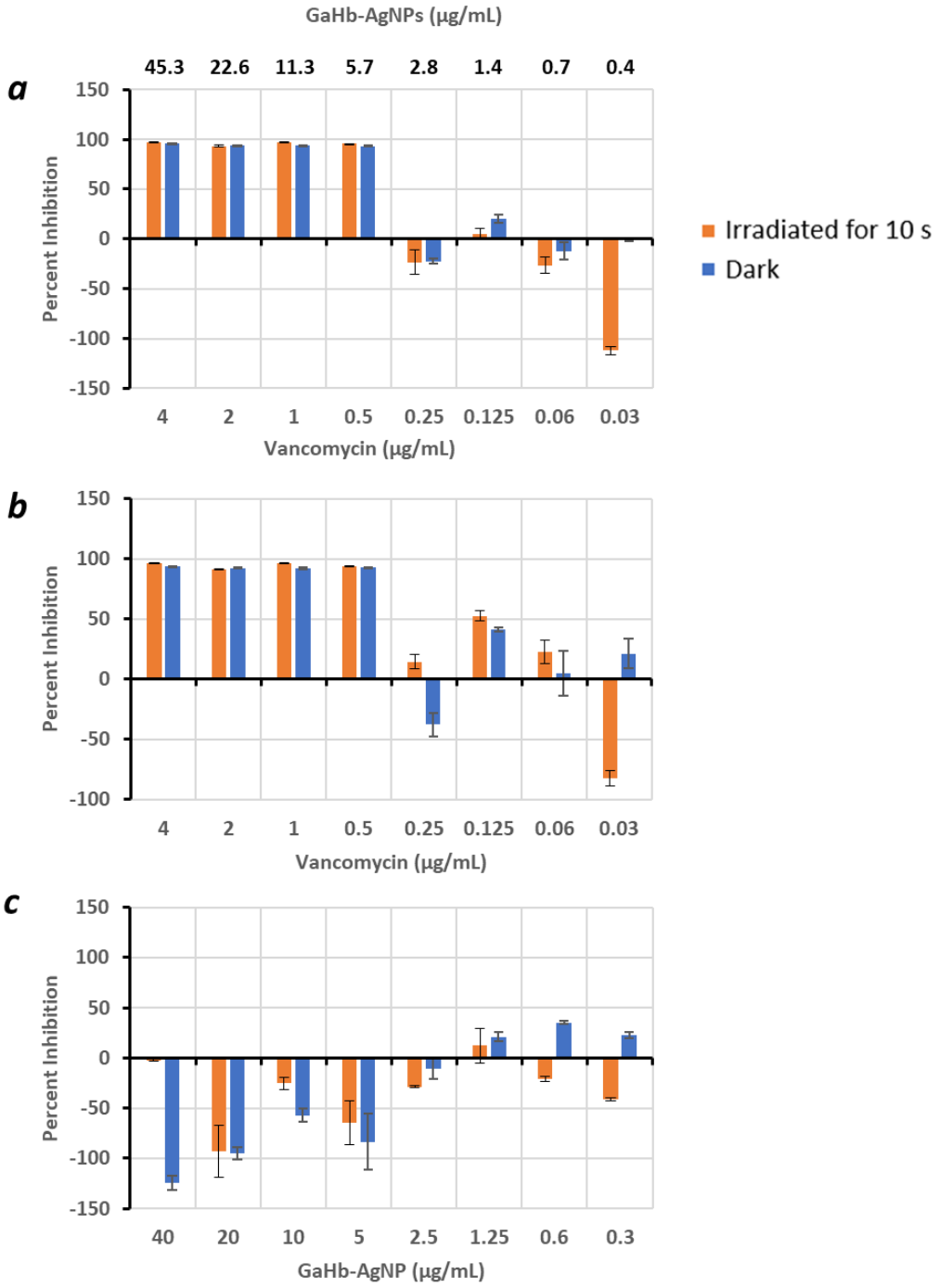

Figure 1.26. aPDI for MRSA biofilm inhibition when treated with various concentrations of (a) GaHb-AgNPs and vancomycin; (b) vancomycin only; (c) GaHb-AgNPs only, after a 10-second exposure to 405-nm light (140 mW/cm^2). Each treatment was conducted in triplicate.

1.2.6 GaHb-AgNPs in aPDI against *M. abscessus*

Currently the available treatment strategies for *M. abscessus* infections consist of prolonged antimicrobial drug therapy.[105] Some of these come with severe side effects, forcing a pre-mature termination of therapy. For example, amikacin is a powerful antibiotic that is administered intravenously and is associated with multiple side effects such as hearing loss, dizziness and numbness. Over half of the patients that receive amikacin injections had to discontinue treatment or reduce the dosage.[105] Alternative treatment regimens are needed to maximize efficacy while minimizing side effects.

In this study we first investigated the effect of aPDI effect on the inhibition against *four M. abscessus* strains (Figure 1.27). Bacteria suspensions were treated with GaHb, GaPpIX, GaHb-AgNP or AgNP at either 20 and 40 μg/mL in units of AgNP or 116.8 and 233.5 ng/mL in units of GaPpIX, followed by a 10-second exposure to 405-nm light. Treated cells were then plated and incubated at 37 °C for four days before counting. One strain (ATCC 49093) showed minimal reduction, but the remaining three (ATCC 44263, ATCC 44273 and ATCC 44266) responded to aPDI treatment. However, despite this positive result, aPDI with GaHb-AgNP did not provide a significant increase in potency relative to GaHb or GaPpIX.

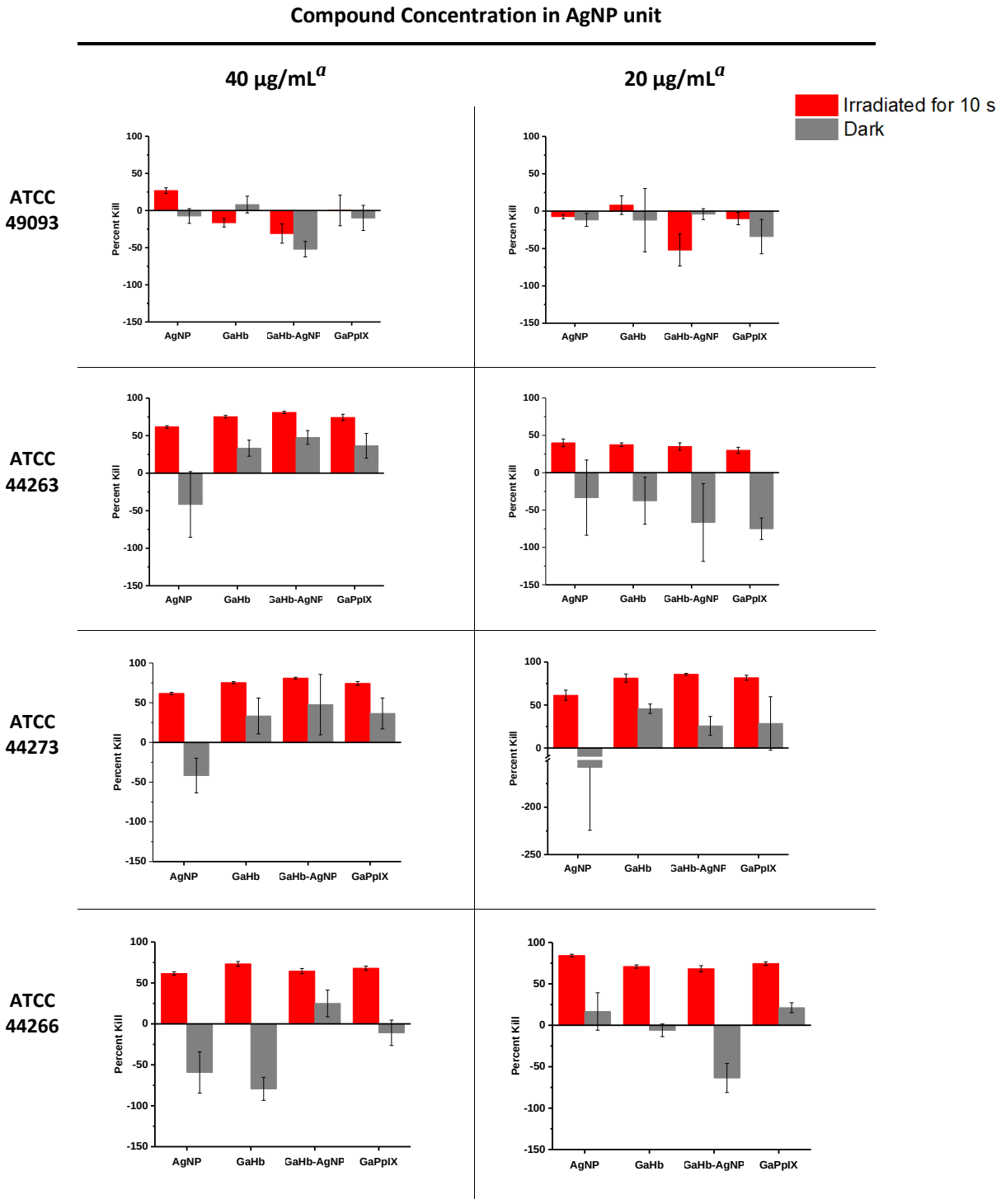

Figure 1.27. aPDI against *M. abscessus* strains when treated with various concentrations of GaHb, GaPpIX, GaHb-AgNP or AgNP, after a 10-second exposure to 405-nm light (140 mW/cm^2). Each treatment was conducted in triplicate. [a] GaHb and GaHb-AgNP at same molar equivalent as GaPpIX.

1.2.7 GaHb-AgNPs and Antiseptic in aPDI against *M. abscessus*

Povidone-iodine (PVP-I) and chlorhexidine gluconate (CHG) are widely used antiseptics against conventional skin infections caused by *S. aureus*, *Enterobacteriaceae* and viruses. Previous studies here indicated that clinically prevalent *M. abscessus* strains are highly resistant to most commercial formulations of CHG, and are only partially susceptible to PVP-I.[106] Since the skin is a primary source of pathogens following a surgical procedure, insufficient mycobactericidal activities of the currently used antiseptics increase the risk of post-surgical infections.[107-108]

In this study we examined the combination of GaHb-AgNP with antiseptics as a bactericidal treatment against *M. abscessus* (ATCC 44263). GaHb-AgNP (22.6 μg/mL), antiseptic (0.1% PVP-I or 0.04% CHG), or both were added to bacterial suspensions of 10^7 CFU/mL and exposed to 10 seconds of 405-nm light using the LED source. Treated cells were plated right away and incubated at 37 °C for four days before counting. The results showed no significant synergistic effect between the antiseptics and aPDI with GaHb-AgNP (Figure 1.28). There is a significant gap of knowledge regarding the heme acquisition pathway of *M. abscessus* and of mycobacteria in general. It is known that *M. tuberculosis* acquire nonheme iron via iron-chelating molecules named siderophores, which chelate ferric ion with extremely high affinity, allowing its solubilization and extraction from most mineral or organic complexes. Only until recently, studies suggested that mycobacteria can acqurie metalloporphyrins such as heme by secreting hemophores such as protein Rv0203.[109] The mechanism of mycobacterial heme uptake needs to be further explored. Nevertheless, in both mechanisms it is known that, heme or nonheme iron are both directed to specific cell surface receptors for further iron extraction.[109-110] Therefore the recognition and uptake of GaHb-AgNP may not be as efficient as CSHR-expressing bacteria, such as *S. aureus*, and that may contribute to the lower potency toward *M. abscessus*.

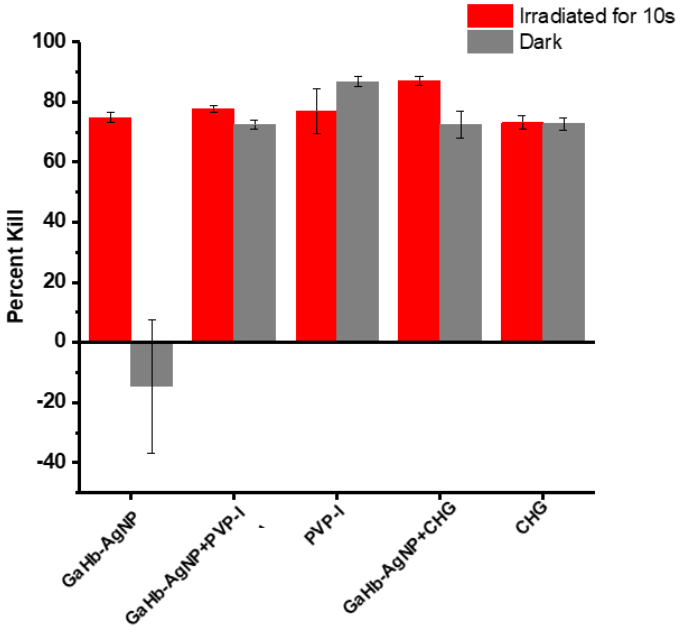

Figure 1.28. aPDI against *M. abscessus* (ATCC 44263) when treated with 22.6 μg/mL GaHb-AgNPs only, 22.6 μg/mL GaHb-AgNPs and 0.1% PVP-I, 0.1% PVP-I only, 22.6 μg/mL GaHb-AgNPs and 0.04% CHG, and 0.04% CHG only, after a 10-second exposure to 405-nm light (140 mW/cm^2). Each treatment was conducted in triplicate.

1.2.8 Cytotoxicity of GaHb-AgNPs

GaHb-AgNPs have proven to be exceptional photosensitizers with nanomolar aPDI effect against clinically relevant MRSA strains, and also have great potential in targeting intracellular MRSA, following a 10-second irradiation with a 405-nm LED source. As a step toward preclinical evaluation, we also investigated the cytotoxicity of GaHb-AgNPs against keratinocytes using HaCaT cells and macrophages using J774 cells.

The dark toxicity against HaCaT cells was evaluated using GaHb-AgNP concentrations ranging from 5.7 to 45.7 μg/mL. HaCaT cells were incubated with GaHb-AgNPs at 37 °C for 22 hours before measuring cell viability using the MTT assay. No significant cytotoxicity was seen

at the highest concentration (Figure 1.29). The increase in cell population at high concentrations may due to the production of non-lethal levels of ROS, resulting in a hormetic response that can enhance the cellular function, homeostasis and growth factor production.[111-113]

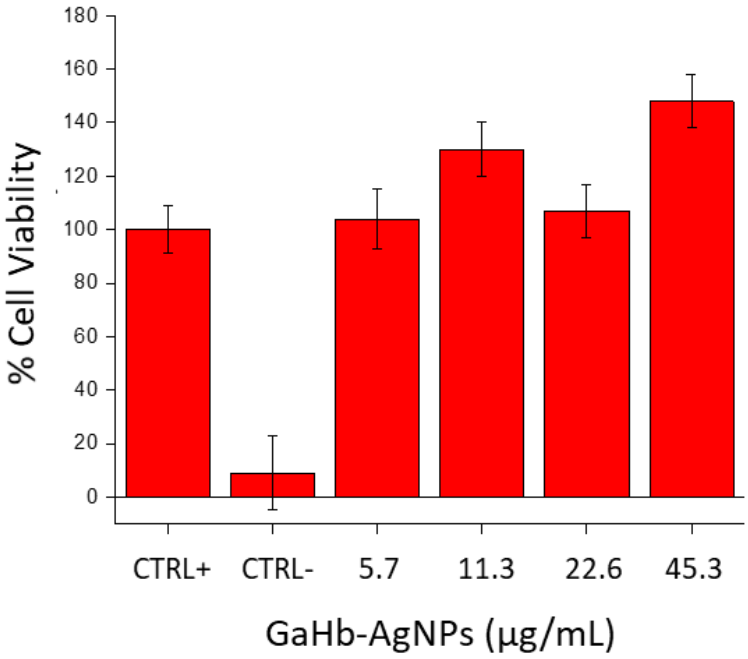

Figure 1.29. Cell viability assay for dark toxicity against HaCaT cells. (*N* = 3). Positive control (CTRL+) represents cells without GaHb-AgNPs; negative control (CTRL–) represents cells treated with 0.005% Triton X-100.

The phototoxicity of GaHb-AgNPs against HaCaT cells was evaluated using a 10-second exposure to 405-nm light. HaCaT cells were pre-incubated with 22.6 or 45.3 µg/mL GaHb-AgNPs for up to 24 hours prior to irradiation. Only at 45.3 µg/mL, the highest concentration, we observed phototoxicity (Figure 1.30).

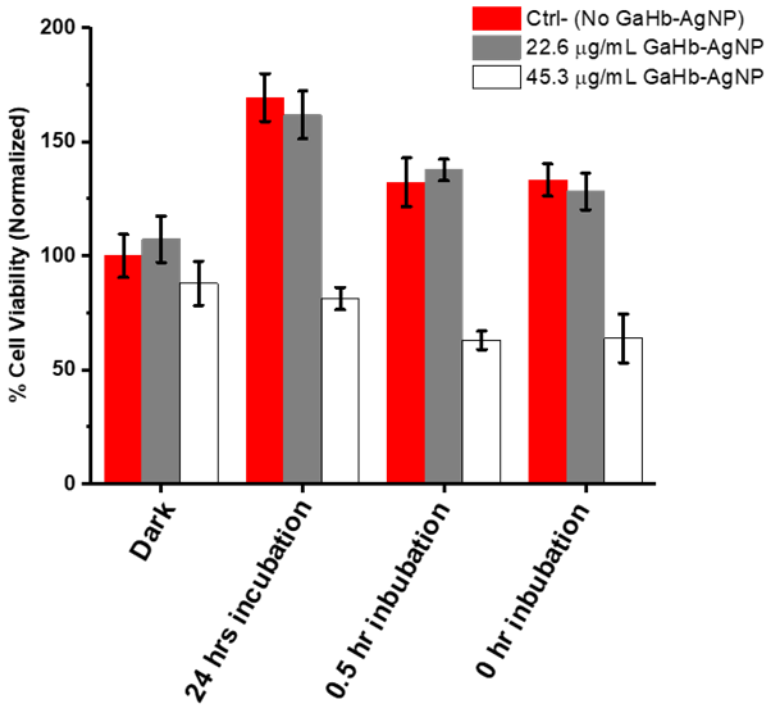

Figure 1.30. Cell viability assay for phototoxicity against HaCaT cells. (N = 3). Cells were incubated for various times prior to a 10-second exposure to 405-nm light (140 mW/cm^2).

The cytotoxicity of GaHb-AgNPs against J774 cells was also evaluated using a 10-second exposure to 405-nm light. J774 cells were pre-incubated with GaHb-AgNPs ranging from 5.7 to 45.3 μg/mL for up to 24 hours, prior to 405-nm light irradiation. Cell viability was measured using the MTT assay, with J774 cells maintaining over 80% cell viability in the absence of light, or if irradiated 24 hours after incubation (Figure 1.31). Cytotoxicity was also not observed when light exposure was conducted immediately after introducing GaHb-AgNPs, except at the highest concentration.

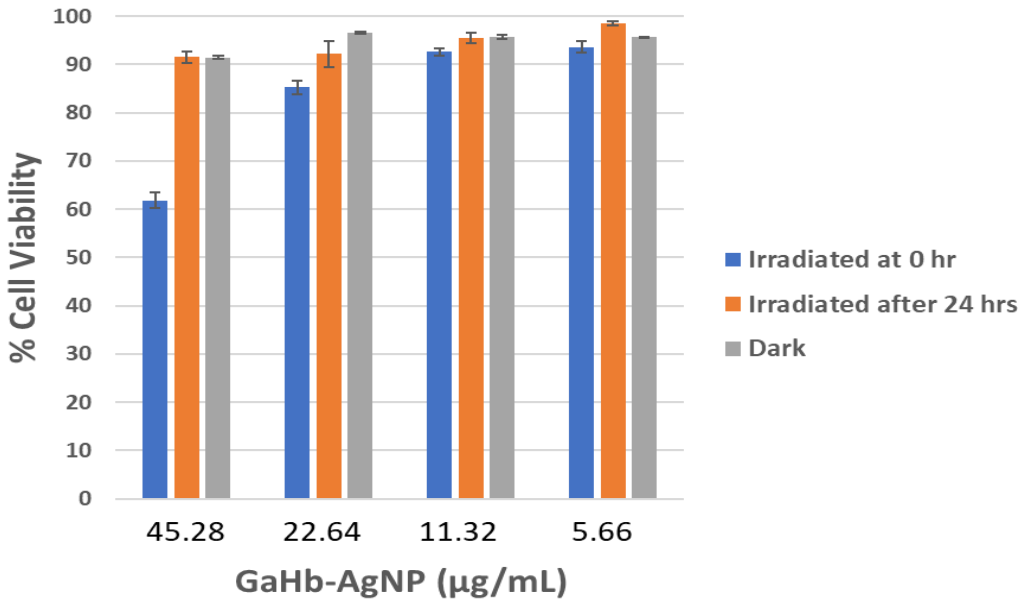

Figure 1.31. Cell viability assay for cytotoxicity against J774 cells. (N = 3). Irradiated cells were incubated for 0 or 24 hours prior to 10-second exposure to 405-nm light (140 mW/cm^2).

1.3 Conclusions

GaHb-AgNPs are effective photosensitizers against *S. aureus* and MRSA. The uptake of GaPpIX by *S. aureus* is diffusion-limited due to its high expression of CSHRs. GaHb-AgNPs also showed potential for the treatment of intracellular MRSA by achieving 80% bacterial kill at 22.64 µg/mL. Within J774 cells, GaHb-AgNPs had a lower level of aPDI activity against *M. abscessus* strains following a 10-second light exposure, suggesting the absence of CSHR for rapid uptake. We did not observe significant aPDI effect against *S. aureus* biofilm by treatment with GaHb-AgNPs or in combination with vancomycin. GaHb-AgNPs exhibit negligible dark toxicity and phototoxicity against keratinocytes and macrophages under aPDI conditions, making them highly attractive for future clinical research or aPDI against topical bacterial infections.

1.4 Materials and Methods

All chemical reagents were obtained from commercial sources and used as received unless otherwise noted. Bovine hemoglobin was obtained from Sigma-Aldrich; 10-nm AgNPs were obtained from NanoComposix. Deionized water was obtained from an ultrafiltration system (Milli-Q, Millipore) with a resistivity >18 MΩ-cm and passed through a 0.22-μm filter to remove particulate matter. Absorbance spectra were collected on a Varian Cary-50 spectrophotometer. DLS and zeta potential data were collected on a ZetaSizer Nano (Malvern Instruments) with data analysis using Zetasizer v.7.12. Transmission electron microscopy (TEM) images were obtained using a Philips CM-10 (FEI) using an accelerating voltage of 100 kV. Synthesis and characterization of GaPpIX was performed as published previously.[114-115]

Preparation and characterization of GaHb. Cofactor-free bovine Hb (apohemoglobin, or apoHb) was prepared as previously reported.[116-117] Briefly, 153 mg of Hb was dissolved at 0 °C in 5 mL of chilled water; the solution was adjusted to pH 2 by dropwise addition of 3 M HCl, then treated with 10 mL of cold ethyl methyl ketone while stirring. The solution was maintained at 0 ºC throughout this process and allowed to stand for 2–3 minutes until a clear separation of layers was observed. The heme was then extracted from the solution, and the aqueous layer containing apoHb was washed extensively with ethyl methyl ketone (4 × 10 mL) to ensure full removal of heme. The apoHb solution was transferred to dialysis tubing (12 kDa MWCO) and dialyzed first against deionized water, then PBS (pH 7.4), then again with pure water. apoHb was lyophilized and stored as a white solid at 4 ºC for future use.

For the preparation of GaHb, 15 mg of apoHb was dissolved at 0 ºC in 10 mL of PBS (pH 6.5, then treated dropwise with 200 μL of chilled 0.01 M NaOH containing 0.6 mg GaPpIX (4 equiv). The reaction mixture was slowly stirred at 0 °C for 3 h, then subjected to centrifugation at 4000 rpm (2700 *g*) for 10 min to remove precipitated proteins. The supernatant was then passed through

a Sephadex-G25 column with 0.01 M PBS (pH 6.3) to remove unbound GaPpIX. The GaHb solution was dialyzed against PBS and deionized water, then lyophilized to yield a pink solid. Insertion of GaPpIX into apoHb was confirmed by UV-visible and CD spectroscopy.[102]

Coating, purification, and characterization of GaHb-AgNPs. A 10-mL aliquot of 10- or 40-nm citrate-stabilized AgNPs (0.02 mg/mL) in sodium citrate buffer (pH 7.7) was centrifuged at 900 *g* for 5 minutes, then decanted to remove residual aggregates. The supernatant with combined with 200 µL of GaHb solution in PBS (1 mg/mL, pH 7.4) and allowed to stir overnight. In the case of 40-nm particles, the mixture was centrifuged at 5700 rpm (3300 *g*) for 20 minutes; the precipitate was then resuspended in 15 mM borate buffer (pH 8.5). In the case of 10-nm particles, higher centrifugation speeds caused the GaHb-AgNPs to aggregate. This problem was solved by using a 100-kDa MWCO Centricon tube and centrifugation at 4000 rpm (2700 *g*) for 5 min, followed by dilution of the residual AgNP suspension in 15 mM borate buffer. The procedure was repeated three times before characterizing the purified GaHb-AgNPs by UV-visible spectroscopy and DLS.

TEM samples with negative staining were prepared by first mixing 20 µL of a GaHb-AgNP suspension with 20 µL of 2% phosphotungstic acid solution and allowing it to stand for 30 minutes. A 10 µL aliquot of this mixture was then deposited onto Formvar-coated Cu grids (400 mesh) and allowed to sit for 25 minutes, followed by blotting the edge with a tissue and drying in air.

Measurement of binding constant between GaPpIX and apoHb In a solid black 96-well plate (Corning Costar), various concentrations (0 nM–20 µM) of apoHb were mixed with 100 nM of GaPpIX (triplicate per concentration tested) and incubated on shaker in the dark at 4 °C for over 4 hours. A Spark 10M multimode microplate reader (Tecan) was used to measure the fluorescence polarization of GaHb at room temperature, with a 405-nm laser for excitation. Fluorescence

emission was measured using a 585-nm filter with a bandwidth of 20 nm. Data were fitted to the Langmuir-Freundlich isotherm model using OriginPro 2017.

Antimicrobial photodynamic inactivation (aPDI). *S. aureus* or MRSA strains were first cultured in tryptic soy broth (TSB) for up to 16 hours at 37 ºC in capped culture tubes, until an optical density of 1.0 was achieved (λ = 600 nm), corresponding to a bacteria concentration of 10^9 cfu/mL. A 100-µL aliquot of bacteria were then added to 10 mL of tryptic soy media containing 3 mM 2,2'-bipyridine and cultured at 37 ºC until an optical density of 0.8 was reached (approximately 4 hours). aPDI was performed using a monochromatic LED array emitting at 405 nm (Rainbow Technologies Systems) with a tunable power density (max. 140 mW/cm^2).

aPDI studies were performed in triplicate using planktonic bacteria at 10^7 cfu/mL in 96-well microtiter plates with variable exposure times to 405-nm irradiation. Colony growth counts were performed in triplicate by the drop-plate method using tryptic soy agar (TSA) plates.[118] In a typical experiment, bacterial suspensions in 96-well plates (10^7 cfu/mL; 50 µL/well) were treated with 50-µL aliquots of GaHb-AgNP solutions with final concentrations ranging from 22–1900 ng/mL in GaPpIX equivalents, followed immediately with exposure to the LED array for 10 seconds. Controls included one set of wells without photosensitizer, and one set of wells with photosensitizer but without light exposure (dark toxicity). Bacterial suspensions from each well were diluted in serial tenfold dilutions (6 rounds) and plated onto agar and incubated for 20 hours at 37 °C. Colonies were counted and reported in colony-forming units per milliliter (cfu/mL).

Flow cytometry analysis of bacterial uptake of GaPpIX by S. aureus. Flow cytometry (FC) was performed on *S. aureus* fixed with paraformaldehyde (2 wt% final concentration) using flow cytometer CytoFLEX S (Beckman Coulter Life Sciences). Paraformaldehyde was introduced at fixed intervals after incubation with GaPpIX. A yellow laser (561 nm) was used for excitation.

Fluorescence emission was measured on the PE channel using a 585-nm filter with a band width of 42 nm. Blank PBS runs were included in between experiments to remove false positives. A region of interest (gate) containing 98% or more of the collected bacterial population was defined using FSC and SSC parameters, and was applied toward all runs. Data were processed using pre-released version of software Kaluza Flow Cytometry Analysis (Beckman Coulter life Sciences).

Eradication of intracellular MRSA. The ability of GaHb-AgNP to reduce the burden of intracellular MRSA was evaluated utilizing previously described methods.[119-120] Murine macrophage cells (J774) were cultured in Dulbecco's Modified Eagle Medium (DMEM) supplemented with 10% FBS at 37 °C in a 5% CO_2 atmosphere. J774 cells were exposed to MRSA USA300 cells at a multiplicity of infection of approximately 10:1. After 1 h of infection, J774 cells were washed with gentamicin (100 µg/mL) to kill extracellular MRSA. GaHb-AgNP was subsequently added to each well at concentrations ranging from 11.3 to 45.28 µg/mL (three replicates per test agent). After 24 hours incubation at 37 °C with 5% CO_2, the test agents were removed and the J774 cells were washed and lysed using 0.1% Triton-X. The solution was serially diluted in phosphate-buffered saline and transferred to TSA plates in order to determine viable MRSA inside the J774 cells. Plates were incubated at 37 ºC for 18–22 h before counting viable colonies. Data are presented as $\log_{10}$ (MRSA cfu/mL) and percent kill in infected J774 cells.

TEM ultrathin cell sample processing. MRSA USA300 cells and J774 cells infected with MRSA USA300 were treated with GaHb-AgNP then fixed over night at 4 °C with 2.5% glutaraldehyde in 0.1 M cacodylate buffer. The cells were washed with cacodylate buffer 3 times then treated with a solution of 1% osmium tetroxide and 0.8% FeCN for 1 hour. The residual osmium tetroxide was rinsed off using water. The cell dehydration process was conducted with 50,

75, 95 and 100% of alcohol. The fixed cells were embedded in flat molds using Embed 812 resin (Electron Microscopy Sciences) with catalyst and left to cure at 70 ºC overnight.

Microtomy was performed in Purdue Life Sciences Microscopy Facility using a Leica Ultracut E for semi-thin and ultrathin sections. Semi-thin sections were cut at 500 nm thickness and heat-fixed onto a glass slide, then stained with Toludine Blue and examined for areas of interest. Final block faces were trimmed down to approximately 1.5 mm x 1 mm, and ultra-thin sections were cut and harvested at 85nm and transferred from the diamond knife boat onto 100-mesh copper/Formvar grids using Perfect Loop (Electron Microscopy Sciences). All sectioning was performed using an ultra 45-degree diamond knife (Diatome). Post-staining of TEM grids was performed with 4% aqueous uranyl acetate for 10 minutes, rinsed twice in two 400 mL of distilled H_20, then treated with 2% lead citrate for 5 minutes.

MRSA biofilm eradication assessment. GaHb-AgNPs and vancomycin hydrochloride (Gold Biotechnology) were examined for their ability to degrade pre-formed, mature staphylococcal biofilms using the microtiter dish biofilm formation assay, following the procedure described in a previous report.[121-122] An overnight culture of MRSA USA300 was diluted 1:100 in culture medium (TSB + 1% glucose) and incubated at 37 °C for 24 h to form a strongly adherent biofilm. The bacterial suspension was removed, and GaHb-AgNPs were added at concentrations ranging from 0.4 to 45.3 μg/mL and/or vancomycin at a concentration range of 0.5 to 64 μg/mL in TSB. GaHb-AgNPs were incubated with the biofilm at 37 °C for 24 h. To quantify the biofilm mass, the bacterial suspension was removed, and wells were washed with phosphate-buffered saline to remove residual planktonic bacteria. An aliquot of 0.1% crystal violet was added to each well to stain the biofilms. After 30 min, wells were washed with sterile water and dried, then de-stained using 100% ethanol prior to quantifying biofilm mass using a spectrophotometer (λ = 595 nm).

Data are presented as percent loss of MRSA USA300 biofilm for each test agent relative to the buffer control wells.

MRSA biofilm inhibition assessment. Vancomycin, GaHb-AgNPs and its components were examined for their ability to inhibit the formation of staphylococcal biofilm using the microtiter plate biofilm formation assay.[123-124] An overnight culture of MRSA USA300 was diluted 1:100 in culture medium (TSB + 1% glucose). Compounds were added in the first row and serially diluted with media containing bacteria, then incubated at 37 °C for 24 hours. In order to quantify biofilm mass, the bacterial suspension (planktonic cells) was removed and wells were washed with phosphate-buffered saline to remove residual planktonic bacteria. An aliquot of 0.1% crystal violet was added to each well to stain the biofilms. After 30 minutes, wells were washed with sterile water and dried, then de-stained using 100% ethanol prior to quantifying biofilm mass using a spectrophotometer (λ = 595 nm). Data are presented as percent inhibition of MRSA USA300 biofilm for each test agent to buffer control wells.

aPDI of GaHb against M. abscessus. Strains were first cultured in Difco Middlebrook 7H9 broth (Becton-Dickinson) enriched with Middlebrook OADC enrichment (Becton-Dickinson) for 3–4 days at 37 ºC in capped culture tubes, until an optical density of 1.0 was achieved (λ = 600 nm). aPDI was performed using a monochromatic LED array emitting at 405 nm with a tunable power density (max. 140 mW/cm^2).

aPDI studies were performed in triplicate using planktonic bacteria at 10^7 cfu/mL in 96-well microtiter plates with various compounds and concentrations. Colony growth counts were performed in triplicate by the drop-plate method using Mycobacteria 7H11 agar base plates (Hardy Diagnostics). In a typical experiment, bacterial suspensions in 96-well plates (10^7 cfu/mL; 100 μL/well) were treated with solutions of GaHb-AgNP or its components with final concentrations

of 20 or 40 μg/mL in AgNP equivalents, or 178.1 or 356.1 nM in GaPpIX equivalents, followed immediately with or without a 10-second exposure to the LED array. Controls included one set of wells with 15 mM borate buffer plus photosensitizer. Bacterial suspensions from each well were diluted in serial tenfold dilutions (6 rounds) and plated onto agar and incubated for 3–4 days at 37 °C. Colonies were counted and reported in colony-forming units per milliliter (cfu/mL).

Toxicity assessment against HaCaT cells. HaCaT cells (AddexBio) were cultured in growth medium (DMEM containing 10% FBS) at 37 ºC in a 5% CO_2 atmosphere, with multiple passages before use. Approximately 10^6 HaCaT cells were plated in a T-25 flask and grown to 70–80% confluence in 5 mL of medium over a period of 1 day. The adherent cells were washed with PBS then released into the media by treatment with 0.25% trypsin/EDTA at room temperature and counted using a hemocytometer. A 0.8-mL suspension containing 10^6 cells was diluted with 7.2 mL of growth medium and added to a 96-well plate in 80-μL aliquots (10^4 cells/well), then incubated for 18–24 hours at 37 ºC. Experimental wells were treated with 20-μL aliquots of 10-nm GaHb-AgNP (40–200 μg/mL), with final concentrations ranging from 5.7 to 45.3 μg/mL. Control wells were treated with 20 μL of 0.005% Triton X-100 in growth medium ($Ctrl^-$) or medium alone ($Ctrl^+$). Cells were incubated with GaHb-AgNPs at 37 ºC at different time intervals (0, 0.5, or 22 hours) to address NP uptake as a variable, then irradiated with a 405-nm LED array for 10 s at 140 mW/cm^2. Wells were immediately treated with 10 μL of MTT reagent (5 mg/mL) then incubated for 4 hours at 37 ºC, followed by 100 μL of detergent solution (10% Triton X-100 + 0.1 M HCl in isopropanol) to halt MTT oxidation and fix the cells. The plate was covered with aluminum foil and left on a rocker overnight at room temperature, then read at 570 nm (main absorbance) and 650 nm (background).

Toxicity assessment against J774 cells. GaHb-AgNPs were assayed against a murine macrophage (J774) cell line to determine their *in vitro* cytotoxicity effect. J774 cells were cultured in growth medium (DMEM containing 10% FBS) at 37 ºC in a 5% CO_2 atmosphere, with multiple passages before use. Approximately 10^6 cells were plated in a T-25 flask and grown to 70–80% confluence in 5 mL of medium until confluent. The adherent cells were washed with PBS then released into the media by treatment with 0.25% trypsin/EDTA at room temperature and counted using a hemocytometer. A 0.8-mL suspension containing 10^6 cells was diluted with 7.2 mL of growth medium and added to a 96-well plate in 80-µL aliquots (10^4 cells/well), then incubated for 2 to 3 days at 37 ºC until confluent. Experimental wells were treated with 20-µL aliquots of 10-nm GaHb-AgNP (40–200 µg/mL), with final concentrations ranging from 5.7 to 45.3 µg/mL. Cells were incubated with GaHb-AgNPs at 37 ºC at different time intervals (0 or 24 hours) to address NP uptake as a variable, then irradiated with a 405-nm LED array for 10 s at 140 mW/cm^2. Wells were immediately treated with 10 µL of MTT reagent (5 mg/mL) then incubated for 4 hours at 37 ºC, followed by 100 µL of detergent solution (10% Triton X-100 + 0.1 M HCl in isopropanol) to halt MTT oxidation and fix the cells. The plate was covered with aluminum foil and left on a rocker overnight at room temperature, then read at 570 nm (peak absorbance) and 650 nm (background).

1.5 References

1. Spellberg, B.; Blaser, M.; Guidos, R. J.; Boucher, H. W.; Bradley, J. S.; Eisenstein, B. I.; Gerding, D.; Lynfield, R.; Reller, L. B.; Rex, J.; Schwartz, D.; Septimus, E.; Tenover, F. C.; Gilbert, D. N., Combating antimicrobial resistance: policy recommendations to save lives. *Clinical Infectious Diseases* **2011,** *52* (5), S397-S428.

2. Slonczewski, J. L., Foster, John W., Microbiology: an evolving science. *W. W. Norton*: **2008;** 1246.

3. Perez, F.; Van Duin, D., Carbapenem-resistant Enterobacteriaceae: a menace to our most vulnerable patients. *Cleveland Clinic Journal of Medicine* **2013,** *80* (4), 225.

4. Antibiotic resistance threats in the United States. *Center for Disease Control and Prevention, U.S. Department of Health and Human Services* **2013**, 112.

5. Nikaido, H., Multidrug resistance in bacteria. *Annual Review of Biochemistry* **2009,** *78*, 119.

6. Lowy, F. D., Staphylococcus aureus infections. *New England Journal of Medicine* **1998,** *339* (8), 520-532.

7. Clement, S.; Vaudaux, P.; Francois, P.; Schrenzel, J.; Huggler, E.; Kampf, S.; Chaponnier, C.; Lew, D.; Lacroix, J.-S., Evidence of an intracellular reservoir in the nasal mucosa of patients with recurrent Staphylococcus aureus rhinosinusitis. *Journal of Infectious Diseases* **2005,** *192* (6), 1023.

8. Bayles, K. W.; Wesson, C. A.; Liou, L. E.; Fox, L. K.; Bohach, G. A.; Trumble, W. R., Intracellular Staphylococcus aureus escapes the endosome and induces apoptosis in epithelial cells. *Infection and Immunity* **1998,** *66* (1), 336.

9. Fowler, T.; Wann, E. R.; Joh, D.; Johansson, S.; Foster, T. J.; Höök, M., Cellular invasion by Staphylococcus aureus involves a fibronectin bridge between the bacterial fibronectin-binding MSCRAMMs and host cell β1 integrins. *European Journal of Cell Biology* **2000,** *79* (10), 672-679.

10. Menzies, B. E.; Kourteva, I., Internalization of Staphylococcus aureus by endothelial cells induces apoptosis. *Infection and Immunity* **1998,** *66* (12), 5994.

11. Nuzzo, I.; Sanges, M. R.; Folgore, A.; Carratelli, C. R., Apoptosis of human keratinocytes after bacterial invasion. *FEMS Immunology and Medical Microbiology* **2000,** *27* (3), 235-240.

12. Peacock, S. J.; Foster, T. J.; Cameron, B. J.; Berendt, A. R., Bacterial fibronectin-binding proteins and endothelial cell surface fibronectin mediate adherence of Staphylococcus aureus to resting human endothelial cells. *Microbiology* **1999,** *145* (12), 3477.

13. Voyich, J. M.; Braughton, K. R.; Sturdevant, D. E.; Whitney, A. R.; Saïd-Salim, B.; Porcella, S. F.; Long, R. D.; Dorward, D. W.; Gardner, D. J.; Kreiswirth, B. N.; Musser, J. M.; Deleo, F. R., Insights into mechanisms used by Staphylococcus aureus to avoid destruction by human neutrophils. *Journal of Immunology* **2005,** *175* (6), 3907.

14. Koziel, J.; Maciag-Gudowska, A.; Mikolajczyk, T.; Bzowska, M.; Sturdevant, D. E.; Whitney, A. R.; Shaw, L. N.; DeLeo, F. R.; Potempa, J., Phagocytosis of Staphylococcus aureus by macrophages exerts cytoprotective effects manifested by the upregulation of antiapoptotic factors. *PLoS ONE* **2009,** *4* (4), e5210.

15. Gresham, H. D.; Lowrance, J. H.; Caver, T. E.; Wilson, B. S.; Cheung, A. L.; Lindberg, F. P., Survival of Staphylococcus aureus inside neutrophils contributes to infection. *Journal of Immunology* **2000,** *164* (7), 3713-3722.

16. Carryn, S.; Chanteux, H.; Seral, C.; Mingeot-Leclercq, M.-P.; Van Bambeke, F.; Tulkens, P. M., Intracellular pharmacodynamics of antibiotics. *Infectious Disease Clinics of North America* **2003,** *17* (3), 615-634.

17. Briones, E.; Isabel Colino, C.; Lanao, J. M., Delivery systems to increase the selectivity of antibiotics in phagocytic cells. *Journal of Controlled Release* **2008,** *125* (3), 210-227.

18. Ranjan, A.; Pothayee, N.; Vadala, T. P.; Seleem, M. N.; Restis, E.; Sriranganathan, N.; Riffle, J. S.; Kasimanickam, R., Efficacy of amphiphilic core-shell nanostructures encapsulating gentamicin in an in vitro salmonella and listeria intracellular infection model. *Antimicrobial Agents and Chemotherapy* **2010,** *54* (8), 3524.

19. Høiby, N.; Bjarnsholt, T.; Givskov, M.; Molin, S.; Ciofu, O., Antibiotic resistance of bacterial biofilms. *International Journal of Antimicrobial Agents* **2010,** *35* (4), 322-332.

20. Lewis, K., Persister cells. *Annual Review of Microbiology* **2010,** *64*, 357.

21. Xu, K. D.; McFeters, G. A.; Stewart, P. S., Biofilm resistance to antimicrobial agents. *Microbiology* **2000,** *146* 547.

22. Archer, N. K.; Mazaitis, M. J.; Costerton, J. W.; Leid, J. G.; Powers, M. E.; Shirtliff, M. E., Staphylococcus aureus biofilms: properties, regulation, and roles in human disease. *Virulence* **2011,** *2* (5), 445-459.

23. Jayasingam, S. D.; Zin, T.; Ngeow, Y. F., Antibiotic resistance in and isolates from Malaysian patients. *International Journal of Mycobacteriology* **2017,** *6* (4), 387.

24. Lee, M.; Sun, P.; Wu, T.; Wang, L.; Yang, C.; Chung, W.; Kuo, A.; Liu, T.; Lu, J.; Chiu, C.; Lai, H.; Chen, N.; Yang, J.; Wu, T., Antimicrobial resistance in Mycobacterium abscessus complex isolated from patients with skin and soft tissue infections at a tertiary teaching hospital in Taiwan. *Journal of Antimicrobial Chemotherapy* **2017,** *72* (10), 2782-2786.

25. Griffith, D. E.; Aksamit, T.; Brown-Elliott, B. A.; Catanzaro, A.; Daley, C.; Gordin, F.; Holland, S. M.; Horsburgh, R.; Huitt, G.; Iademarco, M. F.; Iseman, M.; Olivier, K.; Ruoss, S.; Von Reyn, C. F.; Wallace, R. J.; Winthrop, K., An official ATS/IDSA statement: diagnosis, treatment, and prevention of nontuberculous mycobacterial diseases. *American Journal of Respiratory and Critical Care Medicine* **2007,** *175* (4), 367.

26. Nessar, R.; Cambau, E.; Reyrat, J.; Murray, A.; Gicquel, B., Mycobacterium abscessus: a new antibiotic nightmare. *The Journal of Antimicrobial Chemotherapy* **2012,** *67* (4), 810.

27. Lauro, F. M.; Pretto, P.; Covolo, L.; Jori, G.; Bertoloni, G., Photoinactivation of bacterial strains involved in periodontal diseases sensitized by porphycene–polylysine conjugates. *Photochemical & Photobiological Sciences* **2002,** *1* (7), 468-470.

28. Schastak, S.; Ziganshyna, S.; Gitter, B.; Wiedemann, P.; Claudepierre, T., Efficient photodynamic therapy against Gram-positive and Gram-negative bacteria using THPTS, a cationic photosensitizer excited by infrared wavelength. *PLoS ONE* **2010,** *5* (7), e11674.

29. Huang, L.; Xuan, Y.; Koide, Y.; Zhiyentayev, T.; Tanaka, M.; Hamblin, M. R., Type I and Type II mechanisms of antimicrobial photodynamic therapy: An in vitro study on gram-negative and gram- positive bacteria. *Lasers in Surgery and Medicine* **2012,** *44* (6), 490-499.

30. Reiniers, M. J.; van Golen, R. F.; van Gulik, T. M.; Heger, M., Reactive oxygen and nitrogen species in steatotic hepatocytes: a molecular perspective on the pathophysiology of ischemia-reperfusion injury in the fatty liver. *Antioxidants & Redox Signaling* **2014,** *21* (7), 1119-1142.

31. van Golen, R. F.; van Gulik, T. M.; Heger, M., Mechanistic overview of reactive species-induced degradation of the endothelial glycocalyx during hepatic ischemia/reperfusion injury. *Free Radical Biology and Medicine* **2012,** *52* (8), 1382-1402.

32. Pereira, P. M. R.; Korsak, B.; Sarmento, B.; Schneider, R. J.; Fernandes, R.; Tom, J. P. C., Antibodies armed with photosensitizers: from chemical synthesis to photobiological applications. *Organic & Biomolecular Chemistry* **2015,** *13* (9), 2518-2529.

33. Liu, Y.; Qin, R.; Zaat, S. A. J.; Breukink, E.; Heger, M., Antibacterial photodynamic therapy: overview of a promising approach to fight antibiotic-resistant bacterial infections. *Journal of Clinical and Translational Research* **2015,** *1* (3), 140-167.

34. Rajesh, S.; Koshi, E.; Philip, K.; Mohan, A., Antimicrobial photodynamic therapy: An overview. *Journal of Indian Society of Periodontology* **2011,** *15* (4), 323-327.

35. Agostinis, P.; Berg, K.; Cengel, K. A.; Foster, T. H.; Girotti, A. W.; Gollnick, S. O.; Hahn, S. M.; Hamblin, M. R.; Juzeniene, A.; Kessel, D.; Korbelik, M.; Moan, J.; Mroz, P.; Nowis, D.; Piette, J.; Wilson, B. C.; Golab, J., Photodynamic therapy of cancer: an update. *Ca-A Cancer Journal for Clinicians* **2011,** *61* (4), 250.

36. Soncin, M.; Fabris, C.; Busetti, A.; Dei, D.; Nistri, D.; Roncucci, G.; Jori, G., Approaches to selectivity in the Zn(II)-phthalocyanine-photosensitized inactivation of wild-type and antibiotic-resistant Staphylococcus aureus. *Photochemical and Photobiological Sciences* **2002,** *1* (10), 815-819.

37. Biel, M. A.; Sievert, C.; Usacheva, M.; Teichert, M.; Wedell, E.; Loebel, N.; Rose, A.; Zimmermann, R., Reduction of endotracheal tube biofilms using antimicrobial photodynamic therapy. *Lasers in Surgery and Medicine* **2011,** *43* (7), 586-590.

38. Kashef, N.; Ravaei Sharif Abadi, G.; Djavid, G. E., Phototoxicity of phenothiazinium dyes against methicillin-resistant Staphylococcus aureus and multi-drug resistant Escherichia coli. *Photodiagnosis and Photodynamic Therapy* **2012,** *9* (1), 11-15.

39. Arenas, Y.; Monro, S.; Shi, G.; Mandel, A.; McFarland, S.; Lilge, L., Photodynamic inactivation of Staphylococcus aureus and methicillin-resistant Staphylococcus aureus with Ru(II)-based type I/type II photosensitizers. *Photodiagnosis and Photodynamic Therapy* **2013,** *10* (4), 615-625.

40. Schastak, S.; Gitter, B.; Handzel, R.; Hermann, R.; Wiedemann, P., Improved photoinactivation of Gram-negative and Gram-positive methicillin-resistant bacterial strains using a new near-infrared absorbing meso-tetrahydroporphyrin: A comparative study with a chlorine e6 photosensitizer photolon. *Methods And Findings In Experimental And Clinical Pharmacology* **2008,** *30* (2), 129-133.

41. Ajioka, R. S.; Phillips, J. D.; Kushner, J. P., Biosynthesis of heme in mammals. *BBA - Molecular Cell Research* **2006,** *1763* (7), 723-736.

42. Choby, J. E.; Skaar, E. P., Heme synthesis and acquisition in bacterial pathogens. *Journal of Molecular Biology* **2016,** *428* (17), 3408-3428.

43. Liu, C.; Zhou, Y.; Wang, L.; Han, L.; Lei, J. e.; Ishaq, H.; Xu, J., Mechanistic Aspects of the Photodynamic Inactivation of Vancomycin-Resistant Enterococci Mediated by 5-Aminolevulinic Acid and 5-Aminolevulinic Acid Methyl Ester. *Current Microbiology* **2015,** *70* (4), 528-535.

44. Wachowska, M.; Muchowicz, A.; Firczuk, M.; Gabrysiak, M.; Winiarska, M.; Wanczyk, M.; Bojarczuk, K.; Golab, J., Aminolevulinic Acid (ALA) as a Prodrug in Photodynamic Therapy of Cancer. *Molecules* **2011,** *16* (5), 4140-4164.

45. Warren, C. B.; Karai, L. J.; Vidimos, A.; Maytin, E. V., Pain associated with aminolevulinic acid-photodynamic therapy of skin disease. *Journal of the American Academy of Dermatology* **2009,** *61* (6), 1033-1043.

46. Taslı, H.; Akbıyık, A.; Topaloğlu, N.; Alptüzün, V.; Parlar, S., Photodynamic antimicrobial activity of new porphyrin derivatives against methicillin resistant Staphylococcus aureus. *Journal of Microbiology* **2018,** *56* (11), 828-837.

47. Stojiljkovic, I.; Kumar, V.; Srinivasan, N., Non-iron metalloporphyrins: Potent antibacterial compounds that exploit haem/Hb uptake systems of pathogenic bacteria. *Molecular Microbiology* **1999,** *31* (2), 429.

48. Hijazi, S.; Visca, P.; Frangipani, E., Gallium-Protoporphyrin IX inhibits growth by targeting cytochromes. *Frontiers in Cellular and Infection Microbiology* **2017,** *7*, 12.

49. Arivett, B. A.; Fiester, S. E.; Ohneck, E. J.; Penwell, W. F.; Kaufman, C. M.; Relich, R. F.; Actis, L. A., Antimicrobial activity of Gallium Protoporphyrin IX against Acinetobacter baumannii strains displaying different antibiotic resistance phenotypes. *Antimicrobial Agents and Chemotherapy* **2015,** *59* (12), 7657.

50. Huang, X.; Nakanishi, K.; Berova, N., Porphyrins and metalloporphyrins: Versatile circular dichroic reporter groups for structural studies. *Chirality* **2000,** *12* (4), 237-255.

51. Stojiljkovic, I.; Evavold, B. D.; Kumar, V., Antimicrobial properties of porphyrins. *Expert Opinion on Investigational Drugs* **2001,** *10* (2), 309.

52. Jelić, D.; Tatić, I.; Trzun, M.; Hrvačić, B.; Brajša, K.; Verbanac, D.; Tomašković, M.; Čulić, O.; Antolović, R.; Glojnarić, I.; Weygand-Đurašević, I.; Vladimir-Knežević, S.; Mildner, B., Porphyrins as new endogenous anti-inflammatory agents. *European Journal of Pharmacology* **2012,** *691* (1-3), 251-260.

53. Barona-Castano, J.; Carmona-Vargas, C.; Brocksom, T.; de Oliveira, K., Porphyrins as catalysts in scalable organic reactions. *Molecules* **2016,** *21* (3), 310.

54. Lippert, R.; Shubina, T. E.; Vojnovic, S.; Pavic, A.; Veselinovic, J.; Nikodinovic-Runic, J.; Stankovic, N.; Ivanović-Burmazović, I., Redox behavior and biological properties of ferrocene bearing porphyrins. *Journal of Inorganic Biochemistry* **2017,** *171*, 76-89.

55. Carpenter, B. L.; Feese, E.; Sadeghifar, H.; Argyropoulos, D. S.; Ghiladi, R. A., Porphyrin-cellulose nanocrystals: a photobactericidal material that exhibits broad spectrum antimicrobial activity *Photochemistry and Photobiology* **2012,** *88* (3), 527-536.

56. Naveed Umar, M.; Ur. Rashid, H.; Gul Sayed, M.; Karim, N.; Ghaffar, R.; Antonio Utrera Martines, M.; Shoaib, M., Synthesis and evaluation of analgesic, anti-inflammatory and anti-bacterial activity of synthetic porphyrin derivatives. *Revue Roumaine de Chimie* **2015,** *60* (9), 861-866.

57. Actis, Luis A., Iron transport in bacteria. *The Quarterly Review of Biology* **2005,** *80* (3), 357-357.

58. Maltais, T.; Adak, A.; Younis, W.; Seleem, M.; Wei, A., Label-free detection and discrimination of bacterial pathogens based on hemin recognition. *Bioconjugate Chemistry* **2016,** *27* (7), 1713-1722.

59. Nakonieczna, J.; Kossakowska-Zwierucho, M.; Filipiak, M.; Hewelt-Belka, W.; Grinholc, M.; Bielawski, K., Photoinactivation of Staphylococcus aureus using protoporphyrin IX: the role of haem-regulated transporter HrtA. *Applied Microbiology and Biotechnology* **2016,** *100* (3), 1393-1405.

60. Gat, O.; Zaide, G.; Inbar, I.; Grosfeld, H.; Chitlaru, T.; Levy, H.; Shafferman, A., Characterization of Bacillus anthracis iron- regulated surface determinant (Isd) proteins containing NEAT domains. *Molecular Microbiology* **2008,** *70* (4), 983-999.

61. P. Skaar, E.; Schneewind, O., Iron-regulated surface determinants (Isd) of Staphylococcus aureus: stealing iron from heme. *Microbes and Infection* **2004,** *6* (4), 390-397.

62. Maltais, T. R., I. Rapid detection of pathogenic bacteria with immutable ligands. II. Mechanochemical surface modification of cellulose nanocrystals. *Ph.D. Dissertation, Purdue University* **2015**.

63. Wakeman, C. A.; Stauff, D. L.; Zhang, Y.; Skaar, E. P., Differential activation of Staphylococcus aureus heme detoxification machinery by heme analogues. *Journal of Bacteriology* **2014,** *196* (7), 1335.

64. Tillotson, G. S., Staphylococcus : molecular genetics. *Expert Review of Anti-infective Therapy* **2008,** *6* (6), 849-850.

65. Laakso, H. A.; Marolda, C. L.; Pinter, T. B.; Stillman, M. J.; Heinrichs, D. E., A heme-responsive regulator controls synthesis of staphyloferrin B in Staphylococcus aureus. *The Journal of biological chemistry* **2016,** *291* (1), 29-40.

66. Morales-de-Echegaray, A. V.; Maltais, T. R.; Lin, L.; Younis, W.; Kadasala, N. R.; Seleem, M. N.; Wei, A., Rapid uptake and photodynamic inactivation of Staphylococci by Ga(III)-Protoporphyrin IX. *ACS Infectious Diseases* **2018,** *4* (11), 1564.

67. Chernousova, S.; Epple, M., Silver as Antibacterial Agent: Ion, Nanoparticle, and Metal. Weinheim, **2013;** *52*, 1636-1653.

68. Zhao, G.; Stevens, S., Multiple parameters for the comprehensive evaluation of the susceptibility of Escherichia coli to the silver ion. *Biometals* **1998,** *11* (1), 27-32.

69. Kim, J. S.; Kuk, E.; Yu, K. N.; Kim, J.-H.; Park, S. J.; Lee, H. J.; Kim, S. H.; Park, Y. K.; Park, Y. H.; Hwang, C.-Y.; Kim, Y.-K.; Lee, Y.-S.; Jeong, D. H.; Cho, M.-H., Antimicrobial effects of silver nanoparticles. *Nanomedicine: Nanotechnology, Biology, and Medicine* **2007,** *3* (1), 95-101.

70. Silver, S., Bacterial silver resistance: molecular biology and uses and misuses of silver compounds. *FEMS Microbiology Reviews* **2003,** *27* (2-3), 341-353.

71. Silver, S.; Phung, L.; Silver, G., Silver as biocides in burn and wound dressings and bacterial resistance to silver compounds. *Journal Of Industrial Microbiology & Biotechnology* **2006,** *33* (7), 627-634.

72. Franke, S.; Grass, G.; Nies, D., The product of the ybdE gene of the Escherichia coli chromosome is involved in detoxification of silver ions. *Microbiology-Sgm* **2001,** *147*, 965-972.

73. Chen, X.; Schluesener, H. J., Nanosilver: A nanoproduct in medical application. *Toxicology Letters* **2008,** *176* (1), 1-12.

74. Wijnhoven, S. W. P.; Peijnenburg, W. J. G. M.; Herberts, C. A.; Hagens, W. I.; Oomen, A. G.; Heugens, E. H. W.; Roszek, B.; Bisschops, J.; Gosens, I.; Van De Meent, D.; Dekkers, S.; De Jong, W. H.; Van Zijverden, M.; Sips, A. J. A. M.; Geertsma, R. E., Nano-silver - A review of available data and knowledge gaps in human and environmental risk assessment. *Nanotoxicology* **2009,** *3* (2), 109-138.

75. Moyer, C. A.; Brentano, L.; Gravens, D. L.; Margraf, H. W.; Monafo, W. W., Treatment of large human burns with 0.5% silver nitrate solution. *Archives of Surgery* **1965,** *90* (6), 812-867.

76. Lansdown, A. B. G., Silver. I: Its antibacterial properties and mechanism of action. *Journal of Wound Care* **2002,** *11* (4), 125.

77. Castellano, J.; Shafii, S.; Ko, F.; Donate, G.; Wright, T.; Mannari, R.; Payne, W.; Smith, D.; Robson, M., Comparative evaluation of silver- containing antimicrobial dressings and drugs. *International Wound Journal* **2007,** *4* (2), 139-140.

78. Feng, Q. L.; Wu, J.; Chen, G. Q.; Cui, F. Z.; Kim, T. N.; Kim, J. O., A mechanistic study of the antibacterial effect of silver ions on Escherichia coli and Staphylococcus aureus. *Journal of Biomedical Materials Research* **2000,** *52* (4), 662-668.

79. Lok, C.; Ho, C.; Chen, R.; He, Q.-u.; Yu, W.-i.; Sun, H.; Tam, P. K.; Chiu, J.; Che, C., Proteomic analysis of the mode of antibacterial action of silver nanoparticles. *Journal of Proteome Research* **2006,** *5* (4), 916.

80. Rai, M.; Yadav, A.; Gade, A., Silver nanoparticles as a new generation of antimicrobials. *Biotechnology Advances* **2009,** *27* (1), 76-83.

81. Raimondi, F.; Scherer, G. G.; Kötz, R.; Wokaun, A., Nanoparticles in Energy Technology: Examples from Electrochemistry and Catalysis. *Angewandte Chemie International Edition* **2005,** *44* (15), 2190-2209.

82. Morones, J. R.; Elechiguerra, J. L.; Camacho, A.; Holt, K.; Kouri, J. B.; Ramírez, J. T.; Yacaman, M. J., The bactericidal effect of silver nanoparticles. *Nanotechnology* **2005,** *16* (10), 2346-2353.

83. Lara, H. H.; Ayala-Núñez, N. V.; Ixtepan Turrent, L. d. C.; Rodríguez Padilla, C., Bactericidal effect of silver nanoparticles against multidrug-resistant bacteria. *World Journal of Microbiology and Biotechnology* **2010,** *26* (4), 615-621.

84. Shahverdi, A. R.; Fakhimi, A.; Shahverdi, H. R.; Minaian, S., Synthesis and effect of silver nanoparticles on the antibacterial activity of different antibiotics against Staphylococcus aureus and Escherichia coli. *Nanomedicine: Nanotechnology, Biology and Medicine* **2007,** *3* (2), 168-171.

85. Hu, B.; Cao, X.; Nahan, K.; Caruso, J.; Tang, H.; Zhang, P., Surface plasmon-photosensitizer resonance coupling: an enhanced singlet oxygen production platform for broad-spectrum photodynamic inactivation of bacteria. *Journal of Materials Chemistry B* **2014,** *2* (40), 7073-7081.

86. Wiederrecht, G. P.; Wurtz, G. A.; Hranisavljevic, J., Coherent coupling of molecular excitons to electronic polarizations of noble metal nanoparticles. *Nano Letters* **2004,** *4* (11), 2121-2125.

87. Ahmadov, T. O.; Ding, R.; Zhang, J.; Wang, P.; Tang, H.; Zhang, P., Silver nanoparticle-enhanced hybrid photosensitizer for photoinactivation of multidrug-resistant Staphylococcus aureus (MRSA). *RSC Advances* **2016,** *6* (59), 54318-54321.

88. Bohle, D. S.; Dodd, E. L.; Pinter, T. B. J.; Stillman, M. J., Soluble diamagnetic model for malaria pigment: coordination chemistry of gallium(III)protoporphyrin-IX. *Inorganic Chemistry* **2012,** *51* (20), 10747.

89. Frankenberg, L., Hemoproteins of Enterococcus faecalis. *Ph.D. Dissertation, Luna University* **2003**.

90. Cempel, N.; Guillochon, D., Isolation from bovine haemoglobin of a peptide that might be used as a potential hydrophobic photosensitizer carrier. *Biotechnology and applied biochemistry* **1995,** *21* (3), 287-294.

91. King, M. W., Hemoglobin. *The Medical Biochemistry* **2018**, Web.

92. Linberg, R.; Conover, C. D.; Shum, K. L., Hemoglobin based oxygen carriers: how much methemoglobin is too much? *Artificial Cells, Blood Substitutes, and Biotechnology* **1998,** *26* (2), 133-148.

93. Runyen-Janecky, L., Role and regulation of heme on acquisition in gram-negative pathogens. *Frontiers in Cellular and Infection Microbiology* **2013,** *3*, 55.

94. Linden, J., Blood Safety and Surveillance. *CRC Press*: **2001;** 632.

95. Ascoli, F.; Fanelli, M. R.; Antonini, E., Preparation and properties of apohemoglobin and reconstituted hemoglobins. *Methods in Enzymology* **1981,** *76*, 72.

96. Xu, S.; Kaltashov, I. A., Evaluation of Gallium as a Tracer of Exogenous Hemoglobin–Haptoglobin Complexes for Targeted Drug Delivery Applications. *Journal of The American Society for Mass Spectrometry* **2016,** *27* (12), 2025-2032.

97. Arisaka, F.; Nagai, Y.; Nagai, M., Dimer–tetramer association equilibria of human adult hemoglobin and its mutants as observed by analytical ultracentrifugation. *Methods* **2011,** *54* (1), 175-180.

98. White, S. L., Molecular dissociation of ferrihemoglobin derivatives. *Journal of Biological Chemistry* **1975,** *250* (4), 1263-1268.

99. Yip, Y. K.; Waks, M.; Beychok, S., Influence of prosthetic groups on protein folding and subunit assembly - conformational differences between separated human alpha-globins and beta-globins. *Journal of Biological Chemistry* **1972,** *247* (22), 7237-7244.

100. Hargrove, M. S.; Whitaker, T.; Olson, J. S.; Vali, R. J.; Mathews, A. J., Quaternary structure regulates hemin dissociation from human hemoglobin. *Journal of Biological Chemistry* **1997,** *272* (38), 17385-17389.

101. Jeppu, G. P.; Clement, T. P., A modified Langmuir-Freundlich isotherm model for simulating pH-dependent adsorption effects. *Journal of Contaminant Hydrology* **2012,** *129-130*, 46-53.

102. Morales-de-Echegaray, A. V., Antimicrobial photodynamic therapy with Ga-protoporphyrin derivatives against pathogenic bacteria. *Ph.D. Dissertation, Purdue University* **2018**.

103. Rollin, G.; Tan, X.; Tros, F.; Dupuis, M.; Nassif, X.; Charbit, A.; Coureuil, M., Intracellular survival of Staphylococcus aureus in endothelial cells: a matter of growth or persistence. *Frontiers in Microbiology* **2017,** *8*, 1354.

104. Kshetry, A. O.; Pant, N. D.; Bhandari, R.; Khatri, S.; Shrestha, K. L.; Upadhaya, S. K.; Poudel, A.; Lekhak, B.; Raghubanshi, B. R., Minimum inhibitory concentration of vancomycin to methicillin resistant Staphylococcus aureus isolated from different clinical samples at a tertiary care hospital in Nepal. *Antimicrobial Resistance and Infection Control* **2016,** *5*, 27.

105. Shannon, A. N.; Susan, E. B.; Philip, M. P.; Kate, M.; Kevin, L. W., Treatment of Mycobacterium abscessus infection. *Emerging Infectious Disease Journal* **2016,** *22* (3), 511.

106. Cheng, A.; Sun, H.; Tsai, Y.; Wu, U.; Chuang, Y.; Wang, J.; Sheng, W.; Hsueh, P.; Chen, Y.; Chang, S., Evaluation of Povidone-Iodine and Chlorhexidine against outbreak and nonoutbreak strains of Mycobacterium abscessus using standard quantitative suspension and carrier testing. *Antimicrobial Agents and Chemotherapy* **2018,** *62* (1), e01364-17.

107. Atkins, L. B.; Gottlieb, L. T., Skin and soft tissue infections caused by nontuberculous mycobacteria. *Current Opinion in Infectious Diseases* **2014,** *27* (2), 137-145.

108. Hernandez-Garduno, E.; Elwood, R. K., Increasing incidence of nontuberculous mycobacteria, Taiwan, 2000-2008. *Emerging Infectious Diseases* **2010,** *16* (6), 1047.

109. Chao, A.; Sieminski, P. J.; Owens, C. P.; Goulding, C. W., Iron acquisition in Mycobacterium tuberculosis. *Chemical Reviews* **2018,** *119* (2).

110. De Voss, J. J.; Rutter, K.; Schroeder, B. G.; Barry, C. E., III, Iron acquisition and metabolism by Mycobacteria. *The Journal of Bacteriology* **1999,** *181* (15), 4443.

111. Hamanaka, R. B.; Glasauer, A.; Hoover, P.; Yang, S.; Blatt, H.; Mullen, A. R.; Getsios, S.; Gottardi, C. J.; DeBerardinis, R. J.; Lavker, R. M., Mitochondrial reactive oxygen species promote epidermal differentiation and hair follicle development. *Sci. Signal.* **2013,** *6* (261), ra8-ra8.

112. Dunnill, C.; Patton, T.; Brennan, J.; Barrett, J.; Dryden, M.; Cooke, J.; Leaper, D.; Georgopoulos, N. T., Reactive oxygen species (ROS) and wound healing: the functional role of ROS and emerging ROS- modulating technologies for augmentation of the healing process. *International Wound Journal* **2017,** *14* (1), 89-96.

113. Hole, P. S.; Pearn, L.; Tonks, A. J.; James, P. E.; Burnett, A. K.; Darley, R. L.; Tonks, A., Ras-induced reactive oxygen species promote growth factor–independent proliferation in human CD34+ hematopoietic progenitor cells. *Blood* **2010,** *115* (6), 1238-1246.

114. Bohle, D. S.; Dodd, E. L.; Pinter, T. B. J.; Stillman, M. J., Soluble diamagnetic model for malaria pigment: Coordination chemistry of gallium (III) protoporphyrin-IX. *Inorganic chemistry* **2012,** *51* (20), 10747-10761.

115. Maltais, T. R.; Adak, A. K.; Younis, W.; Seleem, M. N.; Wei, A., Label-Free Detection and Discrimination of Bacterial Pathogens Based on Hemin Recognition. *Bioconjugate chemistry* **2016,** *27* (7), 1713-1722.

116. Ascoli, F.; Fanelli, M. R. R.; Antonini, E., [5] Preparation and properties of apohemoglobin and reconstituted hemoglobins. *Methods in enzymology* **1981,** *76*, 72-87.

117. Zhang, L.; Li, S.; Dong, M.; Jiang, Y.; Li, R.; Zhang, S.; Lv, X.; Chen, L.; Wang, H., Reconstituting redox active centers of heme-containing proteins with biomineralized gold toward peroxidase mimics with strong intrinsic catalysis and electrocatalysis for H 2 O 2 detection. *Biosensors and Bioelectronics* **2017,** *87*, 1036-1043.

118. Herigstad, B.; Hamilton, M.; Heersink, J., How to optimize the drop plate method for enumerating bacteria. *Journal of Microbiological Methods* **2001,** *44* (2), 121-129.

119. Mohamed, M. F.; Abdelkhalek, A.; Seleem, M. N., Evaluation of short synthetic antimicrobial peptides for treatment of drug-resistant and intracellular Staphylococcus aureus. *Scientific Reports* **2016,** *6*, 29707.

120. Hagras, M.; Abutaleb, N. S.; Ali, A. O.; Abdel-Aleem, J. A.; Elsebaei, M. M.; Seleem, M. N.; Mayhoub, A. S., Naphthylthiazoles: targeting multidrug-resistant and intracellular Staphylococcus aureus with biofilm disruption activity. *ACS infectious diseases* **2018,** *4* (12), 1679-1691.

121. Kotb, A.; Abutaleb, N. S.; Seleem, M. A.; Hagras, M.; Mohammad, H.; Bayoumi, A.; Ghiaty, A.; Seleem, M. N.; Mayhoub, A. S., Phenylthiazoles with tert-Butyl side chain: Metabolically stable with anti-biofilm activity. *European journal of medicinal chemistry* **2018,** *151*, 110-120.

122. Kotb, A.; Abutaleb, N. S.; Hagras, M.; Bayoumi, A.; Moustafa, M. M.; Ghiaty, A.; Seleem, M. N.; Mayhoub, A. S., tert-Butylphenylthiazoles with an oxadiazole linker: a novel orally bioavailable class of antibiotics exhibiting antibiofilm activity. *RSC Advances* **2019,** *9* (12), 6770-6778.

123. AbdelKhalek, A.; Abutaleb, N. S.; Mohammad, H.; Seleem, M. N., Repurposing ebselen for decolonization of vancomycin-resistant enterococci (VRE). *Plos One* **2018,** *13* (6), e0199710.

124. AbdelKhalek, A.; Abutaleb, N. S.; Elmagarmid, K. A.; Seleem, M. N., Repurposing auranofin as an intestinal decolonizing agent for vancomycin-resistant enterococci. *Scientific Reports* **2018,** *8* (1), 8353.

CHAPTER 2. SYNTHESIS AND PROPERTIES OF MAGNETIC GOLD NANOPARTICLES

2.1 Introduction

Hybrid nanomaterials that support multiple functions have received increasing interest for nanomedicine applications. Among them, the two most popular materias are gold and iron oxide. Both gold and iron oxide are well known for their high biocompatibility and are frequently utilized in research applications involving biosensing and nanomedicine.[1-4] The surface chemistry of gold nanoparticles (AuNPs) is well established.[5-6] AuNPs can be fabricated to absorb or scatter light at visible to near-infrared wavelengths, the latter having relatively high transmittivity through biological tissues for applications in biological imaging or photo-activated therapies.[7-8] Iron oxide NPs exist in various forms and have been used as medicines for treating chronic anemia (e.g. ferumoxytol).[9] Iron oxide NPs with superparamagnetic properties have also been developed for other biomedical applications such as contrast agents for magnetic resonance imaging,[10] as transducers for magnetic hyperthermia,[11-12] and as carriers for field-directed drug delivery.[10, 13]

Bulk magnets have multiple ferromagnetic domains (Figure 2.1), and their magnetization (M) is the vector sum of all domains.[14] When an exernal magnetic field (H) is applied to a ferromagnetic material, M increases with H until it reaches saturation (M_S, Figure 2.2). In many cases, these domains do not fully return to their original orientations when H is lowered to zero. This phenomenon is reflected in the magnetization curve as a hysteresis loop (Figure 2.2).[14-16] The remanent megnetization (M_R) can be nullified by applying a coercive field H_C in the opposite direction to the initially applied field.[16]

Superparamagnetic materials can also be magnetized by an applied magnetic field, but do not retain their magnetic moment when the external field is removed.[14] Several types of iron-oxide

NPs show superparamagnetism at room temperature, namely Fe_3O_4 (magnetite) and γ-Fe_2O_3 (maghemite). Supermagnetic iron-oxide NPs typically have no hysteresis loop, but have much larger magnetic susceptibilities than that of paramagnetic materials.[14] The unique combination of these properties makes it possible to use localized magnetic field gradients to concentrate NPs at a specific site to enhance applications in drug delivery.[13, 17]

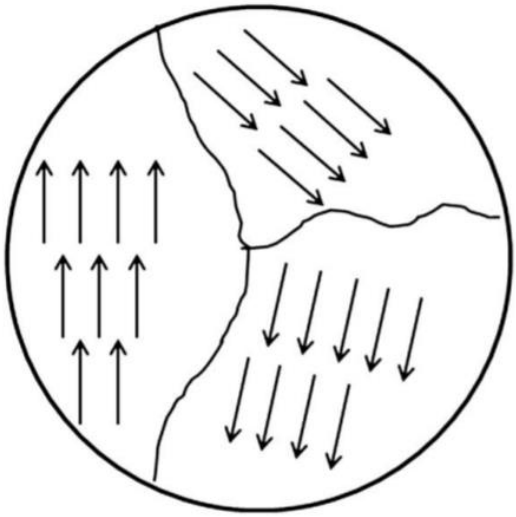

Figure 2.1. Magnetic domains in a bulk ferromagnetic material. Adapted from Teja *et al*.[14]

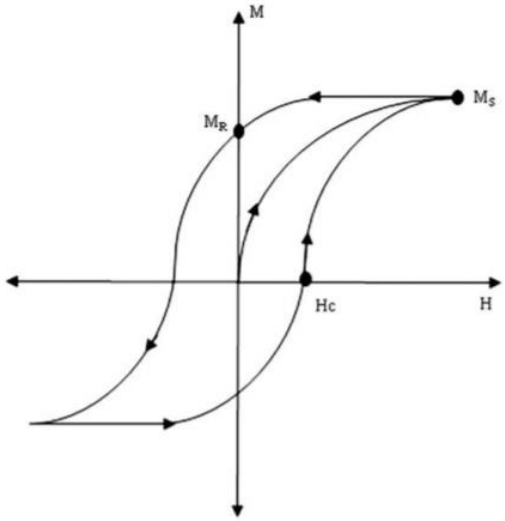

Figure 2.2. Theoretical model of magnetization *M* as a function of magnetic field *H*. Adapted from Teja *et al*.[14]

Magnetic gold nanoparticles (MGNPs) are composites of colloidal Au and iron oxide. The hybrid physical peoperties of MGNPs offer greater potential for innovative nanotechnologies. Specifically, MGNPs can integrate plasmon-enhanced activity with magnetomotive function to support novel sensor and imaging modalities or nano-manufacturing processes. In addition, MGNPs have been used to support magnetomotive versions of surface-enhanced Raman scattering (SERS) capable of detecting trace analytes at picomolar levels,[18-22] and dynamic modes of darkfield imaging for enhanced contrast in environments with intrinsically high noise.[23-25] Recently, MGNPs have been used as laser-activated "drill bits" that can generate high-aspect ratio channels in thermoplastic films and glass, with etch rates accelerated by magnetic field gradients.[26]

To support the transition from proof-of-concept studies to practical nanotechnologies, one requires a synthesis method of MGNPs that is both scalable and sustainable: reaction conditions should be efficient, and minimize the production of hazardous or toxic waste. Previous work from our lab has established a method of synthesizing Au–iron oxide NPs that can be performed in water using mild reaction conditions with low environmental impact.[22, 27] The mean diameter of these synthesized MGNPs was 100 nm.[23] However, the conversion of gold chloride into MGNPs was performed on a small scale and was relatively inefficient, and the removal of residual iron oxide was performed using dithiocarbamate salts. Although dithiocarbamates are excellent ligands for coordination and surface chemistry,[28-29] using them on a large scale increases the amount of hazardous waste generated, which is less appealing from the perspective of green chemistry.[30-31]

Here we optimized the synthesis method with an improved sustainability profile, and also increased the reproducibility and scale of this reaction using a low gold to iron ratio while maintaining control over particle size distributions. Moreover, this protocol allows the removal of residual iron oxide under milder conditions using generally regarded as safe (GRAS) chemicals.

Attenuated total reflectance infrared (ATR-IR) spectroscopy and Raman spectroscopy indicates that the cleansing step does not affect the optical properties of the synthesized MGNPs. Characterization of MGNP microstructure by scanning transmission electron microscopy (STEM) with energy-dispersive X-ray (EDX) analysis establishes their existence as true nanocomposites of gold and iron oxide, rather than as core–shell structures which has been commonly assumed in earlier studies of Au–iron oxide NPs.[3-4, 18-21, 24, 32-44] Variable-temperature magnetization studies show that although MGNPs exhibit superparamagnetism at room temperature, their magnetic behavior under field-cooled (FC) and zero field-cooled (ZFC) conditions is surprisingly similar to that of AuNPs, but with increased magnetization by 3 orders of magnitude. We postulate that the ferromagnetic properties of gold are enhanced by doping with iron oxide.

2.2 Results and Discussion

In previous work, we established a stepwise method for converting colloidal Fe_3O_4 (prepared by co-precipitation) and gold chloride into composite MGNPs on a small scale (<20 mL) by using L-histidine to mediate the adsorption of $AuCl_4$ ions, followed by nucleation and seeded growth by the stepwise addition of *N*-methylhydroxylamine (NMH).[22,27] While this procedure has potential for scalable synthesis, inadequate control over addition or mixing compromises both reproducibility and reaction efficiency. In this work, we describe methods of synthesizing MGNPs with improved reproducibility and control over size and magnetization (Scheme 2.1). The revised synthesis conditions also minimize the use of hazardous reagents and can be performed using scalable processes.

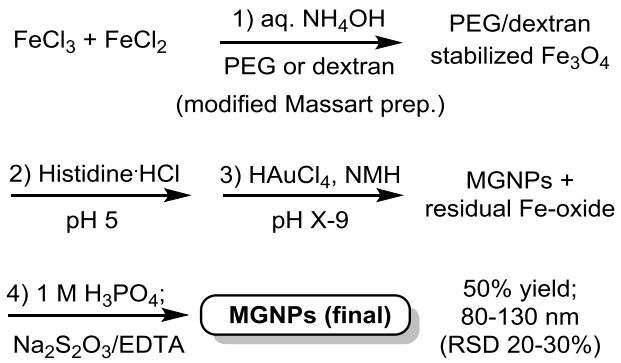

Scheme 2.1. Aqueous synthesis and purification of magnetic gold nanoparticles (MGNPs). EDTA = ethylenediaminetetraacetate; NMH = *N*-methylhydroxylamine. RSD = relative standard deviation.

2.2.1 Scalable Preparation of MGNPs

The synthesis begins with the co-precipitation of colloidal Fe_3O_4 from mixtures of aqueous $FeCl_3$ and $FeCl_2$, a procedure commonly referred to as the Massart method.[45] This economical and green chemistry produces superparamagnetic Fe_3O_4 in high yields with low amounts of waste, although often at the expense of particle size and dispersion control. In this work, co-precipitation generates a reliable and practical feedstock of Fe_3O_4 with crystalline domains on the order of 5 nm.[27] Solutions are deaerated to minimize premature oxidation. For best results, slow mixing with immersion in an ultrasonic bath helps to disperse the co-precipitated Fe_3O_4.

The colloidal Fe_3O_4 dispersions are stabilized with a conditioning polymer, an important factor in aqueous MGNP synthesis. Previously, we found that colloidal Fe_3O_4 treated with polyethylene glycol having a terminal dithiocarbamate (PEG-DTC, 5 kDa) led to the formation of MGNPs with a mean size of 100 nm, with the notion that chemisorptive PEG chains helped to stabilize MGNP dispersions during reduction and particle growth.[22, 27] However, other nonionic polymers and polyelectrolytes can also be employed as peptizing agents for co-precipitated Fe_3O_4, which suggests that chemisorption might not be necessary for MGNP synthesis. To test this, colloidal

Fe_3O_4 was stabilized with polyethylene glycol (PEG), dextran, polyvinylpyrrolidone (PVP), or one of several polyelectrolytes, treated with histidine and $AuCl_4$ ions using a Au:Fe mole ratio of 9:1, then reduced with NMH on a 5-mL scale (Scheme 2.1, steps 3–4). Most of these reactions yielded submicron particles with large variations in mean particle size and dispersity, as measured by their relative standard deviations (RSD; Table 2.1 and Figure 2.3, condition A). Significant amounts of non-magnetic GNPs were also produced, which became evident after harvesting MGNCs with a handheld NdFeB magnet.

Size control and synthetic efficiency were improved by removing excess polymer and histidine from the conditioned Fe_3O_4, prior to treatment with $AuCl_4$ ions (Figure 2.3, condition B). The supernatant of these solutions was less tinted after magnetic precipitation, indicating fewer non-magnetic GNPs and more efficient conversion of $AuCl_4$ into MGNPs. This step also increased the speed of MGNP formation, as judged by the onset of plasmon-resonant absorption during NMH addition, implying that MGNP nucleation and growth in condition A was significantly delayed due to competition from soluble Au–histidine complexes. We thus conclude that nonionic polymers without chemisorptive end groups can be used to stabilize colloidal Fe_3O_4 for MGNP synthesis but requires the added step of removing excess polymer and histidine prior to adding $AuCl_4$.

Table 2.1. Stabilizing polymers tested in MGNP synthesis at different Au:Fe mole ratios. (A) Au:Fe mole ratio = 9:1, in the presence of 1 wt% polymer and 1 mg/mL histidine; (B) Au:Fe mole ratio = 9:1, conditioned Fe_3O_4 washed prior to reaction; (C) Au:Fe mole ratio = 4:1, conditioned Fe_3O_4 washed prior to adding $AuCl_4$. [a] 15 wt% polymer. [b] 0.015 wt% polymer. [c] A weak magnetic response was observed, suggesting low incorporation of Fe. [d] Small sample size ($N < 10$). PAA = polyacrylic acid; PLH = poly-L-histidine; PSS = polystyrenesulfonate. All reactions were performed on a 5 mL scale in test tubes, with manual addition of reagents.

Reaction Condition[§]	Stabilizing Polymer	Mean size (TEM)	RSD
[Au:Fe] = 9 (A)	PEG, 5 kDa	550 nm	20%
	Dextran, 8 kDa [a]	560 nm [c]	28%
	Dextran, 50 kDa	260 nm	>30%[d]
	Dextran, 100 kDa [a]	465 nm	>30%
	PAA, 1.2 kDa [b]	1.2 μm [c]	29%
	Pectin, >100 kDa [b]	500 nm	23%
	PLH, 5–25 kDa	235 nm	27%
	PSS, 70 kDa	360 nm	>30%[d]
	PVP, 50 kDa	780 nm	15%
[Au:Fe] = 9 (B)	PEG, 5 kDa	117 nm	21%
	PSS, 70 kDa	150 nm	22%
	PVP, 50 kDa	62 nm	24%
[Au:Fe] = 4 (C)	PEG, 5 kDa	170 nm	13%
	Dextran, 50 kDa	136 nm	31%
	Dextran, 100 kDa	290 nm	25%
	PLH, 5–25 kDa	107 nm	30%
	PVP, 50 kDa	109 nm	21%

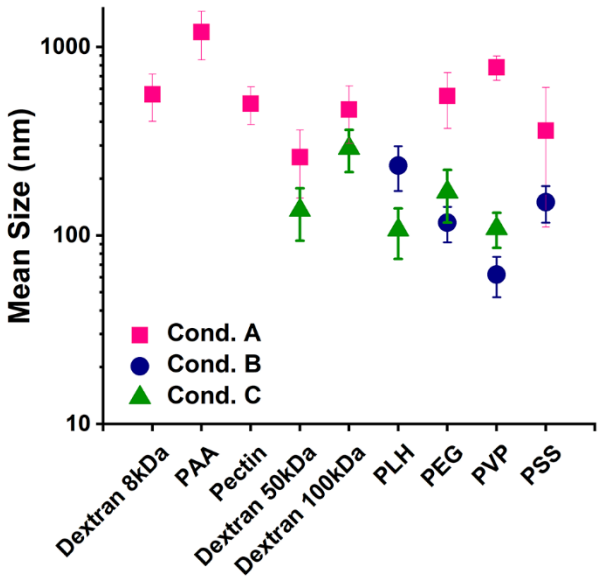

Figure 2.3. Stabilizing polymers tested in MGNP synthesis at different Au:Fe mole ratios. (A) Au:Fe mole ratio = 9:1, in the presence of 1 wt% polymer and 1 mg/mL histidine; (B) Au:Fe mole ratio = 9:1, conditioned Fe_3O_4 washed prior to reaction; (C) Au:Fe mole ratio = 4:1, conditioned Fe_3O_4 washed prior to adding $AuCl_4$.

Prior studies on MGNP synthesis indicated that the final Au:Fe mole ratio was much higher than the mole ratio based on initial $AuCl_4$ and Fe_3O_4 (35.5 versus 9, respectively).[27] To determine whether MGNPs could be synthesized using less $AuCl_4$, we reduced the initial Au:Fe mole ratio from 9:1 to 4:1 and examined the effect of several different stabilizing polymers on a 5-mL scale (Figure 2.3, Condition C). These reactions produced MGNPs with mean sizes larger than those prepared using condition B, but still smaller than those prepared using condition A. Furthermore, magnetic precipitation resulted in a colorless supernatant, indicating complete conversion of $AuCl_4$ into MGNPs. Among the nonionic polymers tested, PEG (5 kDa) and was observed to provide better control over MGNP size dispersity and shape than dextran (50 or 100 kDa) or PVP (50 kDa) (Figure 2.4). Poly-L-histidine (PLH), which has been shown to nucleate the growth of ultrathin layers of Au on magnetic NPs,[44] was also effective for MGNP synthesis but less appealing than the combination of PEG and histidine from the perspective of cost and scalability.

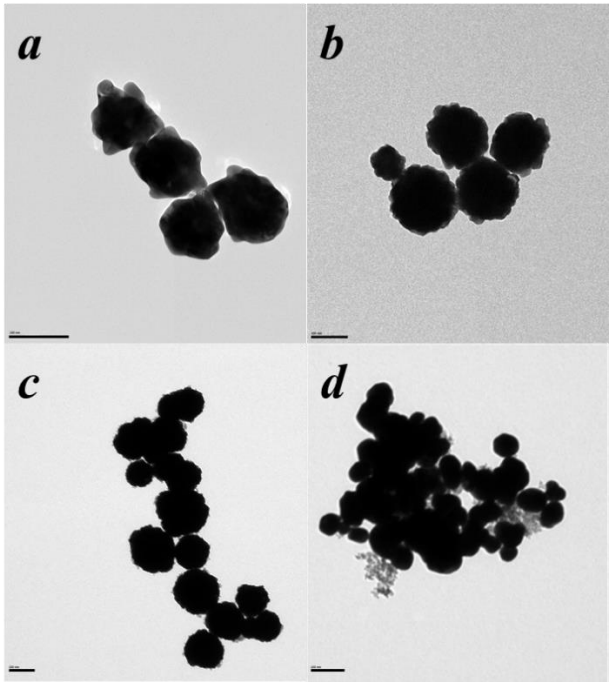

Figure 2.4. (a) TEM image of MGNPs prepared from $AuCl_4$ and colloidal Fe_3O_4 conditioned with 5-kDa PEG and L-histidine ([Au:Fe] = 9). (b–d) TEM images of MGNPs prepared from $AuCl_4$ and colloidal Fe_3O_4 stabilized by (b) 5-kDa PEG, (c) 50-kDa dextran, or (d) 50-kDa PVP ([Au:Fe] =4). All reactions were performed on a 5-mL scale; MGNPs were subjected to a cleaning process prior to TEM analysis. Scale bars: 100 nm.

Subsequent refinements were conducted on a larger scale using a mechanical stirrer and a syringe pump for controlled addition of reducing agent, which improved reproducibility between reaction batches. Use of an overhead mechanical stirrer at constant speed (150 rpm) and addition of NMH solution at constant rate (2.5–5.0 mL/h) removed many of the variations introduced by manual mixing and addition on a small (test tube) scale. This enabled us to adjust reaction parameters in a more systematic fashion, and to establish well-defined conditions for scalable MGNP synthesis.

Mechanically stirred reactions were first performed on a 20-mL scale using 5-kDa PEG as a conditioning polymer and using Au:Fe mole ratios of 4:1 or 2:1 (Table 2.2 and Figure 2.5 Condition D). The latter condition produced MGNPs with mean sizes near 100 nm and without

formation of nonmagnetic GNPs. Increasing the reaction scale to 50 mL with further reductions in Au:Fe mole ratio produced MGNPs below 100 nm, albeit with broader size dispersity. In particular, the reaction condition with the lowest Au:Fe mole ratio used (1:2) proved to be reliable: an analysis of 13 independent syntheses showed that MGNPs were produced with an average size slightly below 100 nm (Figure 2.6; standard error = 14.8%), and with a RSD below 30% for any given batch. Switching 5-kDa PEG to a higher molecular weight polymer (20-kDa PEG, 50-kDa dextran) resulted in larger MGNPs without improving size dispersity. Lastly, we tested our optimized conditions on a 250-mL scale, which yielded MGNPs of similar size and dispersity (Figure 2.5, Condition F). While further improvements in size control are desirable, we conclude that the conditioning of colloidal Fe_3O_4 with 5-kDa PEG and L-histidine are sufficient to support the scalable synthesis of MGNPs.

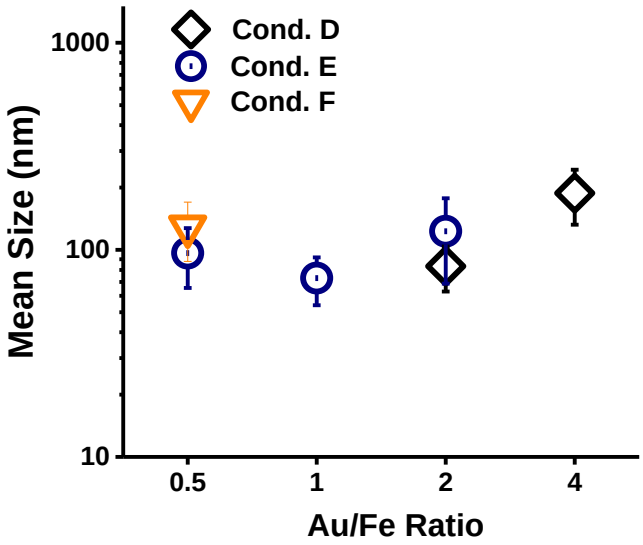

Figure 2.5. MGNP synthesis using PEG, mechanical stirring and continuous addition of reducing agent, at different scales and Au:Fe mole ratios. Reactions were mixed in beakers with an overhead stirrer operating at 150 rpm; conditioned Fe_3O_4 washed prior to reaction. Condition D: 20 mL scale, rate of NMH addition = 2.5 mL/h. Condition E: 50 mL scale, rate of NMH addition = 5.0 mL/h. Condition F: 250 mL scale, rate of NMH addition = 5.0 mL/h.

Table 2.2. MGNP synthesis using mechanical stirring and continuous addition of reducing agent, at different scales and Au:Fe mole ratios. Reactions were mixed in beakers with an overhead stirrer operating at 150 rpm; conditioned Fe_3O_4 washed prior to reaction. (A) rate of NMH addition = 2.5 mL/h. (B) rate of NMH addition = 5.0 mL/h. [a] Mean values from 14 independent experiments (standard error 27%).

Reaction scale	Reaction Condition	Stabilizing Polymer	Mean size (TEM)	RSD
20 mL	[Au:Fe] = 4	PEG, 5 kDa	170 nm	13%
(A)		PEG, 5 kDa	(150-200)	
	[Au:Fe] = 2	PEG, 5 kDa	(50-80)	
		PEG, 5 kDa	(100)	
50 mL	[Au:Fe] = 2	PEG, 5 kDa	123 nm	>30%
(B)	[Au:Fe] = 1	PEG, 5 kDa	73 nm	>30%
	[Au:Fe] = 0.5	PEG, 5 kDa	97 nm[a]	27% [a]
		PEG, 20 kDa	150 nm	>30%
		Dextran, 50 kDa	178 nm	29%
250 mL	[Au:Fe] = 0.5	PEG, 5 kDa	129 nm	>30%

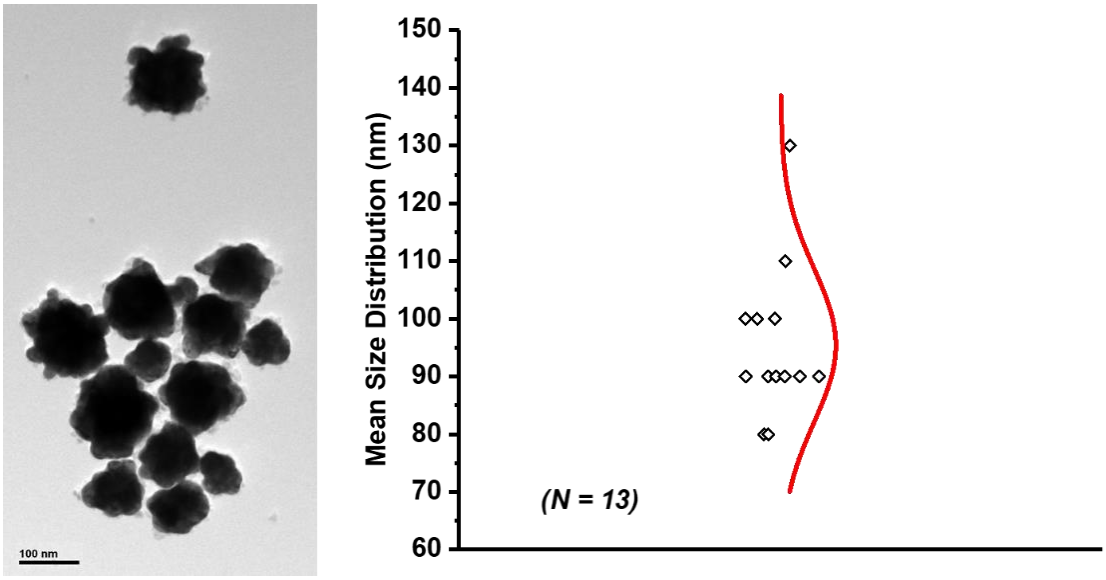

Figure 2.6. TEM image and size distribution analysis of MGNPs synthesized with constant mechanical stirring and reagent addition ([Au:Fe] = 0.5). Reactions were performed on a 50-mL scale. Scale bar: 100 nm

2.2.2 Removing Residual Iron Oxide from MGNPs

While the synthesis of MGNPs is efficient with respect to $AuCl_4$, considerable amounts of iron oxide are left over at the end of the reaction, much of which is physically adsorbed onto MGNP surfaces (Figure 2.7a). The residual iron oxide is presumed to be mostly Fe_3O_4, but is also likely to include various Fe(III) oxides and oxyhydroxides, which are well known to form insoluble deposits.[46] In previous studies, residual iron oxide was effectively removed by treatment with bis(2-hydroxyethyl)dithiocarbamate (DTC),[22, 27] formed *in situ* by the addition of diethanolamine to CS_2.[47] This deferration procedure, while simple in operation, has the drawback of introducing toxic compounds that raise the burden and cost of waste disposal, and is less compatible with efforts to improve the sustainability of scalable process chemistry. We thus examined alternative conditions for cleansing MGNPs of residual iron oxide, focusing on chemicals with GRAS status.

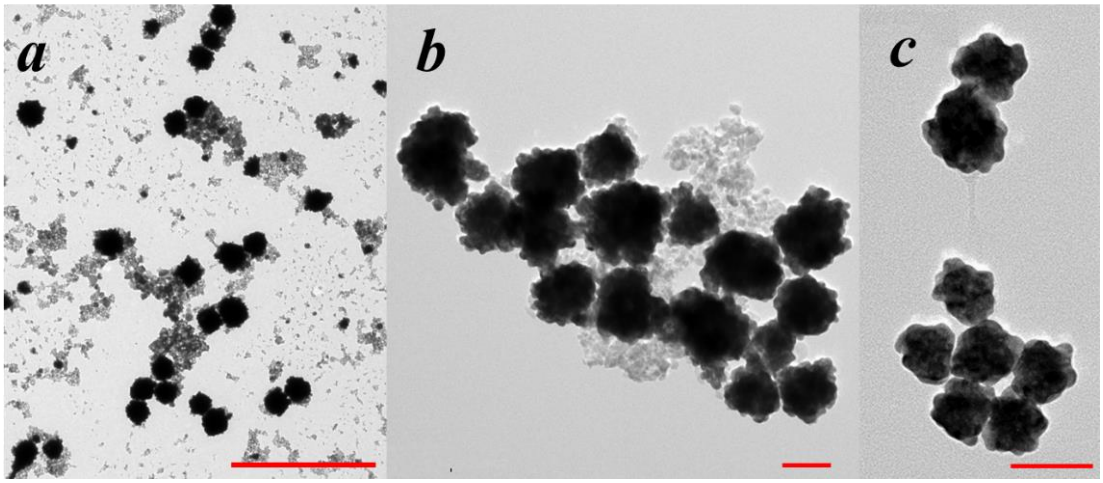

Figure 2.7. TEM images of (a) MGNPs isolated after $AuCl_4$ reduction, prior to removal of leftover iron oxide; (b) MGNPs with residual iron oxide deposits, after 2-h exposure to 0.5 M phosphoric acid; (c) MGNPs after 2-day exposure to 1 mM Na_2–EDTA and 10 mM $Na_2S_2O_3$ at room temperature. Scale bar: (a) 1 μm and (b, c) 100 nm.

Methods for removing iron oxide deposits often employ polyprotic acids to aid their dissolution as iron salts.[46, 48] An initial survey of different acids at various strengths revealed tradeoffs between selective iron oxide etching from MGNP surfaces and complete dissolution, the latter being significant at pH values below 1. We found 0.1–0.5 M H_3PO_4 to provide the best overall outcomes, however many samples contained residual iron oxide that resisted acid dissolution, suggestive of Fe(III) oxide (Figure 2.7b). Further removal of residual iron oxide could be achieved under mildly basic conditions by redispersing partially cleansed MGNPs in EDTA solutions, driven by the formation and solubilization of Fe–EDTA complexes. This approach afforded cleaner MGNPs, but also resulted in a significant loss of particles with irreversible aggregation (Figure 2.8). We then examined the effect of adding thiosulfate, a reducing agent that can reduce Fe(III) ions and enhance their extraction from iron ores.[49] The addition of 10 mM $Na_2S_2O_3$ accelerated the etching of residual iron oxide deposits, with efficient removal achieved using 1 mM EDTA under ambient conditions (Figure 2.7c). The $Na_2S_2O_3$ -EDTA etching condition is sufficiently mild that most of the surface iron oxide can be removed without affecting MGNP size or structure. It is worth noting that the combination of thiosulfate and EDTA also has some capacity for etching Au but is retarded by the affinity of EDTA for Fe ions.[50] On the other hand, as will be discussed further below, a small amount of iron oxide can persist even after prolonged treatment times; we suspect these to be hematite or goethite, which are well known to be more resistant to dissolution than other iron oxide species.[51] This represents a common tradeoff between the use of GRAS chemicals for greater sustainability, and the use of stronger reagents for efficient cleaning. For example, the complete removal of iron oxide can be achieved by treatment with dithiocarbamate salts, but at the expense of producing toxic waste.[22, 27]

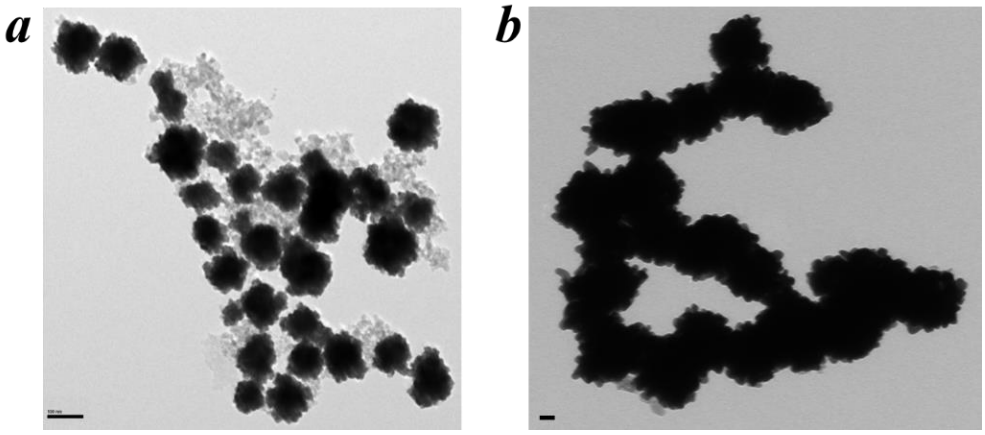

Figure 2.8. TEM images of (a) MGNPs with residual iron oxide deposits, after 2-h exposure to 0.5 M phosphoric acid; (b) acid treated MGNPs after 1-hour incubation in 1 mM Na_2-EDTA at 60 °C. Scale bars: 100 nm.

2.2.3 Characterization of MGNPs

Cleaned MGNPs could be redispersed upon treatment with thiolated PEG (5-kDa) and characterized as stable colloidal suspensions. Although MGNPs generated using a Au:Fe mole ratio of 1 or 0.5 are in the size range of 60–90 nm (Figure 2.5, Condition E), the peaks in the optical extinction spectra of the latter was redshifted to almost 700 nm (Figure 2.9). The PEGylated MGNPs were well dispersed and more uniform in size, compared to MGNPs before cleaning (Figure 2.10a and b). The hydrodynamic sizes of the cleansed and PEGylated particles were characterized by nanoparticle tracking analysis (NTA; Figure 2.10b, d_h = 108.6 nm) and dynamic light scattering (Figure 2.10c, d_h = 114.2 nm), both of which indicated a unimodal particle size distribution.

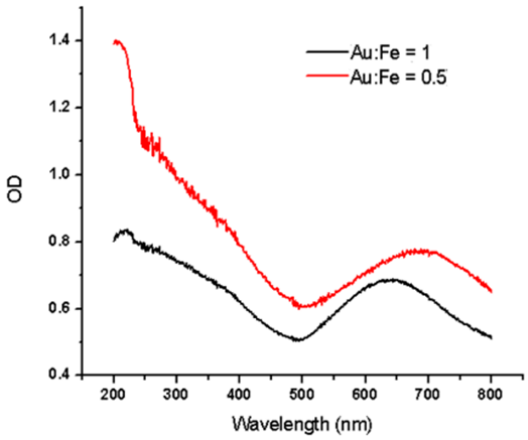

Figure 2.9. Optical extinction spectra of MGNPs generated using Au:Fe mole ratio of 1.0 (black) and 0.5 (red). MGNPs were cleansed of residual iron oxide and coated with 5-kDa PEG-SH.

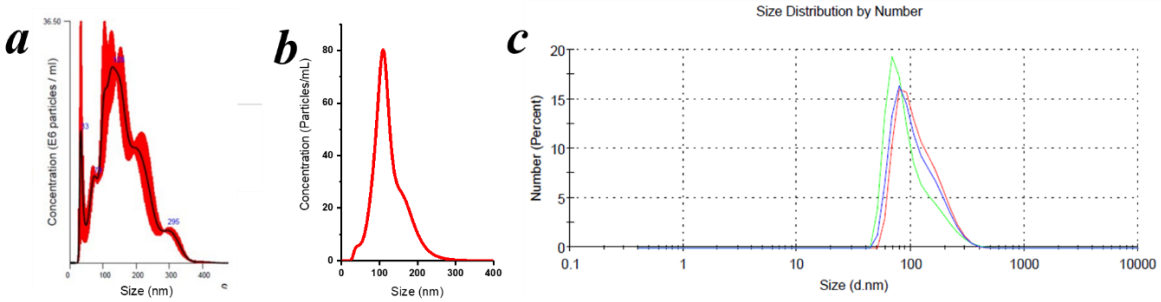

Figure 2.10. NTA size analysis of MGNCs before (a) and after (b) removing residual Fe_3O_4 and coated with PEG-SH. Hydrodynamic size: (a) mean: 156.6 ± 4.4 nm, mode: 104.4 nm, standard deviation (SD): 68.6 nm; (b) mean: 124.1 ± 1.3 nm, mode: 108.6 nm, SD: 44.1 nm. Errors in (a) and (b) represent standard error of the mean (N = 3); (c) number-based size distribution of cleaned MGNCs by dynamic light scattering (d_h = 114.2 nm).

ATR-IR spectroscopy indicates that after incorporating gold with functionalized iron oxide, the spectra peak signatures in the functionalized iron oxide were dwarfed by other IR signals (Figure 2.11a). Essentially, we saw no difference in spectra between MGNPs before and after the removal of residual surface iron oxide (Figure 2.11a). Analysis of freshly prepared MGNPs by Raman microscopy (λ_{ex} = 1064 nm) showed weak signals between 500 and 2000 cm^{-1} (Figure 2.11b, black), which we attribute to surface iron oxide. After removal of residual materials, we

observed changes below 600 cm^{-1} (Figure 2.11b, red), which could due to the adsorption of ions and molecules used during the cleansing process, namely H_3PO_4, $Na_2S_2O_3$ and EDTA. To identify the adsorbate, we first treated the MGNPs with NaCl to replace the surface molecules. As expected most of the signals were eliminated (Figure 2.11b, green). Then the same particles were treated individually with solutions of H_3PO_4, $Na_2S_2O_3$, or EDTA. The results showed that both $Na_2S_2O_3$ treated MGNPs and cleansed MGNPs share the S–S band at 450 cm^{-1} and Au–S band at 260 cm^{-1} (Figure 2.11b, red and orange).[52-53] This demonstrates clearly that $Na_2S_2O_3$ is the major species adsorbed on the MGNP surface. FT-Raman spectroscopy was also used to analyze samples after each step. After removal of residual materials, we observed that any associated peaks within the 600–1600 cm^{-1} region were eliminated (Figure 2.11c, black and red). We also saw surface-enhance Raman scattering blow 600 cm^{-1} regions (Figure 2.11c, red).

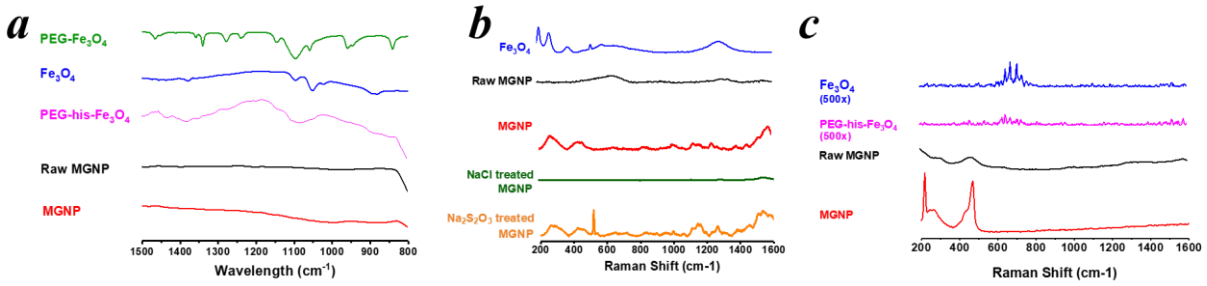

Figure 2.11. (a) ATR-IR spectra and (b) Raman spectra (λ_{ex} = 1064 nm) acquired from samples after various surface treatments; sharp peak in orange at 500 cm^{-1} from Si wafer. (c) FT-Raman spectra (λ_{ex} = 1064 nm) from samples after each step. The Raman signals intensities of Fe_3O_4 and PEG-his-Fe_3O_4 samples were amplified 500× for clarity.

Elemental analysis was performed using inductively coupled plasma mass spectrometry (ICP-MS) and EDX to determine the percentage and distribution of iron and gold within the cleansed MGNPs. The ICP-MS showed that MGNPs synthesized using an initial Au:Fe mole ratio of 4, had a final mole ratio of 18. Despite the initial Au;Fe ratio of 0.5 in the reaction mixture at 50 mL scale,

the synthesized MGNPs also have a high final mole ratio of 36 in ICP-MS analysis. We presume that much Fe tends to reside on the particle surface as iron oxide rather than being incorporated inside the formed MGNPs, and the surface residual iron oxide was lost through the cleaning process.

Compare to ICP-MS analysis, which requires a larger quantity of sample to be digested and ionized before quantification by the mass spectrometer, EDX is a non-destructive method that focuses on analyzing the specimens of interest. EDX mapping (Table 2.3) also showed MGNPs made of Au;Fe ratio of 0.5 to have much higher final mole ratio (Au:Fe = 21), meaning that most of the starting Fe_3O_4 was not incorporated into the product. EDX imaging also allowed us to evaluate the spatial distribution of iron and gold inside MGNPs. High-resolution analysis was performed on individual MGNPs using STEM in high-angle annular dark-field (HAADF) mode. As showing in the images, there is a small amount of residual iron oxide persist on the surface of MGNPs. As mentioned earlier, the residual iron oxide represents a common tradeoff between the use of GRAS chemicals for greater sustainability, and the use of stronger reagents for efficient cleaning.

It is commonly assumed that Au/iron oxide nanoparticles are formed in a nanorose structure, in which 5-nm iron oxide particles were utilized to nucleate the deposition of Au clusters.[54] However, the images indicate a nearly homogeneous distribution of iron inside the MGNPs within the resolution limits of elemental mapping (Figure 2.12). Therefore, the evidence does not support that there are nanosized (>3 nm) iron-oxide domains reside within the MGNPs. There are two possible explanations for the homogeneous distribution of iron. Firstly, the rapid growth and coalescence of Au domains trapped clusters of superparamagnetic iron oxide smaller than 3 nm, which is the resolution limit of the instrument used. Secondly, the formed AuNPs are heavily

doped with Fe(II) or Fe(III) ions or molecular iron-oxide. A previous study synthesized Au-rich Fe–Au alloy nanoparticles that showed homogeneous nucleation of gold along with iron.[55] As they decreased the initial Au:Fe mole ratio, this alloy nanoparticle had a red-shift of plasmon resonances,[55] which is consistent with our observations of MGNPs (Figure 2.9). Another group also synthesized iron-doped gold nanoparticles via laser ablation on bulk Au/Fe alloy, and they observed a complete overlap of the distribution of gold and iron.[56-58] They found the as-obtained nanoalloy not only have plasmonic properties but also are soft ferromagnetic to superparamagnetic. Similar magnetic properties were observed in iron-doped gold nanoparticles that are synthesized by reducing Au (III) and Fe (III) in aqueous solution with the assistance of surfactants.[59-60] They are relatively small in size (6–8 nm), however exhibited a small magnetic hysteresis at room temperature, which suggests superparamagnetic nanoparticles.

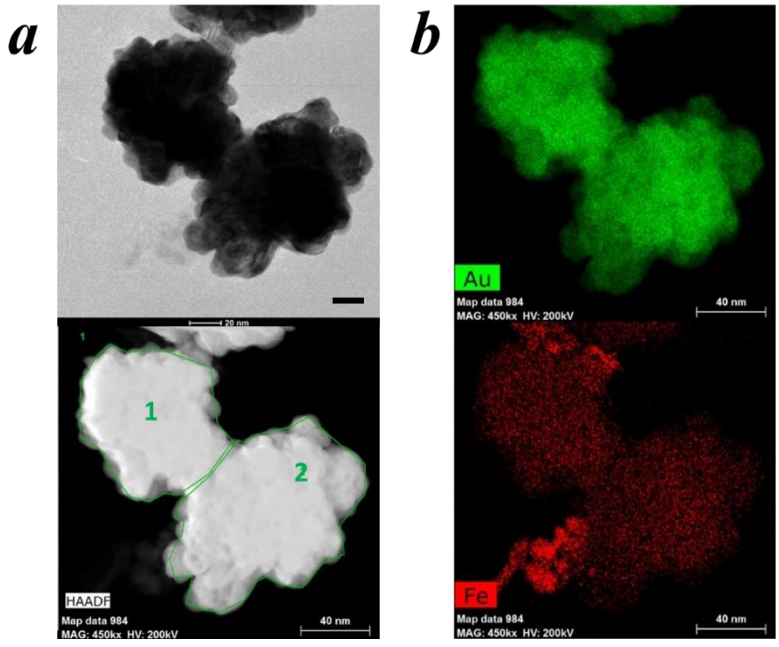

Figure 2.12. EDX data for MGNPs in HAADF-STEM mode, after cleansing. (a) TEM brightfield (top, bar = 20 nm) and HAADF-STEM (bottom, bar = 40 nm) images; (b) elemental maps for iron (top) and gold (bottom). The distribution of iron within MGNPs is nearly homogeneous.

Table 2.3 Atomic percentage of iron and gold in MGNPs (Figure 2.12a).

Atomic Percentage	Fe	Au
Area 1	4.5	95.5
Area 2	4.4	95.6

Although the Fe concentration was low, the MGNPs had sufficient moment to be collected by local field gradients produced by rare-earth magnets. The magnetic properties of MGNPs were characterized in powder form using a superconducting quantum interference device (SQUID) in vibration sample magnetometry (VSM) mode, with a field sweep of ±30 kOe. Figure 2.13 shows the magnetic data of MGNPs at room temperature. As discussed in introduction section, the observed almost closed loop with negligible coercivity (H_C) indicating the superparamagnetic nature of the MGNPs. The maximum M_S value is between 6-7 emu/g (Fig. 2.13).

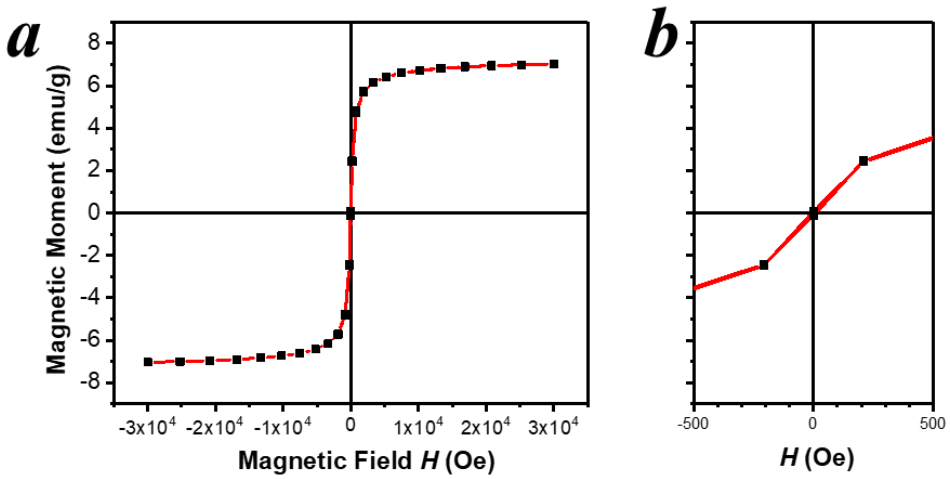

Figure 2.13. (a) Magnetization curve of MGNPs in powder form, taken at room temperature; (b) expansion of low-field region.

The magnetic properties of MGNPs were characterized in dry powder form using a physical property measurement system (PPMS) to conduct temperature-dependent dynamic magnetic measurements. Figure 2.14a shows the zero-field-cooled (ZFC) and field-cooled (FC)

magnetization curve using an applied field of 50 Oe. For the ZFC magnetization, MGNPs were first cooled to 5K in the absence of magnetic field. A magnetic field was then applied, and magnetization was measured as MGNPs were heated incrementally to 300K. The FC magnetization was measured by cooling the MGNPs to 5K in presence of field. We could not determine the blocking temperature of MGNPs within the temperature range we tested (5–300K). Whereas we noticed that the FC/ZFC curves of MGNPs are similar to those of 100-nm AuNPs (Figure 2.14b), but only 3 orders of magnitude higher. The 100-nm AuNPs were synthesized by conditioning 100 nm commercial AuNP with 5-kDa PEG and L-histidine to mediate the nucleation, followed by the growth of gold using NMH. These results suggest that iron oxide might be enhancing the ferromagnetic properties of the Au in MGNPs.

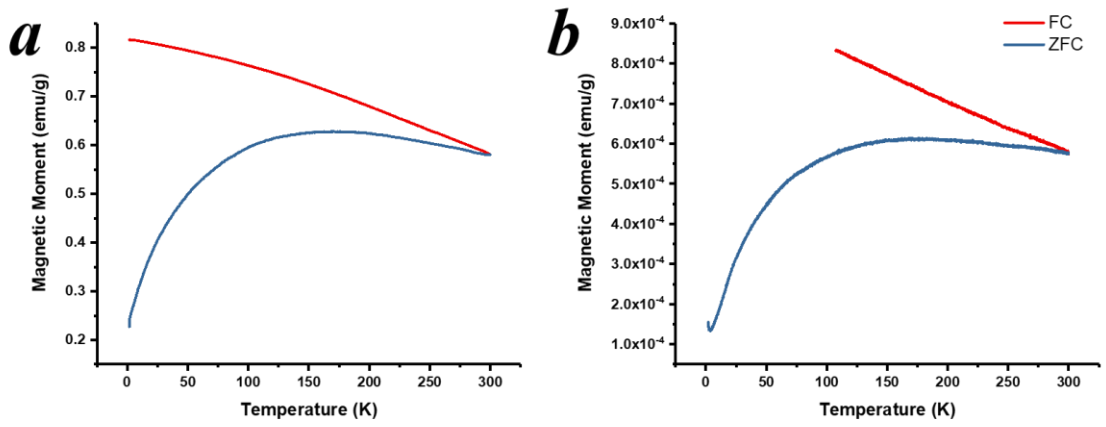

Figure 2.14. Magnetization versus temperature of (a) cleansed MGNPs and (b) AuNPs (100 nm in size) measured under zero-field-cooled (ZFC; blue) and field-cooled (FC) conditions with applied magnetic field of 50 Oe (red).

2.3 Conclusion

A highly reproducible and efficient synthesis of MGNCs can be performed at 50 mL large-scale using lower Au: Fe mole ratio, rate-controlled mechanical stirring and syringe pump. The

optimized method made it possible to make NPs with narrower and smaller size distribution of 60-90 nm and to produce sufficient quantities of materials for preclinical testing. The optimized MGNCs has strong absorption at higher NIR wavelength and has strong magnetic moment.

2.4 Materials and Methods

Materials. All reagents were purchased from Sigma-Aldrich and used as received unless otherwise stated. Deionized water was obtained from an ultrafiltration system (Milli-Q, Millipore) with a measured resistivity above 18 MΩ·cm and passed through a 0.22-μm filter to remove particulate matter.

Instrumentation. Transmission electron microscopy (TEM) images were acquired using a Tecnai T20 (FEI) operating at 200 kV with a CCD camera (Gatan US1000). TEM samples were prepared by dispensing a 25-μL drop of an aqueous MGNC dispersion onto Formvar/carbon-coated grids, followed 15 min later by blotting and drying in air for at least 30 min prior to analysis. Energy-dispersive X-ray (EDX) analysis by scanning transmission electron microscopy (STEM) was performed using a Talos F200X (FEI) equipped with a SuperX energy-dispersive spectrometer and four silicon-drift-detector units. Data was collected using a high-angle annular dark-field (HAADF) detector and recorded with a CMOS imaging camera (FEI, 4k x 4k Ceta 16 M).

Attenuated total reflectance-infrared (ATR-IR) spectroscopy was performed on powder samples deposited onto a ZnSe window, using a Nicolet Nexus 670 spectrometer (Thermo) flushed with N_2 to displace atmospheric CO_2 and moisture. Raman analysis was performed on aqueous samples, using a Nicolet 6700 FT-Raman spectrophotometer, and on solid samples, using Renishaw inVia Raman microscope.

Hydrodynamic size analysis of aqueous dispersions was performed by nanoparticle tracking analysis (NTA) using a Nanosight LM-10 (Malvern Instruments), with 405-nm laser excitation

and distilled, particle-free water stored in polyethylene containers. Three tracking videos were collected per sample with a minimum of 2000 particle tracks per run, yielding hydrodynamic size (d_h) values based on mean and mode peak analysis, with standard errors of the mean determined from triplicate experiments. Optical absorption spectra were recorded on a Cary-50 UV-Vis spectrophotometer (Varian). Dynamic light scattering (DLS) measurements were carried out using a Zetasizer Nano ZS system (Malvern) equipped with non-invasive backscatter optics and a He–Ne laser at 633 nm.

Multi-element analyses were performed using a Thermo Fisher ELEMENT 2 (ThermoFinnigan/ FinniganMAT) Inductively Coupled Argon Plasma mass spectrometer (ICP-MS) system. Samples were first dissolved in aqua regia, then diluted in 4% HCl.

Magnetic properties were measured at room temperature on neat powders using magnetic property measurement system 3 magnetometer (MPMS 3-Quantum Design) in vibrating sample magnetometer mode, with applied magnetic fields up to 10 kOe, and calibrated with colloidal γ-Fe_2O_3.[61] Dynamic magnetic measurements as a function of temperature at 50 Oe were performed on a physical property measurement system (PPMS-Quantum Design) at different temperatures.

Synthesis and modification of colloidal iron oxide. Colloidal iron oxide (Fe_3O_4) was prepared by co-precipitation, using 648 mg of $FeCl_3$ (4 mmol) and 398 mg of $FeCl_2 \cdot 4\ H_2O$ (2 mmol) dissolved in 5 ml of deaerated, deionized water. The iron salt solutions were added dropwise to 20 ml of a 28% NH_4OH solution (from freshly opened bottle) over a period of 10 min in a glass test tube, while immersed in an ultrasonic water bath. Colloidal Fe_3O_4 was formed immediately upon addition. Anaerobic conditions were maintained during the addition of iron salts to the NH_4OH solution. The reaction mixture was then removed from the ultrasonic bath and agitated for 2 min by vortex mixing to generate a homogeneous dispersion. Colloidal Fe_3O_4 was precipitated by

applying an external handheld NdFeB magnet, which produces a field gradient of 1–3 kG/cm, against the walls of the reaction tube, then redispersed in deionized water. This process was repeated three times to remove excess NH_4OH and weakly responsive colloidal materials. Final weights of magnetically active materials were obtained after drying the precipitated colloids in an oven but were otherwise used as freshly prepared dispersions at a concentration of 10 mg/mL.

To prepare PEG-stabilized Fe_3O_4, 20 mg of 5-kDa PEG was dissolved in 1 ml of deaerated, deionized water, then agitated using vortex mixing and allowed to sit at room temperature for 10 min. The freshly prepared PEG solution was then combined with 1 mL of colloidal Fe_3O_4 dispersed in water (10 mg/mL) and incubated at room temperature for 1 h. Aliquots were removed and air-dried for analytical characterization, but otherwise used as-prepared in the next step.

Synthesis of magnetic gold nanoparticles. A freshly prepared dispersion of PEG-treated Fe_3O_4 (2.5 mg in 500 μL) was added to 10 mL of an aqueous solution of L-histidine (1 mg/mL), adjusted to pH 5–6 using 0.1 M HCl, then incubated at room temperature for 1 h. Excess histidine was removed by precipitating the colloidal Fe_3O_4 using a handheld NdFeB magnet against the wall of the reaction vial, then draining the supernatant and redispersing the magnetic particles in deionized water. This process was repeated three times. In a separate container, a 109-μL aliquot of 5% w/v $HAuCl_4$ solution was diluted with 39 mL deionized water, adjusted to pH 9–10 using 5 M NaOH, then combined with the colloidal washed Fe_3O_4 solution with vortex mixing and allowed to sit for 20 min. The reaction mixture (now pH 8–9) was treated with 5 mL of 320 mM *N*-methylhydroxylamine (NMH) via syringe pump at a rate of 5 mL/h to initiate reduction, while being agitated with an overhead mechanical stirrer at 151 rpm. Noticeable color changes were observed during the process: During the initial addition of NMH, the solution changed quickly from brown to dark grey within 5 min. MGNPs were generated in significant quantities after 1 h

at room temperature, and fully formed after 12 h. The reaction gradually increased in acidity to a final range of pH 6–7.

As-formed MGNPs were separated by selective precipitation using a handheld NdFeB magnet producing linear field gradients of 1–3 kG/cm, followed 15–20 min later by decantation of supernatant containing magnetically unresponsive materials. The retentate was subjected to two more rounds of redispersion into water at twice the original volume with mild sonication, followed by magnetic precipitation, to yield MGNCs that were essentially devoid of non-magnetic gold NPs.

2.5 References

1. Gan, N.; Jin, H.; Li, T.; Zheng, L., Fe_3O_4/Au magnetic nanoparticle amplification strategies for ultrasensitive electrochemical immunoassay of alfa-fetoprotein. *International Journal of Nanomedicine* **2011,** *6*, 3259-3269.

2. Jain, T. K.; Reddy, M. K.; Morales, M. A.; Leslie-Pelecky, D. L.; Labhasetwar, V., Biodistribution, clearance, and biocompatibility of iron oxide magnetic nanoparticles in rats. *Molecular Pharmaceutics* **2008,** *5* (2), 316-327.

3. Leung, K. C.-f.; Xuan, S.; Zhu, X.; Wang, D.; Chak, C.-p.; Lee, S.-f.; Ho, W. K. w.; Chung, B. C. t., Gold and iron oxide hybrid nanocomposite materials. *Chemical Society Reviews* **2012,** *41* (5), 1911-1928.

4. Moraes Silva, S.; Tavallaie, R.; Sandiford, L.; Tilley, R. D.; Gooding, J. J., Gold coated magnetic nanoparticles: from preparation to surface modification for analytical and biomedical applications. *Chemical Communications* **2016,** *52* (48), 7528-7540.

5. Oh, N.; Park, J.-H., Surface Chemistry of Gold Nanoparticles Mediates Their Exocytosis in Macrophages. *ACS Nano* **2014,** *8* (6), 6232-6241.

6. Benetti, F.; Fedel, M.; Minati, L.; Speranza, G.; Migliaresi, C., Gold nanoparticles: role of size and surface chemistry on blood protein adsorption. *Journal of Nanoparticle Research* **2013,** *15* (6), 1-9.

7. Wei, A.; Thomas, M.; Mehtala, J.; Wang, J., Gold nanoparticles (GNPs) as multifunctional materials for cancer treatment. *Biomaterials for Cancer Therapeutics,* Woodhead Pub: **2013;** 349-386.

8. Tong, L.; Wei, Q.; Wei, A.; Cheng, J.-X., Gold Nanorods as Contrast Agents for Biological Imaging: Optical Properties, Surface Conjugation and Photothermal Effects. *Other Nanotechnology Publications* **2009,** *85*, 21-32.

9. Zanganeh, S.; Hutter, G.; Spitler, R.; Lenkov, O.; Mahmoudi, M.; Shaw, A.; Pajarinen, J. S.; Nejadnik, H.; Goodman, S.; Moseley, M.; Coussens, L. M.; Daldrup-Link, H. E., Iron oxide nanoparticles inhibit tumour growth by inducing pro-inflammatory macrophage polarization in tumour tissues. *Nature Nanotechnology* **2016,** *11* (11), 986-994.

10. Veiseh, O.; Gunn, J. W.; Zhang, M., Design and fabrication of magnetic nanoparticles for targeted drug delivery and imaging. *Advanced Drug Delivery Reviews* **2010,** *62* (3), 284-304.

11. Yoo, D.; Lee, J.-H.; Shin, T.-H.; Cheon, J., Theranostic magnetic nanoparticles.(Theranostic Nanomedicine)(Report). *Accounts of Chemical Research* **2011,** *44* (10), 863-874.

12. Silva, A. S.-F., É.; Carvalho, J.; Pontes, T.; Araújo-Neto, R.; Silva, K.; Carriço, A.; Egito, E., Magnetic Particles in Biotechnology: From Drug Targeting to Tissue Engineering. *Advances in Applied Biotechnology,* InTech, **2012;** *13*.

13. Park, J.; Kadasala, N. R.; Abouelmagd, S. A.; Castanares, M. A.; Collins, D. S.; Wei, A.; Yeo, Y., Polymer–iron oxide composite nanoparticles for EPR-independent drug delivery. *Biomaterials* **2016,** *101*, 285-295.

14. Teja, A. S.; Koh, P.-Y., Synthesis, properties, and applications of magnetic iron oxide nanoparticles. *Progress in Crystal Growth and Characterization of Materials* **2009,** *55* (1), 22-45.

15. Chikazumi, S., Physics of Ferromagnetism. 2nd ed.; *OUP Oxford*: **2009;** 3-49.

16. Tanwar, S.; Awana, V.; Singh, S.; Pasricha, R., Magnetic field dependence of blocking temperature in oleic acid functionalized iron oxide nanoparticles. *Journal of Superconductivity and Novel Magnetism* **2012,** *25* (6), 2041-2045.

17. Mahmoudi, M.; Sant, S.; Wang, B.; Laurent, S.; Sen, T., Superparamagnetic iron oxide nanoparticles (SPIONs): Development, surface modification and applications in chemotherapy. *Advanced Drug Delivery Reviews* **2011,** *63* (1), 24-46.

18. Zhai, Y.; Zhai, J.; Wang, Y.; Guo, S.; Ren, W.; Dong, S., Fabrication of iron oxide core/gold shell submicrometer spheres with nanoscale surface roughness for efficient surface-enhanced Raman scattering. *The Journal of Physical Chemistry C* **2009,** *113* (17), 7009-7014.

19. Zhou, X.; Xu, W.; Wang, Y.; Kuang, Q.; Shi, Y.; Zhong, L.; Zhang, Q., Fabrication of cluster/shell Fe_3O_4/Au nanoparticles and application in protein detection via a SERS method. *The Journal of Physical Chemistry C* **2010,** *114* (46), 19607-19613.

20. Hu, Y.; Sun, Y., Stable magnetic hot spots for simultaneous concentration and ultrasensitive surface-enhanced Raman scattering detection of solution analytes. *The Journal of Physical Chemistry C* **2012,** *116* (24), 13329-13335.

21. Baniukevic, J.; Hakki Boyaci, I.; Goktug Bozkurt, A.; Tamer, U.; Ramanavicius, A.; Ramanaviciene, A., Magnetic gold nanoparticles in SERS-based sandwich immunoassay for antigen detection by well oriented antibodies. *Biosensors and Bioelectronics* **2013,** *43* (1), 281-288.

22. Kadasala, N. R.; Wei, A., Trace detection of tetrabromobisphenol A by SERS with DMAP-modified magnetic gold nanoclusters. *Nanoscale* **2015,** *7* (25), 10931-10935.

23. Wei, Q.; Song, H.-M.; Leonov, A. P.; Hale, J. A.; Oh, D.; Ong, Q. K.; Ritchie, K.; Wei, A., Gyromagnetic imaging: dynamic optical contrast using gold nanostars with magnetic cores. *Journal of the American Chemical Society* **2009,** *131* (28), 9728-9734.

24. Song, H.-M.; Wei, Q.; Ong, Q. K.; Wei, A., Plasmon-resonant nanoparticles and nanostars with magnetic cores: synthesis and magnetomotive imaging. *ACS Nano* **2010,** *4* (9), 5163-5173.

25. Wei, Q.; Wei, A., Optical imaging with dynamic contrast agents. *Chemistry a European Journal* **2011,** *17* (4), 1080-1091.

26. Kadasala, N. R.; Saei, M.; Cheng, G. J.; Wei, A., Dry etching with nanoparticles: formation of high aspect-ratio pores and channels using magnetic gold nanoclusters. *Advanced Materials* **2018,** *30* (3), 1703091.

27. Kadasala, N. R.; Lin, L.; Gilpin, C.; Wei, A., Eco-friendly (green) synthesis of magnetically active gold nanoclusters. *Science and Technology of Advanced Materials* **2017,** *18* (1), 210-218.

28. Hogarth, G., Metal-dithiocarbamate complexes: chemistry and biological activity. *Mini-Reviews in Medicinal Chemistry* **2012,** *12* (12), 1202-1215.

29. Wang, J.; Thomas, M.; Lin, P.; Cheng, J.-X.; Matei, D. E.; Wei, A., siRNA delivery using dithiocarbamate-anchored oligonucleotides on gold nanorods. *Bioconjugate Chemistry* **2018,** *30* (2), 443-453.

30. Thompson, R. W.; Valentine, H. L.; Valentine, W. M., In *vivo* and in *vitro* hepatotoxicity and glutathione interactions of *N* -methyldithiocarbamate and *N,N* -dimethyldithiocarbamate in the rat. *Toxicological Sciences* **2002,** *70* (2), 269-280.

31. Mulvihill, M. J.; Beach, E. S.; Zimmerman, J. B.; Anastas, P. T., Green chemistry and green engineering: a framework for sustainable technology development. *Annual Review of Environment and Resources* **2011,** *36* (1), 271-293.

32. Chen, M.; Yamamuro, S.; Farrell, D.; Majetich, S. A., Gold-coated iron nanoparticles for biomedical applications. *Journal of Applied Physics* **2003,** *93* (10), 7551-7553.

33. Lyon, J. L.; Fleming, D. A.; Stone, M. B.; Schiffer, P.; Williams, M. E., Synthesis of Fe oxide Core/Au shell nanoparticles by iterative hydroxylamine seeding. *Nano Letters* **2004,** *4* (4), 719-723.

34. Wang, L.; Luo, J.; Fan, Q.; Suzuki, M.; Suzuki, I. S.; Engelhard, M. H.; Lin, Y.; Kim, N.; Wang, J. Q.; Zhong, C.-J., Monodispersed core-shell Fe_3O_4@Au nanoparticles. *The Journal of Physical Chemistry B* **2005,** *109* (46), 21593-21601.

35. Mandal, M.; Kundu, S.; Ghosh, S. K.; Panigrahi, S.; Sau, T. K.; Yusuf, S. M.; Pal, T., Magnetite nanoparticles with tunable gold or silver shell. *Journal of Colloid and Interface Science* **2005,** *286* (1), 187-194.

36. Wang, L.; Bai, J.; Li, Y.; Huang, Y., Multifunctional Nanoparticles Displaying Magnetization and Near- IR Absorption. *Angewandte Chemie International Edition* **2008,** *47* (13), 2439-2442.

37. Guo, S.; Dong, S.; Wang, E., A general route to construct diverse multifunctional Fe_3O_4/metal hybrid nanostructures. *Chemistry a European Journal* **2009,** *15* (10), 2416-2424.

38. Huang, W. C.; Tsai, P. J.; Chen, Y. C., Multifunctional Fe_3O_4@Au nanoeggs as photothermal agents for selective killing of nosocomial and antibiotic- resistant bacteria. *Small* **2009,** *5* (1), 51-56.

39. Pal, S.; Morales, M.; Mukherjee, P.; Srikanth, H., Synthesis and magnetic properties of gold coated iron oxide nanoparticles. *Journal of Applied Physics* **2009,** *105* (7), 07B504.

40. Xie, H.-Y.; Zhen, R.; Wang, B.; Feng, Y.-J.; Chen, P.; Hao, J., Fe_3O_4/Au Core/Shell nanoparticles modified with Ni_2^+−Nitrilotriacetic acid specific to histidine-tagged proteins. *The Journal of Physical Chemistry* **2010,** *114* (11), 4825-4830.

41. Zhang, Q.; Ge, J.; Goebl, J.; Hu, Y.; Sun, Y.; Yin, Y., Tailored synthesis of superparamagnetic gold nanoshells with tunable optical properties. *Advanced Materials* **2010,** *22* (17), 1905-1909.

42. Ma, L. L.; Tam, J. O.; Willsey, B. W.; Rigdon, D.; Ramesh, R.; Sokolov, K.; Johnston, K. P., Selective targeting of antibody conjugated multifunctional nanoclusters (nanoroses) to epidermal growth factor receptors in cancer cells. *Langmuir* **2011,** *27* (12), 7681-7690.

43. Jin, X.; Liang, J.; Yang, C.; Hao, R.; Zhuang, J.; Yang, W., Facile deposition of continuous gold shells on Tween-20 modified Fe_3O_4 superparticles. *Journal of Materials Chemistry B* **2013,** *1* (14), 1921-1925.

44. Jin, Y.; Jia, C.; Huang, S.-W.; O'Donnell, M.; Gao, X., Multifunctional nanoparticles as coupled contrast agents. *Nature Communications* **2010,** *1* (4), 41-48.

45. Massart, R., Preparation of aqueous magnetic liquids in alkaline and acidic media. *IEEE Transactions on Magnetics* **1981,** *17* (2), 1247-1248.

46. Chiarizia, R.; Horwitz, E. P., New formulations for iron oxides dissolution. *Hydrometallurgy* **1991,** *27* (3), 339-360.

47. Zhu, H.; Coleman, D. M.; Dehen, C. J.; Geisler, I. M.; Zemlyanov, D.; Chmielewski, J.; Simpson, G. J.; Wei, A., Assembly of dithiocarbamate-anchored monolayers on gold surfaces in aqueous solutions. *Langmuir* **2008,** *24* (16), 8660-8666.

48. Zhang, Y.; Kallay, N.; Matijevic, E., Interaction of metal hydrous oxides with chelating agents. 7. Hematite-oxalic acid and -citric acid systems. *Langmuir* **1985,** *1* (2), 201-206.

49. Olvera-Venegas, P. N.; Hernández Cruz, L. E.; Lapidus, G. T., Leaching of iron oxides from kaolin: Synergistic effect of citrate-thiosulfate and kinetic analysis. *Hydrometallurgy* **2017,** *171*, 16-26.

50. Feng, D.; van Deventer, J. S. J., Thiosulphate leaching of gold in the presence of orthophosphate and polyphosphate. *Hydrometallurgy* **2011,** *106* (1), 38-45.

51. Sidhu, P.; Gilkes, R.; Cornell, R.; Posner, A.; Quirk, J., Dissolution of iron oxides and oxyhydroxides in hydrochloric and perchloric acids. *Clays and Clay Minerals* **1981,** *29* (4), 269-276.

52. Chen, D.-J.; Xu, B.; Sun, S.-G.; Tong, Y. J., Electroless deposition of ultrathin Au film for surface enhanced in situ spectroelectrochemisrty and reaction-driven surface reconstruction for oxygen reduction reaction. *Catalysis today* **2012,** *182* (1), 46-53.

53. Woods, R.; Hope, G. A.; Watling, K. M.; Jeffrey, M. I., A Spectroelectrochemical Study of Surface Species Formed in the Gold/Thiosulfate System. *Journal of The Electrochemical Society* **2006,** *153* (7), D105.

54. Ma, L. L.; Feldman, M. D.; Tam, J. M.; Paranjape, A. S.; Cheruku, K. K.; Larson, T. A.; Tam, J. O.; Ingram, D. R.; Paramita, V.; Villard, J. W.; Jenkins, J. T.; Wang, T.; Clarke, G. D.; Asmis, R.; Sokolov, K.; Chandrasekar, B.; Milner, T. E.; Johnston, K. P., Small multifunctional nanoclusters (nanoroses) for targeted cellular imaging and therapy. *ACS Nano* **2009,** *3* (9), 2686-2696.

55. Dahal, N.; Chikan, V.; Jasinski, J.; Leppert, V. J., Synthesis of water-soluble iron−gold alloy nanoparticles. *Chemistry of Materials* **2008,** *20* (20), 6389-6395.

56. Amendola, V.; Meneghetti, M.; Bakr, O. M.; Riello, P.; Polizzi, S.; Anjum, D. H.; Fiameni, S.; Arosio, P.; Orlando, T.; De Julian Fernandez, C.; Pineider, F.; Sangregorio, C.; Lascialfari, A., Coexistence of plasmonic and magnetic properties in Au 89 Fe 11 nanoalloys. *Nanoscale* **2013,** *5* (12), 5611-5619.

57. Amendola, V.; Saija, R.; Marag, O. M.; Iat, M. A., Superior plasmon absorption in iron-doped gold nanoparticles. *Nanoscale* **2015,** *7* (19), 8782-8792.

58. Amendola, V.; Scaramuzza, S.; Agnoli, S.; Polizzi, S.; Meneghetti, M., Strong dependence of surface plasmon resonance and surface enhanced Raman scattering on the composition of AuFe nanoalloys. *Nanoscale* **2014,** *6* (3), 1423-1433.

59. Wijaya, A.; Brown, K. A.; Alper, J. D.; Hamad-Schifferli, K., Magnetic field heating study of Fe-doped Au nanoparticles. *Journal of Magnetism and Magnetic Materials* **2007,** *309* (1), 15-19.

60. Liu, H.; Hou, P.; Zhang, W.; Kim, Y. K.; Wu, J., The synthesis and characterization of polymer-coated feau multifunctional nanoparticles. *Nanotechnology* **2010,** *21* (33), 335602-335611.

61. Batis-Landoulsi, H.; Vergnon, P., Magnetic moment of γ-Fe 2 O 3 microcrystals: morphological and size effect. *Journal of Materials Science* **1983,** *18* (11), 3399-3403.

VITA

Lu Lin was born in Yueyang, China in 1991, where she grew up and finished the first year of middle school. In 2004, she moved with her parents to Hangzhou, China where completed her middle school and high school education. From there she attended Anhui Normal University and graduated with a B.S. degree in biotechnology in 2012. She then pursued her M.S degree with a human nutrition major at Columbia University in the City of New York. After she graduated in 2013, she worked as a laboratory technician under the supervision of Nataki C. Douglas in Columbia University Medical Center. In fall 2014, she left New York and entered Purdue University Interdisciplinary Life Science program to pursue a doctorate. Following a one-year rotation period, she joined Professor Alexander Wei's research group. She completed her Ph.D. degree in July 2019.

PUBLICATIONS

ACS Infectious Diseases

Article

Cite This: ACS Infect. Dis. 2018, 4, 1564−1573

pubs.acs.org/journal/aidcbc

Rapid Uptake and Photodynamic Inactivation of Staphylococci by Ga(III)-Protoporphyrin IX

Ana V. Morales-de-Echegaray,[†] Thora R. Maltais,[†] Lu Lin,[†] Waleed Younis,[‡] Naveen R. Kadasala,[†] Mohamed N. Seleem,[‡] and Alexander Wei*[,†]

[†]Department of Chemistry and [‡]Department of Comparative Pathobiology, Purdue University, West Lafayette, Indiana 47907, United States

Supporting Information

ABSTRACT: Antimicrobial photodynamic therapy (aPDT) is a promising method for the topical treatment of drug-resistant staphylococcal infections and can be further improved by identifying mechanisms that increase the specificity of photosensitizer uptake by bacteria. Here we show that Ga(III)-protoporphyrin IX chloride (Ga-PpIX), a fluorescent hemin analog with previously undisclosed photosensitizing properties, can be taken up within seconds by *Staphylococcus aureus* including multidrug-resistant strains such as MRSA. The uptake of Ga-PpIX by staphylococci is likely diffusion-limited and is attributed to the expression of high-affinity cell-surface hemin receptors (CSHRs), namely iron-regulated surface determinant (Isd) proteins. A structure−activity study reveals the ionic character of both the heme center and propionyl groups to be important for uptake specificity. Ga-PpIX was evaluated as a photosensitizer against *S. aureus* and several clinical isolates of MRSA using a visible light source, with antimicrobial activity at 0.03 μM with 10 s of irradiation by a 405 nm diode array (1.4 J/cm^2); antimicrobial activity could also be achieved within minutes using a compact fluorescent lightbulb. GaPpIX was not only many times more potent than PpIX, a standard photosensitizer featured in clinical aPDI, but also demonstrated low cytotoxicity against HEK293 cells and human keratinocytes. Ga-PpIX uptake was screened against a diverse panel of bacterial pathogens using a fluorescence-based imaging assay, which revealed rapid uptake by several Gram-positive species known to express CSHRs, suggesting future candidates for targeted aPDT.

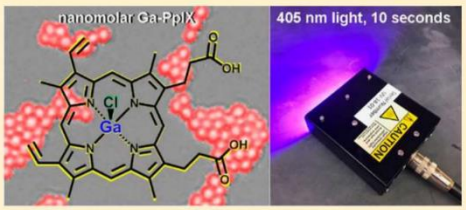

KEYWORDS: *staphylococci, MRSA, photodynamic therapy, hemin, porphyrins, targeted delivery*

Staphylococcus aureus and its multidrug-resistant (MDR) strains remain the leading cause of hospital-associated infections, despite attempts to address this problem over the last several decades.[1−3] Vancomycin, the current gold standard for combating methicillin-resistant *S. aureus* (MRSA), is compromised by the rise of vancomycin-resistant strains, and while newer drugs such as linezolid and daptomycin have been recommended as alternatives,[4] MRSA strains with demonstrated resistance against these have already emerged.[5,6] In fact, the speed with which *S. aureus* and other pathogens can develop or acquire antibiotic resistance threatens to jeopardize any therapy that relies on conventional drug paradigms.[7]

A possible exception to this argument is antimicrobial photodynamic therapy (aPDT), in which a photosensitizer is delivered to microbial pathogens for generating singlet oxygen and other reactive oxygen species (ROS) upon irradiation with light.[8,9] aPDT cannot be easily overcome by established mechanisms of antibiotic resistance[10] and has been found to be particularly effective against Gram-positive MDR bacteria such as MRSA.[11] aPDT can be applied in situations that are not limited by light penetration into tissue, and has been found to be compatible with keratinocytes;[12] established clinical aPDT examples include the topical treatment of acne[13,14] and the decolonization of bacteria in oral cavities (periodontal disease).[15,16] Ongoing clinical trials and *in vivo* studies indicate that aPDT should also be effective for disinfection of open wounds,[17−19] and decolonization of exposed skin prior to surgery to mitigate postoperative infections.[20]

Topically administered aPDT holds great promise to reduce or prevent MRSA infections, but the efficient delivery and selective uptake of photosensitizers should also be considered.[17,18] For example, many photosensitizers are cationic or hydrophobic in nature, resulting in their indiscriminate uptake into mammalian cells as well as bacteria. This not only contributes toward collateral cytotoxicity, but also reduces the amount of available photosensitizer for aPDT. Such issues are being addressed by developing photosensitizer conjugates for their targeted delivery to bacteria.[21] Molecular uptake pathways associated with bacterial virulence are especially attractive in this regard, although incorporation of a targeting ligand may result in added complexity.

Hemin acquisition systems offer natural portals for the bacterial uptake of photosensitizers and obviate the need to

Received: May 19, 2018
Published: September 3, 2018

DOI: 10.1021/acsinfecdis.8b00125
ACS Infect. Dis. 2018, 4, 1564−1573

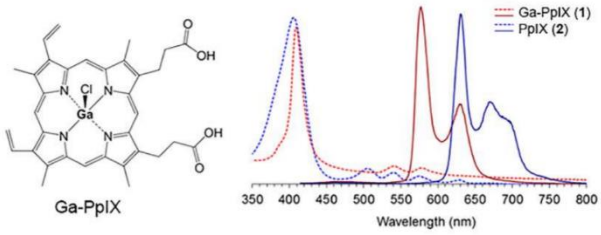

Figure 1. Absorbance (---) and emission (—) spectra for Ga-PpIX (8 μM in DMSO, red) with comparison to PpIX (blue). Structure of Ga-PpIX shown at left.

design synthetic conjugates. Although hemin itself (Fe(III)-protoporphyrin IX chloride, or Fe-PpIX) does not have photosensitizing properties, deferrated species such as PpIX and hematoporphyrin (HP) are highly photoactive and have been widely used in aPDT.[22,23] Non-iron metalloporphyrins are also good candidates for uptake by hemin acquisition systems, many of which are chemically more robust than their unmetalated forms.[24−27] Seminal work by Stojiljkovic has shown that non-iron PpIX species are readily taken up by bacterial hemin uptake pathways and also exhibit low collateral toxicity in human cell lines and in rodent models.[28] Non-iron PpIX species have been investigated as antimicrobial agents,[28−31] but remarkably their utility for aPDT remains to be explored,[32] despite the long history of porphyrin-based photosensitizers in photodynamic therapies.

In this work, we show that Ga(III)-protoporphyrin IX chloride (Ga-PpIX), a fluorescent analog of hemin, exerts an antimicrobial effect against *S. aureus* and several clinical isolates of MRSA at nanomolar concentrations, following a 10-s exposure to a visible light source array operating at 405 nm. The uptake of Ga-PpIX by *S. aureus* is faster than our ability to measure experimentally and appears to be diffusion-controlled. The primary mechanism of Ga-PpIX uptake involves cell-surface hemin receptors (CSHRs), most likely the iron-regulated surface determinant (Isd) proteins in the case of *S. aureus*,[33,34] which can be exploited for targeted delivery. Structure−uptake studies using various PpIX derivatives reveal important features for rapid and specific uptake by this pathway. We also show that Ga-PpIX is superior in potency to several other photosensitizers, yet has low dark cytotoxicity to human kidney cells and keratinocytes, as well as negligible phototoxicity to the latter under aPDT conditions. Lastly, we establish the importance of CSHRs for targeted Ga-PpIX uptake by screening a wider panel of Gram-positive and -negative bacteria having diverse hemin acquisition systems, and we identify several other pathogens as candidates for rapid aPDT.

■ RESULTS AND DISCUSSION

Photophysical Properties of Ga-PpIX. Absorption spectroscopy of PpIX (prepared by deferration of hemin chloride with iron powder) and Ga-PpIX (prepared by microwave heating with anhydrous $GaCl_3$) reveals a distinct change in the Q bands (475−650 nm) characteristic of metal substitution but a modest narrowing of the Soret band at 405 nm (Figure 1).[26] Fluorescence spectroscopy reveals a blueshift in the emission band of Ga-PpIX of over 80 nm, with a primary emission band at 575 nm and secondary emission at 628 nm. The fluorescence quantum yield of Ga-PpIX at 405 nm is 6.3%, which is sufficient for quantitative image analysis of bacterial labeling or uptake. The singlet-oxygen quantum yield (ϕ_Δ) of Ga-PpIX is estimated by the electron paramagnetic resonance (EPR)-based method, described by Nakamura et al.,[35] using a 405 nm light-emitting diode (LED) array for excitation and tetrakis(1-methyl-4-pyridinio)porphyrin (TMPyP) as a reference compound (ϕ_Δ in water: 77%).[36] Standard curves of EPR signal intensities yield a ϕ_Δ of 45% (Figure S2, Supporting Information).

Bacterial Uptake of Ga-PpIX. In a previous study on the bacterial recognition of hemin, we found *S. aureus* to be especially avid in its binding of hemin conjugates with observable adhesion on the order of minutes, leading us to postulate the role of high-affinity CSHRs (specifically Isd proteins) in rapid hemin uptake.[37] Isd expression is well-known to be activated by the ferric uptake regulator (*fur*) gene and increases upon iron deprivation.[33,38] This leads us to compare Ga-PpIX uptake by *S. aureus* cultured in standard and iron-limited conditions, with modest levels observed by the former but dramatically higher uptake by the latter, corresponding with greater avidity (Figure S4, Supporting Information). Iron-deficient conditions are relevant from a clinical perspective, as the body withdraws all available sources of iron during infection, inducing pathogens to express various iron acquisition systems including CSHRs.

In this study, Ga-PpIX was deployed as a fluorescent hemin analog to characterize its rate of uptake by *S. aureus* using flow cytometry. Suspensions of *S. aureus* (PC 1203) cultured in iron-deficient media were rapidly mixed with Ga-PpIX in phosphate buffered saline (PBS), incubated at room temperature for fixed intervals between 10 s and 40 min, and then fixed with 4% paraformaldehyde and subjected to flow cytometry. Remarkably, only minor variations in fluorescence were observed, regardless of exposure times to Ga-PpIX (Figure 2). The absence of a fluorescence buildup period over time implies that the capture of Ga-PpIX by CSHRs is likely diffusion-controlled.

While the rapid bacterial uptake of Ga-PpIX is of primary interest, we considered whether Ga-PpIX accumulation might be affected adversely by the activation of bacterial efflux pumps, a known mechanism for removing excessive hemin to prevent acute iron toxicity.[39] In this study, we did not obtain conclusive evidence of Ga-PpIX-activated efflux, relative to the time scale of photodynamic inactivation (see below). Given our observation of rapid Ga-PpIX uptake, we reasoned that maximum aPDT efficacy could be achieved by applying light irradiation immediately after introducing Ga-PpIX, and would also circumvent hemin efflux as a potential resistance mechanism.

DOI: 10.1021/acsinfecdis.8b00125
ACS Infect. Dis. 2018, 4, 1564−1573

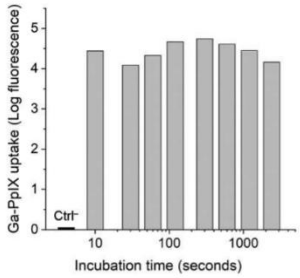

Figure 2. Flow cytometry of *S. aureus* treated with Ga-PpIX as a function of incubation time (plotted on log scale; Ctrl⁻ = no Ga-PpIX). Bacteria were fixed with paraformaldehyde prior to analysis. All runs based on gated bacteria populations and reported as mean fluorescence values.

To elucidate the most relevant structural features for Ga-PpIX uptake by *S. aureus*, we performed a competitive uptake assay using one equivalent of hemin against Ga-PpIX (**1**), PpIX (**2**), and 11 other fluorescent porphyrin derivatives, with evaluation by fluorescence imaging after 15 min of coincubation (Figure 3 and Table S1, Supporting Information). These studies were guided in part by insights taken from the X-ray structures of hemin and Ga-PpIX within the binding pocket of IsdH:[40] (i) apical coordination of the trivalent metal center by a tyrosine residue; (ii) flanking of the vinyl groups on pyrrole rings A and B by nearby aromatic residues; and (iii) the extension and presumed hydration of the propionyl groups (rings C and D) outside of the binding pocket.

The competitive uptake assay produced three important observations: (i) the uptake of Ga(III)-PpIX (**1**) was strongly affected by competition with hemin chloride, with greater than 80% reduction in fluorescence versus the positive control without hemin; (ii) the uptakes of diacids PpIX (**2**), Zn(II)-PpIX (**3**), HP (**4**), and Zn(II)-HP (**5**) were moderately affected by hemin; and (iii) uptakes of dimethyl diesters **6**–**8** (derived from **1**, **2**, and **4**), tetraesters **9** and **10** (di-*O*-acetyl and -succinyl derivatives of **8**), diacetyldeuteroporphyrins

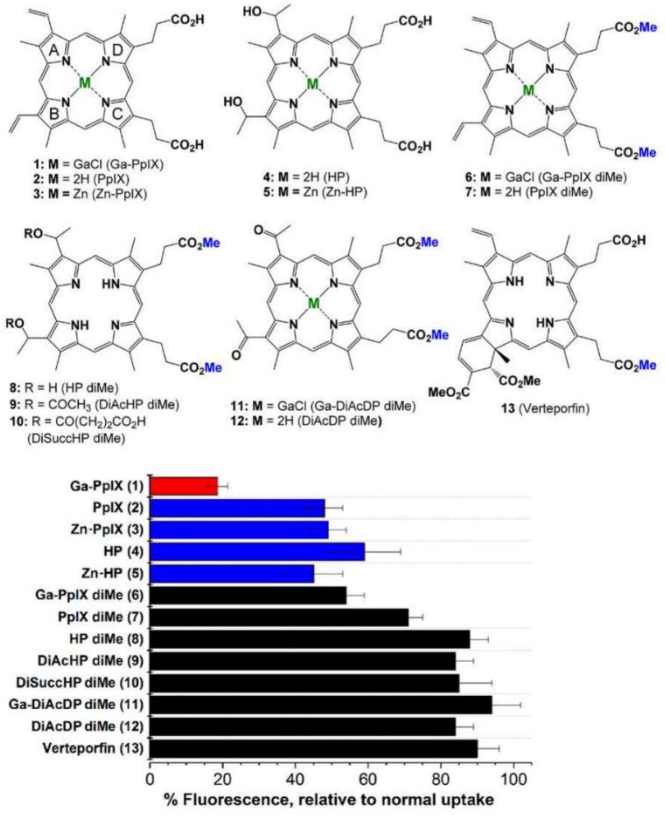

Figure 3. Competitive uptake of PpIX derivatives **1**–**13** by *S. aureus* (PCI 1203) versus one equivalent of hemin (15 min coexposure). Ga-PpIX **1** uptake inhibition (red) is greater than that of other PpIX diacid and diester derivatives (blue and black, respectively). All values are relative to uptake in the absence of hemin; see Supporting Information for complete details.

DOI: 10.1021/acsinfecdis.8b00125
ACS Infect. Dis. 2018, 4, 1564–1573

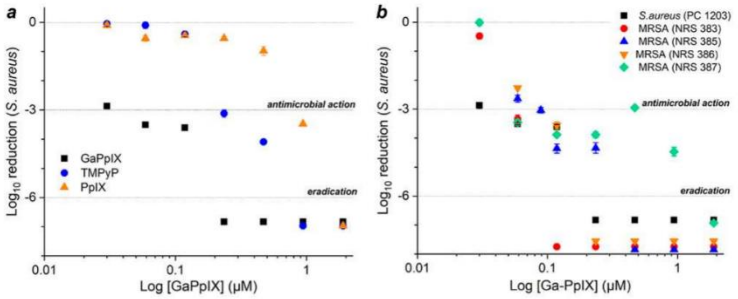

Figure 4. (a) Antimicrobial photodynamic inactivation of *S. aureus* (PC 1203, ATCC 10537) using Ga-PpIX in PBS (pH 7.4), with 10-s exposure to 405 nm light from a LED array (1.4 J/cm^2). aPDI activities of two other photosensitizers (TMPyP and PpIX) were evaluated under identical conditions for comparison. (b) aPDI activity of Ga-PpIX against several clinical isolates of MRSA. Bacteria were plated after irradiation and incubated at 37 °C for 20 h to obtain log reduction values; antimicrobial action and eradication correspond to 3- and 6-log reductions in CFU/mL, respectively. All experiments were performed in triplicate.

(DiAcDP) **11** and **12**, and verteporfin **13** were all less affected by hemin relative to their diacid counterparts, indicating nonspecific uptake as a major or dominant mechanism.

The competitive uptake of **1** (in red) versus compounds **2**–**5** (in blue) suggests that the CSHRs on *S. aureus* have stronger affinity for ionic heme groups (with trivalent metal ions) and weaker affinity for neutral ones, with nonspecific uptake pathways gaining significance in the latter case. Replacement of carboxylic acids with nonionizable esters (compounds **6**–**13**) resulted in further loss of selective uptake, to the extent that CSHR expression no longer played a major role. These observations were confirmed by control experiments using *S. aureus* cultured in standard (iron-replete) media, with a large decrease in the uptake efficiency of **1** and a moderate decrease in the case of **2**, but with little or no effect for several diester derivatives, indicating uptake of the latter to be independent of CSHR activity (Figure S5 and Table S2, Supporting Information). We therefore conclude that the ionic character of the heme group is important for selective uptake by CSHRs and that esterification of the propionyl groups increases lipophilicity and contributes toward loss of specificity.

Antimicrobial Photodynamic Inactivation (aPDI). Ga-PpIX was initially evaluated as a photosensitizer against a laboratory strain of *S. aureus* (PC 1203). Studies were performed in the context of topical administration using a hand-held LED array operating at 405 nm (30 mW/cm^2 per LED), a visible wavelength with no risk of DNA damage. Antimicrobial photodynamic inactivation (aPDI) experiments were performed on bacterial suspensions in 96-well plates; wells were treated with aliquots of Ga-PpIX, followed immediately by a 10-s exposure to 405 nm light using the LED source (140 mW/cm^2; see Experimental Section for complete details). The aPDI activity of Ga-PpIX against *S. aureus* is remarkably rapid and potent, with 10 s of irradiation (ca. 1.4 J/cm^2) resulting in a 2.87 ± 0.12 log reduction in colony-forming units (CFU) per mL at 0.03 μM, and complete eradication (>6 log reduction in CFU/mL) at 0.24 μM (Figure 4a). Light exposure for 30 s did not produce a clear increase in potency for aPDI, although eradication was observed at a lower Ga-PpIX dose (Table 1). In contrast, Ga-PpIX exhibited only modest bactericidal activity in the absence of light, with a 3-log reduction at approximately 70 μM. The photodynamic effect

Table 1. aPDI Activity of Ga-PpIX against Various *S. aureus* Strains

light exposure (in seconds)[a]	antimicrobial activity (3-log reduction)		eradication (>6-log reduction)
	conc. (μM)	aPDI potency[b]	conc. (μM)
S. aureus (PCI 1203; ATCC 10537)			
0 s (dark)	70		
10 s	0.03[c]	2400	0.24
30 s	<0.06[d]		0.12
MRSA (USA200), Clinical Isolate NRS 383			
0 s (dark)	36.3		
10 s	0.06	600	0.12
30 s	<0.06[d]		<0.06[d]
MRSA (USA500), Clinical Isolate NRS 385			
0 s (dark)	>145[e]		
10 s	0.09	>1600	0.47
30 s	<0.06[d]		<0.06[d]
MRSA (USA700), Clinical Isolate NRS 386			
0 s (dark)	>145[e]		
10 s	0.12	>1200	0.24
30 s	0.06	>2400	0.24
MRSA (USA800), Clinical Isolate NRS 387			
0 s (dark)	72.6		
10 s	0.06	1200	1.88
30 s	0.06		>0.24[f]

[a]Irradiated with 405 nm LED array (140 mW/cm^2 per well), with 10- and 30-s exposure times corresponding to 1.4 and 4.2 J/cm^2, respectively. [b]Fold reduction in Ga-PpIX concentration, relative to dark toxicity (no light exposure). [c]3-log reduction within 1σ of experimental value. [d]Lowest concentration tested at this fluence; > 3-log CFU/mL reduction. [e]Highest concentration tested; < 3-log CFU/mL reduction. [f]Highest concentration tested; < 6-log CFU/mL reduction.

thus increased the potency of Ga-PpIX against *S. aureus* by over three orders of magnitude relative to its dark toxicity.

The aPDI activity of Ga-PpIX was compared against two other photosensitizers with similar λ_{max} values, under identical conditions: TMPyP (λ_{max} 421 nm), a tetracationic porphyrin that has also been noted for its rapid and potent aPDI,[41,42] and PpIX (λ_{max} 405 nm), the photoactive species generated in situ during clinical aPDT with 5-aminolevulinic acid.[13,14] aPDI

DOI: 10.1021/acsinfecdis.8b00125
ACS Infect. Dis. 2018, 4, 1564–1573

studies using the 405 nm LED source show both photosensitizers to be active at this wavelength, but less potent than Ga-PpIX by an order of magnitude (Figure 4a). The dark toxicities of TMPyP and PpIX against *S. aureus* were evaluated and determined to be 7.4 μM and 36 μM, respectively, meaning that their photodynamic effects increased their potency by less than two orders of magnitude.

To establish the efficacy of Ga-PpIX-mediated aPDI against MDR strains of *S. aureus*, we tested several clinical isolates of MRSA known to exhibit resistance to various antibiotics including macrolides, aminoglycosides, lincosamides, and fluoroquinolones (Figure 4b and Table 1). Antimicrobial activity against these strains was achieved using 0.06−0.12 μM Ga-PpIX and 10 s of irradiation by the 405 nm LED source; increasing the irradiation time to 30 s guaranteed a 3-log reduction in all strains using 0.06 μM, with >6-log reduction in two cases. These results support our assumption that Ga-PpIX can be developed for aPDT against *S. aureus* infections, regardless of their MDR status. The consistent response to Ga-PpIX treatment is encouraging, as efficacy between strains can vary in antimicrobial photodynamic therapy.[43]

To determine whether Ga-PpIX-mediated aPDI could be achieved using a less powerful light source, experiments were also performed using a 20-W compact fluorescent lightbulb (CFL) with violet light emission near the Soret band of Ga-PpIX (λ_{max} 406 nm; Figure S7, Supporting Information). aPDI against *S. aureus* could be achieved at micromolar concentrations within 5 min and <1 μM within 15 min exposure to the CFL source, the latter corresponding with a 2-log increase in potency relative to dark toxicity (Figure 5 and Table S3, Supporting Information). Ga-PpIX mediated aPDI against clinical MRSA strains using the CFL source was comparable to that observed with the laboratory *S. aureus* strain (1−5 μM); the aPDI activity of PpIX was also evaluated with CFL irradiation and found to be less than that of Ga-PpIX as expected (Table S3). Overall, we find that Ga-PpIX can produce respectable levels of aPDI with an off-the-shelf CFL source, when using exposure times on the order of minutes. In this context, it is worth mentioning a recent report in which 5 μM of photosensitizer (TMPyP) was sufficient to produce aPDI using ambient lighting at a power density of 0.13 mW/cm^2, within a 10 min exposure time.[42]

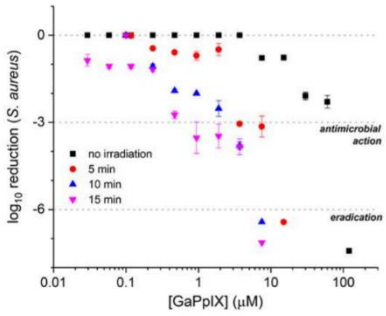

Figure 5. Normalized survival plots of *S. aureus* (PC 1203) as a function of Ga-PpIX concentration and exposure time to 406 nm light from a 20-W compact fluorescent lightbulb (CFL). Antimicrobial action and eradication correspond to 3- and 6-log CFU/mL reduction, respectively.

Cytotoxicity Studies. Ga-PpIX was tested for toxicity against human kidney cells (HEK293) and keratinocytes (HaCaT), the former to address potential systemic effects and the latter for topical exposure with and without light irradiation. HEK293 cells were evaluated for dark toxicity using the MTT assay following a 72-h incubation with Ga-PpIX from 0.6 μM up to 20 μM, above the limits needed for aPDI based on the response curves in Figure 5. Signs of mitochondrial cytotoxicity were observed starting at 5 μM (p < 0.05); however, cell viabilities remained above 90% even at the highest concentration (Figure 6a).

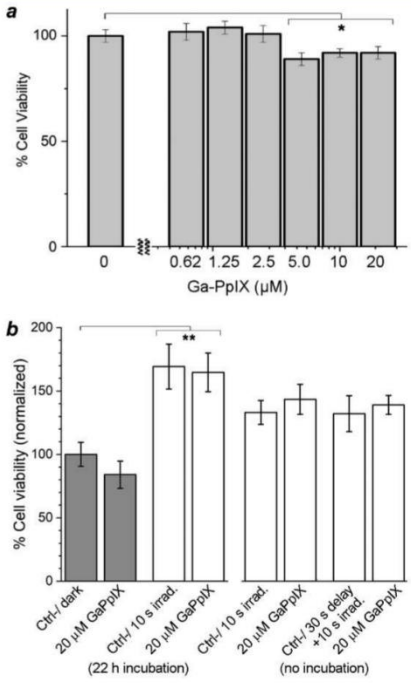

Figure 6. (a) Cytotoxicity of Ga-PpIX against HEK293 cells versus concentration; *, p < 0.05 (N = 3). (b) Effects of Ga-PpIX (20 μM) and 405 nm irradiation (10-s LED exposure) on HaCaT cells with different incubation times following treatment. Dark controls (no light exposure) presented in dark gray; **, p < 0.005 (N = 3). A complete set of p values is provided in the Supporting Information (Tables S4 and S5).

Viability assays were also performed with HaCaT cells using 20 μM Ga-PpIX and 10 s of irradiation by the LED source, with different incubation times (Figure 6b). Modest dark toxicity was observed after a 22-h incubation period (85% viability; p > 0.1), but a 10-s exposure to 405 nm irradiation stimulated cell growth or activity, with no adverse effect by Ga-PpIX (165−170% viability; p < 0.005). The stimulation of cell activities by short periods of laser or LED irradiation has been noted by others, particularly in the context of low-level light

DOI: 10.1021/acsinfecdis.8b00125
ACS Infect. Dis. 2018, 4, 1564−1573

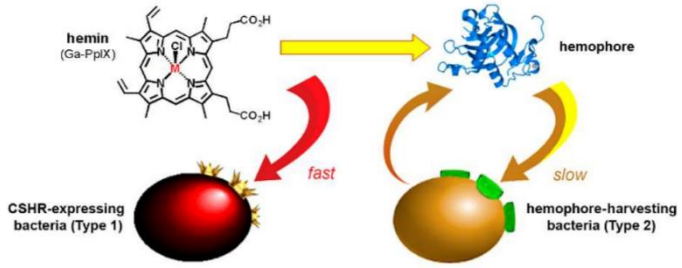

Figure 7. CSHR-expressing bacteria (Type 1) and hemophore-harvesting strains (Type 2), distinguished by their rates of hemin (or Ga-PpIX) uptake.[37]

therapy.[44] We thus conclude that Ga-PpIX mediated aPDI is compatible with mammalian systems, under the conditions presented in this study.

Rapid Uptake of Ga-PpIX by Other Bacterial Pathogens. *S. aureus* is not the only bacterial species that can express CSHRs enabling rapid hemin acquisition; indeed, studies aimed at elucidating the roles of specific heme transporters in aPDT are just now emerging.[45] To determine whether Ga-PpIX might be considered for targeted aPDT against additional pathogens, we developed a fluorescence imaging assay and screened a diverse panel of Gram-positive and negative bacteria for rapid Ga-PpIX uptake. On the basis of prior studies,[37] we expected bacteria to fall into three types: (1) those capable of rapid hemin acquisition via expression of CSHRs; (2) those that acquire hemin by the release and recovery of harvesting proteins (hemophores),[46] with a consequent delay in hemin acquisition rate; and (3) species that do not produce hemin-harvesting systems for iron acquisition (Figure 7).

Bacteria were typically cultivated under iron-deficient conditions and treated with Ga-PpIX at a fixed concentration for 15 to 60 min, then centrifuged and redispersed in PBS and imaged by fluorescence microscopy using a standard microscope. Those that achieved fluorescence saturation within the first 15 min were assigned as Type 1; those that accumulated fluorescence more slowly were assigned as Type 2 (Figure 8 and Table 2). Type 1 bacteria include Gram-positive species such as staphylococci (*S. aureus* and *S. epidermidis*), *Bacillus anthracis*, *Cornyebacterium diphtheria*, and *Streptococcus pneumoniae*. CSHRs for the first four species are well characterized, but the hemin acquisition system for *S. pneumoniae* is currently unassigned and awaits further study.[49,50] We note that at least two Type 1 pathogens are on government watchlists: *B. anthracis* can be weaponized for biological warfare with up to 90% mortality rate upon inhalation or ingestion,[47] and *S. pneumoniae* is a vector for community-acquired pneumonia, especially among young children.[2,3]

To further illustrate the differences in Ga-PpIX uptake between Type 1 and Type 2 bacteria, we performed confocal fluorescence microscopy on *S. aureus* and *Yersinia enterocolitica*, a Gram-negative species that acquires hemin through HemR, a TonB-dependent hemophore receptor.[56] As expected, *S. aureus* was strongly and uniformly labeled within the first 15 min, indicative of saturation; in contrast, the fluorescence of *Y. enterocolitica* was initially weak and heterogeneous but gradually increased over a 60 min period (Figure 9). This supports our hypothesis that hemin (or Ga-PpIX) acquisition

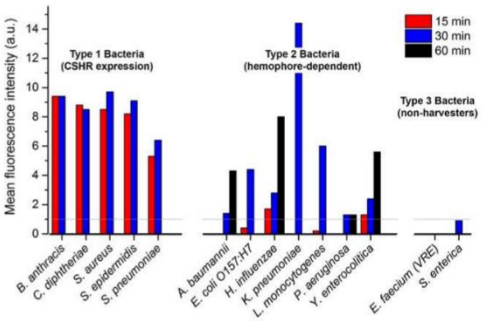

Figure 8. Ga-PpIX uptake by representative bacteria, classified into three types based on rates of saturation. Threshold of significance (gray line) is defined by the autofluorescence of *S. enterica*, a Type 3 species, and set at a unit value of one. Data for image analysis collected in triplicate; see Supporting Information for complete details.

by Type 2 bacteria is delayed by the extra step of hemophore retrieval (Figure 7).

In conclusion, CSHR-expressing pathogens such as *S. aureus* can be targeted for potent photodynamic inactivation within seconds using Ga-PpIX and 405 nm light irradiation. A structure–activity study reveals the importance of ionic character and the presence of free propionyl units in the specific uptake of Ga-PpIX. Antimicrobial activity is achieved with nanomolar Ga-PpIX using a monochromatic LED source; a lower but still respectable level of aPDI could be achieved with micromolar Ga-PpIX using an off-the-shelf CFL source. Ga-PpIX is highly active against several strains of MRSA, yet exhibits low dark toxicity against HEK293 cells and negligible phototoxicity against HaCaT cells under aPDI conditions, paving the path toward *in vivo* studies using skin infection models. Lastly, rapid Ga-PpIX uptake by several other (Type 1) pathogens has been established, broadening its potential scope for targeted aPDT.

■ EXPERIMENTAL SECTION

Hemin chloride and all reagents were obtained from commercial sources and used as received unless otherwise noted (see Supporting Information). The optimized syntheses of Ga-PpIX (**1**),[57] PpIX (**2**),[58] and derivatives **6**, **11**, and **12** are described in Supporting Information; the syntheses of Zn-

DOI: 10.1021/acsinfecdis.8b00125
ACS Infect. Dis. 2018, 4, 1564–1573

Table 2. Bacterial Pathogens Featured in Ga-PpIX Uptake Assay[a]

Bacteria, by Classification	Culture Conditions	Hemin Acquisition Proteins[c]
Type 1 (CSHRExpressing)		
Bacillus anthracis (Ames 35)	tryptic soy	Isd (C,E,X1,X2), BslK, Hal
Corynebacterium diphtheriae (5159)	brain–heart infusion	HmuT, Hta (A,B)[48]
Staphylococcus aureus(PCI 1203)	tryptic soy	Isd (A,B,C,E,H)
Staphylococcus epidermidis (ATCC 155)	tryptic soy	Isd (A,B,C,E,H)
Streptococcus pneumoniae (CDC CS111)	brain–heart infusion[b]	unassigned[49,50]
Type 2 (Hemophore Producing)		
Acinetobacter baumannii (DSM 6974)	nutrient broth	unassigned[51−53]
Escherichia coli O157:H7 (CDC EDL 933)	tryptic soy	ChuA, Hma, ShuA[54]
Klebsiella pneumoniae(S 389)	nutrient broth	unidentified[55]
Listeria monocytogenes(J0161)	brain–heart infusion	HupC, Hbp2/SvpA
Haemophilus influenzae (AMC 36-A-5)	gonococcal medium[b]	Hgp (A,B,C), Hup, HxuC
Pseudomonas aeruginosa (PAO1-LAC)	Luria–Bertani	Has (A,R), PhuR
Yersinia enterocolitica (WA-314)	Luria–Bertani	HemR
Type 3 (Nonharvesters)		
Enterococcus faecium (VRE)	brain–heart infusion	
Salmonella enterica typhimurium (LT2)	nutrient broth	

[a]Details taken from ref 46 unless otherwise noted. [b]5% CO_2 atmosphere. [c]Abbreviations: Bsl, *B. anthracis S*-layer; Chu, *E.coli* heme utilization; Hal, heme-acquisition leucine-rich; Has, heme acquisition system; Hbp, hemin binding protein; Hem, hemin receptor; Hgp, hemoglobin/haptoglobin binding protein; Hma, heme acquisition protein; Hmu, hemin uptake; Hta, hemin transport associated; Hup, heme uptake; Hxu, hemopexin uptake; Isd, iron-regulated surface determinant; Phu, *Pseudomonas* heme uptake; Shu, *Shigella* heme uptake; Svp, surface virulence-associated protein.

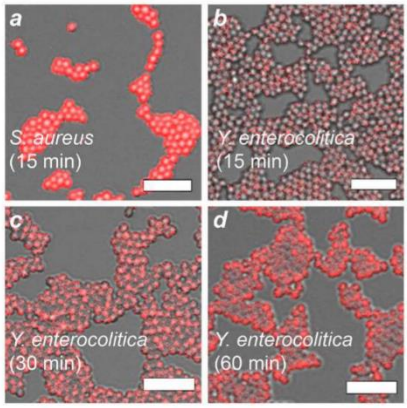

Figure 9. Confocal fluorescence microscopy of Ga-PpIX uptake (bar = 5 μm). (*a*) *S. aureus* after 15 min incubation; (b–d) *Y. enterocolitica* (ovoid form) after 15, 30, and 60 min incubation.

PpIX (**3**),[59] hematoporphyrin (HP; **4**) and Zn-HP (**5**),[60] PpIX dimethyl diester (**7**),[61] HP dimethyl diester (**8**),[61] and di-*O*-acetyl- and di-*O*-succinyl-HP dimethyl diester (**9**, **10**)[62] were synthesized from PpIX or HP as previously described in the literature. Absorption spectra were collected on a Varian Cary50 spectrometer. Photoemissions were measured on a Cary Eclipse fluorimeter with a gate time of 5 ms. EPR spectra were obtained using a Bruker EMX X-band spectrometer operating at 9.5 GHz and 5.02 mW, with a field modulation amplitude of 5 *g* at 100 kHz. Flow cytometry was performed using a BD Accuri C6 instrument ($\lambda_{ex}/\lambda_{em}$ = 488/585 nm). Fluorescence images were acquired using an upright microscope with Hg lamp and filter set for λ_{em} > 570 nm (Olympus BX51, U-MWG2), or a laser scanning confocal microscope with 488 nm excitation and appropriate bandpass filter (Olympus FV1000, DM405/488; BA505–605). Care was taken to minimize UV or laser exposure time to less than 5 s to avoid bleaching of molecules. Fluorescence data analyses were performed in triplicate using ImageJ 1.47v based on mean pixel intensities from labeled bacteria (8-bit format).

Microbiological Culture Conditions. Bacterial strains were obtained from the American Type Culture Collection (ATCC), BEI Resources, or Microbiologics, and cultured at 37 °C in an aerobic atmosphere unless otherwise noted. Bacterial suspensions were typically incubated for up to 16 h until an optical density of 1.0 was achieved at 600 nm. Bacterial counts were estimated in units of CFU/mL by plating serial dilutions onto agar plates, followed by incubation for 16 h at 37 °C. Iron-challenged conditions were typically achieved by first growing the bacteria in standard (iron-replete) media, then in media containing 3 mM 2,2′-bipyridine (Table 2). Further details and variations on bacterial culture conditions are provided in the Supporting Information.

Bacterial Uptake Assays of Ga-PpIX and Related Derivatives. Bacteria were cultured and assayed in iron-deficient media unless otherwise noted. A stock solution of Ga-PpIX (200 μM) was prepared by dispersing 2.54 mg in 1 mL of 10% DMSO in PBS for 10 min protected from light, followed by filtration and 20-fold dilution in PBS just prior to use. For flow cytometry, bacterial suspensions (10^8 CFU in 0.5 mL) were incubated with Ga-PpIX (73 μM) for specified periods (10 s–40 min), then fixed with 0.5 mL of 4% paraformaldehyde and subjected to analysis without further processing. A region of interest (ROI) based on forward scatter (FSC) and side scatter (SSC) parameters was used to gate bacterial populations (ca. 5×10^4 per data point) to exclude fluorescent debris.[63] For fluorescence imaging, bacterial suspensions (10^8 CFU in 0.5 mL) were incubated with Ga-PpIX or related derivatives (73 μM) for 15 min, then centrifuged and resuspended twice in 0.5 mL deionized water, then deposited onto glass slides in 10-μL aliquots and dried in air. More details on image processing and flow cytometry analysis are provided in the Supporting Information (Figures S3–S5).

Competitive Hemin Uptake Assay. Suspensions of *S. aureus* (PCI 1203) were centrifuged and redispersed 3 × in 0.5 mL PBS and adjusted to a concentration of 10^8 CFU/mL. Stock solutions of hemin and PpIX derivatives **1**–**13** were mixed in a 1:1 ratio (0.5 mL), then added to bacterial suspensions (10^8 CFU in 0.5 mL) and incubated for 15 min at room temperature. For control studies, hemin or fluorophore solutions were substituted with PBS to maintain constant concentration. Bacteria were harvested and washed as

DOI: 10.1021/acsinfecdis.8b00125
ACS Infect. Dis. 2018, 4, 1564–1573

described above and then evaluated by fluorescence microscopy for relative uptake efficiency.

Antimicrobial Photodynamic Inactivation (aPDI). Studies were performed in triplicate using 96-well microtiter plates with irradiation from a 405 nm LED array (Rainbow Technology Systems, 140 mW/cm^2) or a 20-W compact fluorescent lightbulb (CFL; Sunlite SL20/BLB) housed in an ellipsoidal reflector dome with emission at 406 nm (ca. 12.4 mW/cm^2; see Supporting Information). Antimicrobial assays were performed on planktonic bacteria at 10^7 CFU/mL with variable exposure times to CFL irradiation, followed by plating on agar and incubation at 37 °C. In a typical experiment, bacterial suspensions were transferred into microtiter plates then treated with 100-μL aliquots of Ga-PpIX with final concentrations ranging from 0.03 to 120 μM, followed immediately with LED irradiation (10 s) or CFL irradiation (up to 15 min). The irradiated bacteria were plated onto agar in serial 10-fold dilutions (10^7–10^1 CFU/mL); controls included one set of wells without photosensitizer (Ctrl$^+$) and one set of wells with photosensitizer but without irradiation (dark toxicity). Bacterial counts were determined by the drop-plate method using TS–agar plates[64] and recorded as mean log values with an error of one standard deviation. Bacterial susceptibilities were quantified by subtracting mean log values from an initial value of 7, with the threshold for antimicrobial activity defined as a 3-log reduction in cell count.

Cytotoxicity (MTT Oxidation) Assays. HEK293 cells (ATCC CRL-1573) and HaCaT cells (AddexBio) were cultured in DMEM containing 10% FBS, and incubated at 37 °C in a 5% CO_2 atmosphere, with multiple passages before use. Trypsinized cells were added to 96-well microtiter plates (10^4 cells/well) and incubated for 18–24 h before treatment with Ga-PpIX (100 μM stock solution), with final concentrations ranging from 0.6 to 20 μM. Control wells were treated with DMEM/FBS (Ctrl$^+$) or 0.005% Triton X-100 in media (Ctrl$^-$). HEK293 cells were incubated for 72 h, then treated with MTT (5 mg/mL, 10 μL/well) and incubated for another 4 h at 37 °C. HaCaT cells were treated with 20 μM Ga-PpIX and irradiated for 10 s using the 405 nm LED source, then incubated for 0 or 22 h prior to MTT treatment. All cells were fixed by adding 0.1 M HCl in isopropanol containing 10% Triton X-100 (100 μL/well) and mixed for 12 h on a plate rocker in dark at room temperature. Absorbance readings were acquired at 570 nm (main absorbance) and 650 nm (background).

■ ASSOCIATED CONTENT

Supporting Information

The Supporting Information is available free of charge on the ACS Publications website at DOI: 10.1021/acsinfecdis.8b00125.

Data from photophysical measurements of Ga-PpIX; microbiological culture conditions; details of fluorescence imaging and analysis; data from competitive uptake assays; details on LED and CFL sources; additional data from aPDI studies using CFL source; *t*-tests for cytotoxicity assays; synthesis and ^{1}H NMR spectra of PpIX derivatives **1**, **2**, **6**, **11**, and **12** (PDF)

■ AUTHOR INFORMATION

Corresponding Author

*E-mail: alexwei@purdue.edu.

ORCID

Ana V. Morales-de-Echegaray: 0000-0002-9468-5068
Waleed Younis: 0000-0001-5572-0142
Mohamed N. Seleem: 0000-0003-0939-0458
Alexander Wei: 0000-0002-8587-1037

Notes

The authors declare no competing financial interest.

■ ACKNOWLEDGMENTS

The authors acknowledge financial support from the Department of Defense (W911SR-08-C-0001) through the U.S. Army RDECOM (Edgewood Contracting Division), the National Science Foundation (CMMI-1449358), the National Institutes of Health (R01 AI130186), and the Purdue University Center for Cancer Research (P30 CA023168). We thank BEI Resources at NIAID for providing several of the bacterial strains used in this study, David McMillin for assistance with fluorimetry, María Mercado Ojeda and Zackery Hernandez for contributions toward antimicrobial studies, Gregory Knipp for providing HEK293 cells, and Kathy Raghed and J. Paul Robinson for their kind assistance with flow cytometry.

■ REFERENCES

(1) Tarai, B., Das, P., and Kumar, D. (2013) Recurrent challenges for clinicians: Emergence of methicillin-resistant *Staphylococcus aureus*, vancomycin resistance, and current treatment options. *J. Lab. Physicians 5*, 71–78.

(2) (2013) *Antibiotic Resistance Threats in the United States*, Centers for Disease Control and Prevention, Atlanta, GA.

(3) (2014) *Antimicrobial Resistance: Global Report on Surveillance. Fact Sheet No. 194*, World Health Organization.

(4) Rodvold, K. A., and McConeghy, K. W. (2014) Methicillin-Resistant *Staphylococcus aureus* Therapy: Past, Present, and Future. *Clin. Infect. Dis. 58*, S20–S27.

(5) Gu, B., Kelesidis, T., Tsiodras, S., Hindler, J., and Humphries, R. M. (2013) The emerging problem of linezolid-resistant *Staphylococcus*. *J. Antimicrob. Chemother. 68*, 4–11.

(6) Skiest, D. J. (2006) Treatment Failure Resulting from Resistance of *Staphylococcus aureus* to Daptomycin. *J. Clin. Microbiol. 44*, 655–656.

(7) Chambers, H. F., and DeLeo, F. R. (2009) Waves of Resistance: *Staphylococcus aureus* in the Antibiotic Era. *Nat. Rev. Microbiol. 7*, 629–641.

(8) Wainwright, M. (1998) Photodynamic antimicrobial chemotherapy (PACT). *J. Antimicrob. Chemother. 42*, 13–28.

(9) Hamblin, M. R., and Hasan, T. (2004) Photodynamic therapy: A new antimicrobial approach to infectious disease? *Photochem. Photobiol. Sci. 3*, 436–450.

(10) Giuliani, F., Martinelli, M., Cocchi, A., Arbia, D., Fantetti, L., and Roncucci, G. (2010) *In vitro* resistance selection studies of RLP068/Cl, a new Zn(II) phthalocyanine suitable for antimicrobial photodynamic therapy. *Antimicrob. Agents Chemother. 54*, 637–642.

(11) Agrawal, T., Avci, P., Gupta, G. K., Rineh, A., Lakshmanan, S., Batwala, V., Tegos, G. P., and Hamblin, M. R. (2015) Harnessing the power of light to treat staphylococcal infections focusing on MRSA. *Curr. Pharm. Des. 21*, 2109–2121.

(12) Zeina, B., Greenman, J., Corry, D., and Purcell, W. M. (2003) Antimicrobial photodynamic therapy: Assessment of genotoxic effects on keratinocytes *in vitro*. *Br. J. Dermatol. 148*, 229–232.

(13) Hongcharu, W., Taylor, C. R., Aghassi, D., Suthamjariya, K., Anderson, R. R., and Chang, Y. (2000) Topical ALA-Photodynamic Therapy for the Treatment of *Acne vulgaris*. *J. Invest. Dermatol. 115*, 183–192.

(14) Itoh, Y., Ninomiya, Y., Tajima, S., and Ishibashi, A. (2000) Photodynamic therapy for *Acne vulgaris* with topical 5-aminolevulinic acid. *Arch. Dermatol. 136*, 1093–1095.

DOI: 10.1021/acsinfecdis.8b00125
ACS Infect. Dis. 2018, 4, 1564–1573

(15) Braun, A., Dehn, C., Krause, F., and Jepsen, S. (2008) Short-term clinical effects of adjunctive antimicrobial photodynamic therapy in periodontal treatment: A randomized clinical trial. *J. Clin. Periodontol. 35*, 877−884.
(16) Sigusch, B. W., Engelbrecht, M., Völpel, A., Holletschke, A., Pfister, W., and Schütze, J. (2010) Full-Mouth Antimicrobial Photodynamic Therapy in *Fusobacterium nucleatum*−Infected Periodontitis Patients. *J. Periodontol. 81*, 975−981.
(17) Cassidy, C. M., Tunney, M. M., McCarron, P. A., and Donnelly, R. F. (2009) Drug delivery strategies for photodynamic antimicrobial chemotherapy: From benchtop to clinical practice. *J. Photochem. Photobiol., B 95*, 71−80.
(18) Kharkwal, G. B., Sharma, S. K., Huang, Y.-Y., Dai, T., and Hamblin, M. R. (2011) Photodynamic Therapy for Infections: Clinical Applications. *Lasers Surg. Med. 43*, 755−767.
(19) Maisch, T., Hackbarth, S., Regensburger, J., Felgenträger, A., Bäumler, W., Landthaler, M., and Röder, B. (2011) Photodynamic inactivation of multi-resistant bacteria (PIB) − a new approach to treat superficial infections in the 21st century. *J. Dtsch. Dermatol. Ges. 9*, 360−366.
(20) Septimus, E. J., and Schweizer, M. L. (2016) Decolonization in Prevention of Health Care-Associated Infections. *Clin. Microbiol. Rev. 29*, 201−222.
(21) Alonso, C., and Boyle, R. W. (2010) Bioconjugates of Porphyrins and Related Molecules for Photodynamic Therapy. In *Handbook of Porphyrin Science* (Kadish, K. M., Smith, K. M., and Guilard, R., Eds.) Vol. *4*, pp 121−190, World Scientific. DOI: DOI: 10.1142/9789814280228_0017.
(22) Dickson, E. F. G., Kennedy, J. C., Pottier, R. H., and Patrice, T. (2003) Photodynamic therapy using 5-aminolevulinic acid-induced protoporphyrin IX. In *Photodynamic Therapy* (Patrice, T., Ed.) pp 81−104 Royal Society of Chemistry, Cambridge. DOI: DOI: 10.1039/9781847551658-00081.
(23) Malik, Z., Hanania, J., and Nitzan, Y. (1990) New trends in photobiology bactericidal effects of photoactivated porphyrins– An alternative approach to antimicrobial drugs. *J. Photochem. Photobiol., B 5*, 281−293.
(24) Pilpa, R. M., Robson, S. A., Villareal, V. A., Wong, M. L., Phillips, M., and Clubb, R. T. (2009) Functionally distinct NEAT (NEAr Transporter) domains within the *Staphylococcus aureus* IsdH/HarA protein extract heme from methemoglobin. *J. Biol. Chem. 284*, 1166−1176.
(25) Behnam Azad, B., Cho, C. F., Lewis, J. D., and Luyt, L. G. (2012) Synthesis, radiometal labelling and in vitro evaluation of a targeted PPIX derivative. *Appl. Radiat. Isot. 70*, 505−511.
(26) Hu, Y., Geissinger, P., and Woehl, J. C. (2011) Potential of protoporphyrin IX and metal derivatives for single molecule fluorescence studies. *J. Lumin. 131*, 477−481.
(27) Bonnett, R., and Martínez, G. (2001) Photobleaching of sensitisers used in photodynamic therapy. *Tetrahedron 57*, 9513−9547.
(28) Stojiljkovic, I., Kumar, V., and Srinivasan, N. (1999) Non-iron metalloporphyrins: Potent antibacterial compounds that exploit haem/Hb uptake systems of pathogenic bacteria. *Mol. Microbiol. 31*, 429−442.
(29) Wilks, A., and Barker, K. D. (2010) Mechanisms of Heme Uptake and Utilization in Bacterial Pathogens. In *Handbook of Porphyrin Science* (Kadish, K. M., Smith, K. M., and Guilard, R., Eds.) pp 357−398, World Scientific, Singapore. DOI: DOI: 10.1142/9789814322386_0024.
(30) Olczak, T., Maszczak-Seneczko, D., Smalley, J. W., and Olczak, M. (2012) Gallium(III), cobalt(III) and copper(II) protoporphyrin IX exhibit antimicrobial activity against *Porphyromonas gingivalis* by reducing planktonic and biofilm growth and invasion of host epithelial cells. *Arch. Microbiol. 194*, 719−724.
(31) Arivett, B. A., Fiester, S. E., Ohneck, E. J., Penwell, W. F., Kaufman, C. M., Relich, R. F., and Actis, L. A. (2015) Antimicrobial Activity of Gallium Protoporphyrin IX against *Acinetobacter baumannii* Strains Displaying Different Antibiotic Resistance Phenotypes. *Antimicrob. Agents Chemother. 59*, 7657−7665.
(32) Bhaumik, J. (2007) *Synthetic Porphyrinic Macrocycles for Photodynamic Therapy and Other Biological Applications*, Ph.D. Thesis, North Carolina State University, Raleigh, NC.
(33) Hammer, N. D., and Skaar, E. P. (2011) Molecular mechanisms of *Staphylococcus aureus* iron acquisition. *Annu. Rev. Microbiol. 65*, 129−147.
(34) Maresso, A. W., Garufi, G., and Schneewind, O. (2008) *Bacillus anthracis* secretes proteins that mediate heme acquisition from hemoglobin. *PLoS Pathog. 4*, e1000132.
(35) Nakamura, K., Ishiyama, K., Ikai, H., Kanno, T., Sasaki, K., Niwano, Y., and Kohno, M. (2011) Reevaluation of analytical methods for photogenerated singlet oxygen. *J. Clin. Biochem. Nutr. 49*, 87−95.
(36) Frederiksen, P. K., McIlroy, S. P., Nielsen, C. B., Nikolajsen, L., Skovsen, E., Jørgensen, M., Mikkelsen, K. V., and Ogilby, P. R. (2005) Two-Photon Photosensitized Production of Singlet Oxygen in Water. *J. Am. Chem. Soc. 127*, 255−269.
(37) Maltais, T. R., Adak, A. K., Younis, W., Seleem, M. N., and Wei, A. (2016) Label-free detection and discrimination of bacterial pathogens based on hemin recognition. *Bioconjugate Chem. 27*, 1713−1722.
(38) Carpenter, B. M., Whitmire, J. M., and Merrell, D. S. (2009) This is not your mother's repressor: The complex role of *fur* in pathogenesis. *Infect. Immun. 77*, 2590−2601.
(39) Wakeman, C. A., Stauff, D. L., Zhang, Y., and Skaar, E. P. (2014) Differential Activation of *Staphylococcus aureus* Heme Detoxification Machinery by Heme Analogues. *J. Bacteriol. 196*, 1335−1342.
(40) Moriwaki, Y., Caaveiro, J. M. M., Tanaka, Y., Tsutsumi, H., Hamachi, I., and Tsumoto, K. (2011) Molecular basis of recognition of antibacterial porphyrins by heme-transporter IsdH-NEAT3 of *Staphylococcus aureus*. *Biochemistry 50*, 7311−7230.
(41) Eichner, A., Gonzales, F. P., Felgentrager, A., Regensburger, J., Holzmann, T., Schneider-Brachert, W., Baumler, W., and Maisch, T. (2013) Dirty hands: photodynamic killing of human pathogens like EHEC, MRSA and *Candida* within seconds. *Photochem. Photobiol. Sci. 12*, 135−147.
(42) Eckl, D. B., Dengler, L., Nemmert, M., Eichner, A., Bäumler, W., and Huber, H. (2018) A Closer Look at Dark Toxicity of the Photosensitizer TMPyP in Bacteria. *Photochem. Photobiol. 94*, 165−172.
(43) Nakonieczna, J., and Grinholc, M. (2012) Photodynamic inactivation requires innovative approach concerning numerous bacterial isolates and multicomponent sensitizing agents. *Photodiagn. Photodyn. Ther. 9*, 359−361.
(44) Hashmi, J., Huang, Y., Sharma, S., Kurup, D., De Taboada, L., Carroll, J., and Hamblin, M. (2010) Effect of pulsing in low-level light therapy. *Lasers Surg. Med. 42*, 450−466.
(45) Nakonieczna, J., Kossakowska-Zwierucho, M., Filipiak, M., Hewelt-Belka, W., Grinholc, M., and Bielawski, K. (2016) Photoinactivation of *Staphylococcus aureus* using protoporphyrin IX: the role of haem-regulated transporter HrtA. *Appl. Microbiol. Biotechnol. 100*, 1393−1405.
(46) Crosa, J. H., Mey, A. R., and Payne, S. M. (2004) *Iron Transport in Bacteria*, ASM Press, Washington, D.C. DOI: DOI: 10.1128/9781555816544.
(47) Spencer, R. C. (2003) Bacillus anthracis. *J. Clin. Pathol. 56*, 182−187.
(48) Allen, C. E., and Schmitt, M. P. (2009) HtaA is an iron-regulated hemin binding protein involved in the utilization of heme iron in *Corynebacterium diphtheriae*. *J. Bacteriol. 191*, 2638−2648.
(49) Tai, S. S., Lee, C. J., and Winter, R. E. (1993) Hemin utilization is related to virulence of *Streptococcus pneumoniae*. *Infect. Immun. 61*, 5401−5405.
(50) Romero-Espejel, M. E., Gonzalez-Lopez, M. A., and de Jesus Olivares-Trejo, J. (2013) *Streptococcus pneumoniae* requires iron for its

DOI: 10.1021/acsinfecdis.8b00125
ACS Infect. Dis. 2018, 4, 1564−1573

viability and expresses two membrane proteins that bind haemoglobin and haem. *Metallomics 5*, 384−389.
(51) McConnell, M. J., Actis, L., and Pachon, J. (2013) *Acinetobacter baumannii*: human infections, factors contributing to pathogenesis and animal models. *FEM Microbiol. Rev. 37*, 130−155.
(52) Zimbler, D., Penwell, W., Gaddy, J., Menke, S., Tomaras, A., Connerly, P., and Actis, L. (2009) Iron acquisition functions expressed by the human pathogen *Acinetobacter baumannii*. *BioMetals 22*, 23−32.
(53) Eijkelkamp, B. A., Hassan, K. A., Paulsen, I. T., and Brown, M. H. (2011) Investigation of the human pathogen *Acinetobacter baumannii* under iron limiting conditions. *BMC Genomics 12*, 126.
(54) Torres, A. G., and Payne, S. M. (1997) Haem iron-transport system in enterohaemorrhagic *Escherichia coli* O157:H7. *Mol. Microbiol. 23*, 825−833.
(55) Fouts, D. E., Tyler, H. L., DeBoy, R. T., Daugherty, S., Ren, Q., Badger, J. H., Durkin, A. S., Huot, H., Shrivastava, S., Kothari, S., et al. (2008) Complete Genome Sequence of the N2-Fixing Broad Host Range Endophyte *Klebsiella pneumoniae* 342 and Virulence Predictions Verified in Mice. *PLoS Genet. 4*, e1000141.
(56) Stojiljkovic, I., and Hantke, K. (1992) Hemin uptake system of *Yersinia enterocolitica*: similarities with other TonB-dependent systems in Gram-negative bacteria. *EMBO J. 11*, 4359−4367.
(57) Bohle, D. S., Dodd, E. L., Pinter, T. B. J., and Stillman, M. (2012) Soluble diamagnetic model for malaria pigment: Coordination chemistry of gallium(III)protoporphyrin-IX. *Inorg. Chem. 51*, 10747−10761.
(58) Erdman, J. G., Ramsey, V. G., Kalenda, N. W., and Hanson, W. E. (1956) Synthesis and properties of porphyrin vanadium complexes. *J. Am. Chem. Soc. 78*, 5844−5847.
(59) Clark, E., and Kurtz, D. M. (2017) Photosensitized H_2 production using a zinc porphyrin-substituted protein, platinum nanoparticles, and ascorbate with no electron relay: participation of Good's buffers. *Inorg. Chem. 56*, 4584.
(60) Xu, S., Hu, B., Cui, Q., Zhou, W., Luo, H., and Liu, Z. (2011) Synthesis of 3,8-bisacetyl deuteroporphyrin dimethyl ester. *Chin. J. Appl. Chem. 28*, 657−661.
(61) Byrne, C. J., and Ward, A. D. (1988) A facile porphyrin esterification/etherification procedure. *Tetrahedron Lett. 29*, 1421−1424.
(62) Bonnett, R., Ridge, R. J., Scourides, P. A., and Berenbaum, M. C. (1981) On the nature of 'haematoporphyrin derivative'. *J. Chem. Soc., Perkin Trans. 1*, 3135−3140.
(63) Benincasa, M., Barrière, Q., Runti, G., Pierre, O., Bourge, M., Scocchi, M., and Mergaert, P. (2016) Single Cell Flow Cytometry Assay for Peptide Uptake by Bacteria. *Bio-Protocol 6*, e2038.
(64) Herigstad, B., Hamilton, M., and Heersink, J. (2001) How to optimize the drop plate method for enumerating bacteria. *J. Microbiol. Methods 44*, 121−129.

DOI: 10.1021/acsinfecdis.8b00125
ACS Infect. Dis. 2018, 4, 1564−1573

Environmental Science & Technology Letters

Letter

pubs.acs.org/journal/estlcu

Protein Corona Analysis of Silver Nanoparticles Exposed to Fish Plasma

Jiejun Gao,[†] Lu Lin,[‡] Alexander Wei,*[,‡] and Maria S. Sepúlveda*[,†]

[†]Department of Forestry and Natural Resources and Bindley Biosciences Center and [‡]Department of Chemistry, Purdue University, West Lafayette, Indiana 47907, United States

Supporting Information

ABSTRACT: Nanoparticles (NPs) in contact with biological fluids experience changes in surface chemistry that can impact their biodistribution and downstream physiological impact. One such change involves the formation of a protein corona (PC) on the surface of NPs. Here we present a foundational study of PC formation following the incubation of polyvinylpyrrolidone-coated AgNPs (PVP-AgNPs, 50 nm) in the plasma of smallmouth bass (*Micropterus dolomieu*). The level of PC formation increases with exposure time and is also affected by gender, with AgNPs incubated in male plasma having PCs slightly thinner than and ζ potentials less negative than those of AgNPs incubated in female plasma. Proteomic analysis also revealed gender-specific differences in PC composition: in particular, egg-specific proteins (vitellogenin and zona pellucida) were identified in only PCs derived from female plasma, raising the possibility of their roles in AgNP-related reproductive toxicity by promoting their accumulation in developing oocytes.

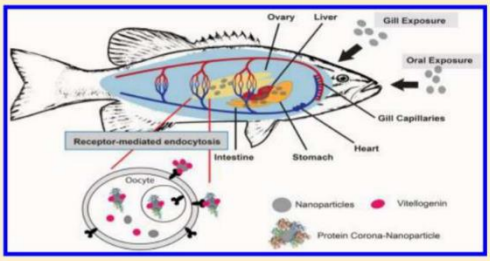

INTRODUCTION

Silver NPs (AgNPs) have been studied extensively as agents of concern in ecotoxicology. In fish populations, numerous studies have shown that AgNPs can cause hatching delays, abnormal larval development, and early mortality in juveniles.[1−3] AgNPs are known to induce the level of expression of genes related to metal detoxification and radical scavenging action and can also activate pro-inflammatory responses to oxidative stress that can result in cellular and DNA damage.[4,5] AgNPs are widely distributed throughout the fish body: in addition to the vascular system and alimentary canal, they have been found in the brain, heart, yolk, retina, gill arches, and ovaries.[1,6] The toxicological impact of AgNPs on humans and other organisms has not yet been adequately defined by scientific data, in part because of limitations in mechanistic insights. However, it is known that NPs in mammalian serum or plasma nucleate the rapid and dynamic formation of a protein corona (PC), whose "biological identity" can influence their biodistribution and uptake with subsequent effects on cell and organ function.[7−10] For example, the PC composition can promote or deter the interaction of NPs with outer membrane receptors for specific cell uptake[11,12] or impact their blood circulation lifetime.[13,14]

PC formation is governed by both protein−NP and protein−protein interactions. Factors that influence PC composition can be intrinsic (size and topology, surface chemistry, and charge density) or extrinsic (protein activities, pH, and ionic strength).[15−17] Exposure time is also important, as the dynamics of surface adsorption and exchange can cause the PC size and composition to evolve substantially over relatively short periods. For example, the thickness of PCs formed on silica and polystyrene NPs of variable size and surface chemistry has been observed to increase over time, with the PC composition remaining roughly constant.[17]

Nearly all PC studies are based on NPs exposed to mammalian serum or plasma.[18−23] Similar phenomena should occur in other vertebrate species such as fish; however, studies involving fish plasma are just now emerging.[33] Here we provide a foundational study of PCs formed upon exposure of NPs to plasma extracted from male and female smallmouth bass (*Micropterus dolomieu*), one that offers valuable insights into how NPs might accumulate in specific organs. We observed PCs on polyvinylpyrrolidone (PVP)-coated AgNPs to undergo time-dependent changes in size and composition. Notably, compositional differences are gender-dependent, with PCs derived from female bass containing significant levels of vitellogenin (VTG) and zona pellucida (ZP), proteins known to be critical for egg development. These novel findings suggest a mechanism for the accumulation of NPs in ovaries and developing eggs, via targeted delivery to follicular cells expressing cognate receptors.

Received: March 2, 2017
Revised: April 2, 2017
Accepted: April 7, 2017
Published: April 7, 2017

DOI: 10.1021/acs.estlett.7b00074
Environ. Sci. Technol. Lett. 2017, 4, 174−179

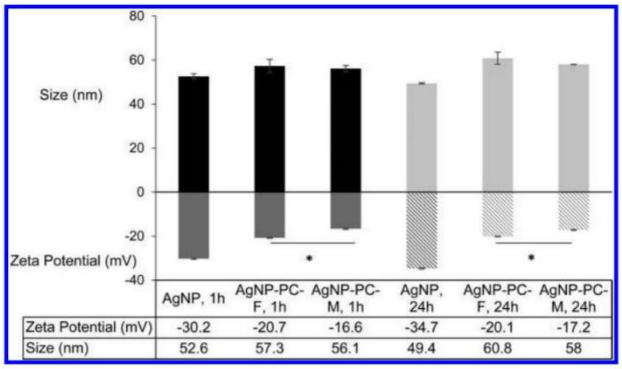

	AgNP, 1h	AgNP-PC-F, 1h	AgNP-PC-M, 1h	AgNP, 24h	AgNP-PC-F, 24h	AgNP-PC-M, 24h
Zeta Potential (mV)	-30.2	-20.7	-16.6	-34.7	-20.1	-17.2
Size (nm)	52.6	57.3	56.1	49.4	60.8	58

Figure 1. Changes in the hydrodynamic size and ζ potential (mode $\pm$ standard error; $N = 3$) of PVP-AgNPs, before and after incubation with fish plasma extracted from adult female (F) or male (M) smallmouth bass for 1 or 24 h. Untreated PVP-AgNPs were measured at 1 and 24 h to determine changes in size and ζ potential over time. Gender-related differences in ζ potential after protein corona (PC) formation were also established ($*p < 0.05$).

■ MATERIALS AND METHODS

Smallmouth Bass Plasma Collection. Ten adult fish (six females and four males) were collected from the St. Joseph River (Elkhart, IN) during the peak of their spawning season (middle to late March). Fish were captured uninjured using electrofishing methods. Blood samples (~1 mL) were collected and kept on ice prior to centrifugation (1000*g* for 20 min); the resulting plasma was frozen and stored at −80 °C until it could be further processed. Fish were dissected after bleeding for confirmation of gender.[24]

VTG Analysis. The presence or absence of VTG in plasma was confirmed by Western blotting (Figure S1). The primary antibody used was a polyclonal anti-VTG antibody from Biosense (Bergen, Norway), imaged by a secondary antibody labeled with IRDye 700 (Li-Cor, Lincoln, NE). Vascular endothelial growth factor (VEGF) was used as a reference protein, as it is expressed at steady levels in fish plasma, and detected using a polyclonal antibody from Anaspec (Fremont, CA) and a secondary antibody labeled with IRDye 800 (Li-Cor). Plasma samples were pooled by gender, as VTG was found in only female plasma.

Characterization of PVP-AgNPs and Their Protein Coronas. PVP-AgNPs (50 nm, Nanocomposix, San Diego, CA) were used as provided and incubated with either female or male bass plasma (NP:protein weight ratio of 1:500) for 1 or 24 h. Untreated PVP-AgNPs and fish plasma without PVP-AgNPs were included as controls. The dispersion stability was characterized by ultraviolet−visible (UV−vis) spectroscopy using a Cary-50 spectrophotometer (Varian, Palo Alto, CA). Nanoparticle tracking analysis (NTA) was performed at 25 °C using a Nanosight LM-10 (Malvern Instruments, Marlborough, MA) to quantify particle size distribution. The hydrodynamic size and ζ potentials were measured at 25 °C using a Zetasizer NanoZS (Malvern).

Isolation and Sodium Dodecyl Sulfate−Polyacrylamide Gel Electrophoresis (SDS−PAGE) Analysis of PC-Coated NPs. PVP-AgNPs (1 μg/mL) coated with fish plasma proteins (1 μg/mL) were incubated at 30 °C for 1 or 24 h and then collected by centrifugation (15000*g* for 20 min at 4 °C). Solid pellets were separated from free plasma, then redispersed in a fresh solution, and digested following a published protocol.[25] Aliquots were eluted by 12% SDS−PAGE and visualized with a silver stain kit (Thermo Fisher Scientific, Rockford, IL).

Liquid Chromatography−Mass Spectrometry (LC−MS) Analysis. Protein corona pellets were digested for LC−MS/MS analysis,[26] using a Dionex UltiMate 3000 RSLC Nano System coupled to a Q Exactive HF Hybrid Quadrupole-Orbitrap mass spectrometer (Thermo Scientific, Waltham, MA). A database search of nonredundant proteins from chordates (NCBI) was performed using the Mascot MS/MS Ion Server (Matrix Science, Boston, MA). Relative mass fractions of proteins were estimated with the exponentially modified protein abundance index;[27] additional details are provided in the Supporting Information.

Statistical Analysis. All statistical analyses were conducted using SPSS 22.0. One-way analysis of variance (ANOVA) followed by post hoc Tukey's multiple-comparison tests was used to compare means across treatments.

■ RESULTS AND DISCUSSION

UV−vis analysis of PVP-AgNPs indicates an absorption peak at 430 nm, with a 10 nm red-shift upon PC formation (Figure S2). A 5 nm increase in hydrodynamic size is observed after the first hour of incubation with fish plasma, with a further increase (2−3 nm) after a 24 h period (Figure 1). In addition, the ζ potentials for PC-coated AgNPs are less negative after the first hour of incubation and remain essentially the same after 24 h. The changes in size and ζ potential are both expected: with regard to the latter, adsorption of protein to negatively charged NPs has been observed previously to reduce ζ potentials.[17,28,29] It is well-known that the early adsorption of proteins to NP surfaces is kinetically driven and often dominated by hydrophobic species such as apolipoproteins (see below); however, the population of these high-abundance species declines as they are replaced with proteins with lower abundance but higher affinity for the NP surface or components in the inner "hard" corona layer.[8−10] It should be mentioned that incubation of PVP-AgNPs in fish plasma resulted in some agglomeration and colloidal instability, especially for AgNPs incubated in male plasma for 24 h. This is again not surprising, as the kinetic destabilization of imperfectly passivated metal colloids is well-

DOI: 10.1021/acs.estlett.7b00074
Environ. Sci. Technol. Lett. 2017, 4, 174−179

known. Nevertheless, NTA indicates the great majority of AgNPs to be stable, with an overall size increase due to PC formation (Figure S3).

We also observe a significant, gender-based difference in PC formation. Specifically, PVP-AgNPs added to male plasma exhibit a larger change in ζ potential relative to those added to female plasma ($p < 0.05$), whereas differences in hydrodynamic size are less significant. This observation is in contrast to the only other study of gender-related effects in PC formation using 20 nm AgNPs exposed to human plasma, which reported minimal physical or biochemical differences.[29] We attribute the gender-related differential in ζ potentials to variations in PC composition, which will be discussed below.

SDS−PAGE analysis provides additional evidence that PC composition is both gender-specific and time-dependent (Figure 2 and Figure S7). PCs derived from male fish plasma

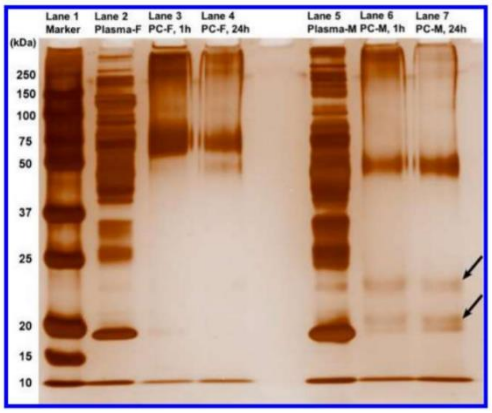

Figure 2. SDS−PAGE gel showing elution of proteins from protein coronas (PCs) formed after incubation of PVP-AgNPs with plasma from adult female (F) or male (M) smallmouth bass, for 1 or 24 h. Compositional differences can be correlated with both gender differences and incubation time. Significantly higher levels of smaller proteins (<25 kDa) were found in PCs isolated from male plasma (black arrows; see Figure S7 for a more heavily stained image). A decrease in the relative abundance of midsized proteins (50−80 kDa) was observed in PCs formed after incubation for 24 h in female plasma. Original female plasma and male plasma are included for comparison.

(lanes 6 and 7) contain significantly higher quantities of smaller proteins (<25 kDa), relative to those from female plasma. The profiles of corona proteins from either gender are also quite different than those in the parent fish plasma (lanes 2 and 5), indicating that PC formation is an innately selective process.

LC−MS/MS data indicate PCs derived from fish plasma contain a larger fraction of low-molecular weight proteins (≤25 kDa, >50% by mass) and a smaller fraction of high-molecular weight proteins (≥100 kDa, <10% by mass) relative to those in bulk plasma (Figure S4). In particular, PCs derived from female fish plasma carry an especially large fraction of <20 kDa proteins, which increased to >50% by mass after incubation for 24 h. The protein sizes and distributions in these PCs are in a range similar to those reported in studies involving citrate- and PVP-coated AgNPs (20 nm) in human plasma, in which the majority of the proteins were <60 kDa.[29] It is worth noting that the PC composition is also influenced by the chemistry of the core NP: for example, PCs formed on polystyrene NPs contain mostly proteins in the 60−70 kDa range, whereas PCs formed on silica NPs exposed to the same plasma source contain much larger proteins (150−200 kDa).[17]

A total of 337 proteins were identified in PC-coated AgNPs by LC−MS/MS proteomic analysis (Figure S5). For PCs derived from female fish plasma, 135 and 147 proteins were identified from AgNPs incubated for 1 and 24 h respectively; for those derived from male plasma, 194 and 193 proteins were identified. Fewer than 18% (60 proteins) were common to all PCs, and fewer than 40% (128 proteins) were shared between genders. These values are much lower than those of PCs formed on 20 nm AgNPs in human plasma, which shared 70% of all proteins between genders.[29] In PCs derived from female fish plasma, roughly two-thirds of the proteins (89 of 135) are common to both 1 and 24 h incubation samples, while the number of proteins unique to either condition is relatively low (n = 19 and 26, respectively). On the other hand, while more than half of the proteins in male-derived PCs (109 or 193) are found in both 1 and 24 h incubation conditions, a surprisingly large number of proteins are unique to a given sample (n = 67 and 64, respectively), an interesting finding that warrants further investigation.

The relative proportions of high-abundance proteins in PCs differs substantially from those in the bulk plasma. In both fish sexes, the populations of parvalbumin, apolipoproteins, and other lipid transport proteins in PCs are far smaller than that found in the bulk, whereas the proportion of immunoglobulins in PCs is significantly higher. The amount of hemoglobin in PCs is also initially higher than that of the bulk during the first hour but has receded by the 24 h mark. Furthermore, levels of fibrinogen and fibronectin in PCs isolated from male plasma are lower than those measured in the bulk and decrease over time; a similar trend is observed for the egg-specific proteins VTG and ZP in PCs isolated from female plasma. No correlations between relative abundance and function are being suggested at this time; however, the mere presence of serum proteins such as VTG and ZP may be sufficient to modulate the uptake and delivery of NPs to specific organs (see below).

The relative distribution of proteins in PCs derived from female and male fish plasma can be broken down according to their primary functions (Figure 3; for a complete list, see Tables S1 and S2). The most abundant proteins are those associated with the immune system (immunoglobulins and complement proteins), followed by those for vascular and oxygen transport (hemoglobin, plasminogen, and fibrinogen/fibronectin). Lipid transport proteins (lipoproteins and apolipoproteins) were also present but to a lesser extent; high-density lipoproteins (HDLs, ApoA) were associated with PVP-AgNPs regardless of gender or length of incubation. Low-density lipoproteins (LDLs) and two apolipoproteins (ApoB-100 and ApoE) were also found in all PCs. Earlier studies with polystyrene and silica NPs in human serum have yielded similar observations,[30,31] leading to hypotheses that lipid transport proteins may be involved in the movement of NPs from the bloodstream into organs and across the blood−brain barrier.[15]

Several other proteins were identified in significant quantities within PCs, some at much higher concentrations relative to that in the bulk plasma (Figure 3b). Ceruloplasmin and plasminogen are particularly noteworthy; other metal-ion regulators such as Ca^{+}/calmodulin-dependent protein kinase II (CaMKII) and transferrin are also present. Acute-phase

DOI: 10.1021/acs.estlett.7b00074
Environ. Sci. Technol. Lett. 2017, 4, 174−179

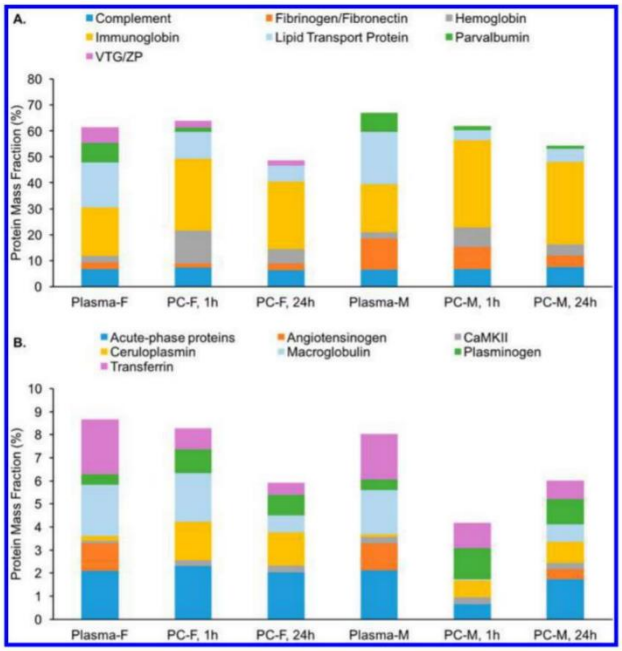

Figure 3. Protein corona (PC) compositions with the relative abundance of proteins by class, derived from PVP-coated AgNPs exposed to adult female (F) or male (M) fish plasma for 1 or 24 h. The composition of bulk plasma is shown for comparison. (A) Highest-percentage proteins within PCs. (B) Other significant proteins found in the PC layer. Abbreviations: CaMKII, calcium/calmodulin-dependent protein kinase; VTG, vitellogenin; ZP, zona pellucida.

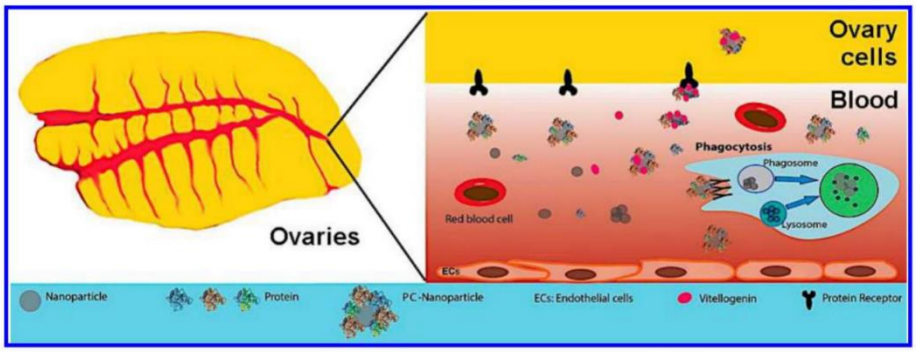

Figure 4. Hypothetical roles of corona proteins in the distribution and transport of silver nanoparticles (AgNPs) in fish plasma. AgNPs labeled with complement proteins and other opsonins are likely taken up into macrophages by phagocytosis, whereas those labeled with egg-specific proteins such as vitellogenin (VTG) may be transported into developing follicles within the ovaries by cognate receptors.

proteins associated with the inflammatory response are also represented within the PCs, including amyloid A, antitrypsin, kallikrein, kininogen, and vitamin K-dependent protein (Tables S1 and S2). Notably, many plasma proteins are incorporated preferentially into PCs while others appear to be excluded; for example, parvalbumin, lipid transport proteins, and macroglobulin are present at levels much lower than those in bulk plasma, and angiotensinogen (a blood pressure regulator) is hardly present at all, especially during the early stages of PC formation (Figure 3 and Figure S6).

The most significant finding in this study is the incorporation of VTG and ZP in PCs derived from female fish plasma. VTG, a precursor to egg yolk that plays critical roles in oogenesis, is synthesized in the liver and transported to the ovaries via the bloodstream.[32] The significant inclusion of VTG in PCs formed on SiO_2 NPs exposed in zebrafish plasma has also been

DOI: 10.1021/acs.estlett.7b00074
Environ. Sci. Technol. Lett. 2017, 4, 174−179

reported very recently, with evidence of sex-specific NP uptake by immune cells.[33] VTG and ZP are produced at elevated levels by female smallmouth bass during the spawning season and are taken up by developing follicles within fish ovaries by receptor-mediated endocytosis (Figure 4).[34,35] These egg-specific proteins are incorporated at an early stage of PC formation, but their levels decrease after a 24 h incubation, which suggests that they reside in the outer "soft" corona layer and are thus readily presented to follicular cells expressing their cognate receptors. This suggests that the biological response to PVP-AgNPs may depend not only on gender but also on the window of exposure during the fish's reproductive cycle.

Previous research has shown that AgNPs can accumulate in fish ovaries, which can lead to abnormal follicular development with subsequent loss of fecundity and reproductive capacity.[36−38] Early exposure of fish eggs to AgNPs or silver ions can also result in the defective development of embryos and larvae, resulting in their decreased rates of survival.[39−42] Given the rapid inclusion of VTG and ZP from female fish plasma into PCs, we postulate that these egg-specific proteins can promote translocation of AgNPs to the ovaries.

In summary, the PC around AgNPs exposed to fish plasma offers a rich source of information about the physiological condition of the host species. Unlike studies involving mammalian sera, gender plays an important role in PC composition, with significant differences in ζ potential, diversity, and relative proportions of the constituent proteins, and the incorporation of gender-specific protein markers. The latter may be important in directing circulating NPs to specific organs and tissues and promoting their uptake via cell-surface receptors. In particular, the inclusion of VTG and ZP in the PCs of AgNPs in the bloodstream of female fish may provide a mechanism for accelerating their movement to ovaries and developing eggs. Experiments to confirm this hypothesis will be performed in due course.

■ ASSOCIATED CONTENT

Supporting Information

The Supporting Information is available free of charge on the ACS Publications website at DOI: 10.1021/acs.estlett.7b00074.

Western blot analysis of vitellogenin, UV−vis absorption and NTA data of PVP-AgNPs and PC-AgNPs, and additional proteomics analysis, including tables of specific proteins identified under specific conditions (PDF)

■ AUTHOR INFORMATION

Corresponding Authors

*E-mail: mssepulv@purdue.edu. Phone: +1 765 496 3428.
*E-mail: alexwei@purdue.edu. Phone: +1 765 494 5257.

ORCID

Maria S. Sepúlveda: 0000-0003-0473-5760

Notes

The authors declare no competing financial interest.

■ ACKNOWLEDGMENTS

J.G. gratefully acknowledges the financial support of the China Scholarship Council and the Department of Forestry and Natural Resources, Purdue University. The authors also acknowledge support from the Purdue University Center for Cancer Research (P30 CA023168) and Vicki Hedrick in the Bindley Bioscience Center Proteomics Facility for assistance with protein digestions and LC−MS/MS analysis.

■ REFERENCES

(1) Asharani, P. V.; Lian Wu, Y.; Gong, Z.; Valiyaveettil, S. Toxicity of silver nanoparticles in zebrafish models. *Nanotechnology* **2008**, *19* (25), 255102.

(2) Gao, J.; Mahapatra, C. T.; Mapes, C. D.; Khlebnikova, M.; Wei, A.; Sepúlveda, M. S. Vascular toxicity of silver nanoparticles to developing zebrafish (*Danio rerio*). *Nanotoxicology* **2016**, *10*, 1363−1372.

(3) Bar-Ilan, O.; Albrecht, R. M.; Fako, V. E.; Furgeson, D. Y. Toxicity assessments of multisized gold and silver nanoparticles in zebrafish embryos. *Small* **2009**, *5* (16), 1897−1910.

(4) Chae, Y. J.; Pham, C. H.; Lee, J.; Bae, E.; Yi, J.; Gu, M. B. Evaluation of the toxic impact of silver nanoparticles on Japanese medaka (Oryzias latipes). *Aquat. Toxicol.* **2009**, *94* (4), 320−327.

(5) Laban, G.; Nies, L. F.; Turco, R. F.; Bickham, J. W.; Sepúlveda, M. S. The effects of silver nanoparticles on fathead minnow (*Pimephales promelas*) embryos. *Ecotoxicology* **2010**, *19* (1), 185−195.

(6) Lee, K. J.; Nallathamby, P. D.; Browning, L. M.; Osgood, C. J.; Xu, X. H. In vivo imaging of transport and biocompatibility of single silver nanoparticles in early development of zebrafish embryos. *ACS Nano* **2007**, *1* (2), 133−143.

(7) Salvati, A.; Pitek, A. S.; Monopoli, M. P.; Prapainop, K.; Bombelli, F. B.; Hristov, D. R.; Kelly, P. M.; Åberg, C.; Mahon, E.; Dawson, K. A. Transferrin-functionalized nanoparticles lose their targeting capabilities when a biomolecule corona adsorbs on the surface. *Nat. Nanotechnol.* **2013**, *8* (2), 137−143.

(8) Albanese, A.; Walkey, C. D.; Olsen, J. B.; Guo, H.; Emili, A.; Chan, W. C. Secreted biomolecules alter the biological identity and cellular interactions of nanoparticles. *ACS Nano* **2014**, *8* (6), 5515−5526.

(9) Pearson, R. M.; Juettner, V. V.; Hong, S. Biomolecular corona on nanoparticles: A survey of recent literature and its implications in targeted drug delivery. *Front. Chem.* **2014**, *2*, 108.

(10) Treuel, L.; Nienhaus, G. U. Toward a molecular understanding of nanoparticle−protein interactions. *Biophys. Rev.* **2012**, *4* (2), 137−147.

(11) Decuzzi, P.; Ferrari, M. The role of specific and non-specific interactions in receptor-mediated endocytosis of nanoparticles. *Biomaterials* **2007**, *28* (18), 2915−2922.

(12) Nel, A. E.; Mädler, L.; Velegol, D.; Xia, T.; Hoek, E. M.; Somasundaran, P.; Klaessig, F.; Castranova, V.; Thompson, M. Understanding biophysicochemical interactions at the nano-bio interface. *Nat. Mater.* **2009**, *8* (7), 543−557.

(13) Runa, S.; Hill, A.; Cochran, V. L.; Payne, C. K. PEGylated nanoparticles: protein corona and secondary structure. *Proc. SPIE* **2014**, *9165*, 91651F.

(14) Boles, M. A.; Ling, D.; Hyeon, T.; Talapin, D. V. The surface science of nanocrystals. *Nat. Mater.* **2016**, *15* (2), 141−153.

(15) Lundqvist, M.; Stigler, J.; Elia, G.; Lynch, I.; Cedervall, T.; Dawson, K. A. Nanoparticle size and surface properties determine the protein corona with possible implications for biological impacts. *Proc. Natl. Acad. Sci. U. S. A.* **2008**, *105* (38), 14265−14270.

(16) Pozzi, D.; Caracciolo, G.; Capriotti, A. L.; Cavaliere, C.; La Barbera, G.; Anchordoquy, T. J.; Laganà, A. Surface chemistry and serum type both determine the nanoparticle-protein corona. *J. Proteomics* **2015**, *119*, 209−217.

(17) Tenzer, S.; Docter, D.; Kuharev, J.; Musyanovych, A.; Fetz, V.; Hecht, R.; Schlenk, F.; Fischer, D.; Kiouptsi, K.; Reinhardt, C.; Landfester, K.; Schild, H.; Maskos, M.; Knauer, S. K.; Stauber, R. H. Rapid formation of plasma protein corona critically affects nanoparticle pathophysiology. *Nat. Nanotechnol.* **2013**, *8* (10), 772−781.

(18) Walkey, C. D.; Olsen, J. B.; Song, F.; Liu, R.; Guo, H.; Olsen, D. W.; Cohen, Y.; Emili, A.; Chan, W. C. Protein corona fingerprinting predicts the cellular interaction of gold and silver nanoparticles. *ACS Nano* **2014**, *8* (3), 2439−2455.

DOI: 10.1021/acs.estlett.7b00074
Environ. Sci. Technol. Lett. 2017, 4, 174−179

(19) Eigenheer, R.; Castellanos, E.; Nakamoto, M.; Gerner, K.; Lampe, A.; Wheeler, K. Silver nanoparticle protein corona composition compared across engineered particle properties and environmentally relevant reaction conditions. *Environ. Sci.: Nano* **2014**, *1*, 238−247.
(20) Shannahan, J. H.; Lai, X.; Ke, P. C.; Podila, R.; Brown, J. M.; Witzmann, F. A. Silver nanoparticle protein corona composition in cell culture media. *PLoS One* **2013**, *8* (9), e74001.
(21) Treuel, L.; Malissek, M.; Gebauer, J. S.; Zellner, R. The influence of surface composition of nanoparticles on their interactions with serum albumin. *ChemPhysChem* **2010**, *11* (14), 3093−3099.
(22) Wen, Y.; Geitner, N.; Chen, R.; Ding, F.; Chen, P.; Andorfer, R.; Govindan, P. N.; Ke, P. C. Binding of cytoskeletal proteins with silver nanoparticles. *RSC Adv.* **2013**, *3*, 22002−22007.
(23) Ding, F.; Radic, S.; Chen, R.; Chen, P.; Geitner, N. K.; Brown, J. M.; Ke, P. C. Direct observation of a single nanoparticle-ubiquitin corona formation. *Nanoscale* **2013**, *5* (19), 9162−9169.
(24) Zenobio, J. E.; Sanchez, B. C.; Leet, J. K.; Archuleta, L. C.; Sepúlveda, M. S. Presence and effects of pharmaceutical and personal care products on the Baca National Wildlife Refuge, Colorado. *Chemosphere* **2015**, *120*, 750−755.
(25) Docter, D.; Distler, U.; Storck, W.; Kuharev, J.; Wünsch, D.; Hahlbrock, A.; Knauer, S. K.; Tenzer, S.; Stauber, R. H. Quantitative profiling of the protein coronas that form around nanoparticles. *Nat. Protoc.* **2014**, *9* (9), 2030−2044.
(26) Hedrick, V. E.; LaLand, M. N.; Nakayasu, E. S.; Paul, L. N. Digestion, Purification, and Enrichment of Protein Samples for Mass Spectrometry. *Curr. Protoc Chem. Biol.* **2015**, *7* (3), 201−222.
(27) Ishihama, Y.; Oda, Y.; Tabata, T.; Sato, T.; Nagasu, T.; Rappsilber, J.; Mann, M. Exponentially modified protein abundance index (emPAI) for estimation of absolute protein amount in proteomics by the number of sequenced peptides per protein. *Mol. Cell. Proteomics* **2005**, *4* (9), 1265−1272.
(28) Casals, E.; Pfaller, T.; Duschl, A.; Oostingh, G. J.; Puntes, V. Time evolution of the nanoparticle protein corona. *ACS Nano* **2010**, *4* (7), 3623−3632.
(29) Huang, H.; Lai, W.; Cui, M.; Liang, L.; Lin, Y.; Fang, Q.; Liu, Y.; Xie, L. An Evaluation of Blood Compatibility of Silver Nanoparticles. *Sci. Rep.* **2016**, *6*, 25518.
(30) Lo Giudice, M. C.; Herda, L.; Polo, E.; Dawson, K. In situ characterization of nanoparticle biomolecular interactions in complex biological media by flow cytometry. *Nat. Commun.* **2016**, *7*, 13475.
(31) Lara, S.; Alnasser, F.; Polo, E.; Garry, D.; Lo Giudice, M. C.; Hristov, D.; Rocks, L.; Salvati, A.; Yan, Y.; Dawson, K. A. Identification of receptor binding to the biomolecular corona of nanoparticles. *ACS Nano* **2017**, *11* (2), 1884−1893.
(32) Hara, A.; Hiramatsu, N.; Fujita, T. Vitellogenesis and choriogenesis in fishes. *Fish. Sci.* **2016**, *82* (2), 187−202.
(33) Hayashi, Y.; Miclaus, T.; Murugadoss, S.; Takamiya, M.; Scavenius, C.; Kjaer-Sorensen, K.; Enghild, J.; Strähle, U.; Oxvig, C.; Weiss, C.; Sutherland, D. Female versus male biological identities of nanoparticles determine the interaction with immune cells in fish. *Environ. Sci.: Nano* **2017**, n/a.
(34) Pan, M. L.; Bell, W. J.; Telfer, W. H. Vitellogenic blood protein synthesis by insect fat body. *Science* **1969**, *165* (3891), 393−394.
(35) Wallace, R. A. Vitellogenesis and oocyte growth in non-mammalian vertebrates. In *Oogenesis*; Browder, L. W., Ed.; Plenum Press: New York, 1985; pp 127−177.
(36) Liu, X. Q.; Zhang, H. F.; Zhang, W. D.; Zhang, P. F.; Hao, Y. N.; Song, R.; Li, L.; Feng, Y. N.; Hao, Z. H.; Shen, W.; Min, L. J.; Yang, H. D.; Zhao, Y. Regulation of neuroendocrine cells and neuron factors in the ovary by zinc oxide nanoparticles. *Toxicol. Lett.* **2016**, *256*, 19−32.
(37) Zhang, W.-D.; Zhao, Y.; Zhang, H.-F.; Wang, S.-K.; Hao, Z.-H.; Liu, J.; Yuan, Y.-Q.; Zhang, P.-F.; Yang, H.-D.; Shen, W.; Li, L. Alteration of gene expression by zinc oxide nanoparticles or zinc sulfate *in vivo* and comparison with *in vitro* data: A harmonious case. *Theriogenology* **2016**, *86* (3), 850−861.
(38) Chatterjee, N.; Bhattacharjee, B. Revelation of ZnS Nanoparticles Induces Follicular Atresia and Apoptosis in the Ovarian Preovulatory Follicles in the Catfish *Mystus tengara* (Hamilton, 1822). *Scientifica* **2016**, *2016*, 3927340.
(39) Austin, C. A.; Umbreit, T. H.; Brown, K. M.; Barber, D. S.; Dair, B. J.; Francke-Carroll, S.; Feswick, A.; Saint-Louis, M. A.; Hikawa, H.; Siebein, K. N.; Goering, P. L. Distribution of silver nanoparticles in pregnant mice and developing embryos. *Nanotoxicology* **2012**, *6*, 912−922.
(40) Lee, Y.; Choi, J.; Kim, P.; Choi, K.; Kim, S.; Shon, W.; Park, K. A transfer of silver nanoparticles from pregnant rat to offspring. *Toxicol. Res.* **2012**, *28* (3), 139−41.
(41) Tabatabaei, S. R.; Moshrefi, M.; Askaripour, M. Prenatal Exposure to Silver Nanoparticles Causes Depression Like Responses in Mice. *Indian J. Pharm. Sci.* **2015**, *77* (6), 681−686.
(42) Morishita, Y.; Yoshioka, Y.; Takimura, Y.; Shimizu, Y.; Namba, Y.; Nojiri, N.; Ishizaka, T.; Takao, K.; Yamashita, F.; Takuma, K.; Ago, Y.; Nagano, K.; Mukai, Y.; Kamada, H.; Tsunoda, S.; Saito, S.; Matsuda, T.; Hashida, M.; Miyakawa, T.; Higashisaka, K.; Tsutsumi, Y. Distribution of Silver Nanoparticles to Breast Milk and Their Biological Effects on Breast-Fed Offspring Mice. *ACS Nano* **2016**, *10* (9), 8180−8191.

DOI: 10.1021/acs.estlett.7b00074
Environ. Sci. Technol. Lett. 2017, 4, 174−179

SCIENCE AND TECHNOLOGY OF ADVANCED MATERIALS, 2017
VOL. 18, NO. 01, 210–218
http://dx.doi.org/10.1080/14686996.2017.1290492

Taylor & Francis
Taylor & Francis Group

Eco-friendly (green) synthesis of magnetically active gold nanoclusters

Naveen Reddy Kadasala, Lu Lin, Christopher Gilpin and Alexander Wei

Department of Chemistry, Purdue University, West Lafayette, IN, USA

ABSTRACT

Au–Fe_xO_y composite nanoparticles (NPs) are of great technological interest due to their combined optical and magnetic properties. However, typical syntheses are neither simple nor ecologically friendly, creating a challenging situation for process scale-up. Here we describe conditions for preparing Au–Fe_xO_y NPs in aqueous solutions and at ambient temperatures, without resorting to solvents or amphiphilic surfactants with poor sustainability profiles. These magnetic gold nanoclusters (MGNCs) are prepared in practical yields with average sizes slightly below 100 nm, and surface plasmon resonances that extend to near-infrared wavelengths, and sufficient magnetic moment (up to 6 emu g^{-1}) to permit collection within minutes by handheld magnets. The MGNCs also produce significant photoluminescence when excited at 488 nm. Energy dispersive X-ray (EDX) analysis indicates a relatively even distribution of Fe within the MGNCs, as opposed to a central magnetic core.

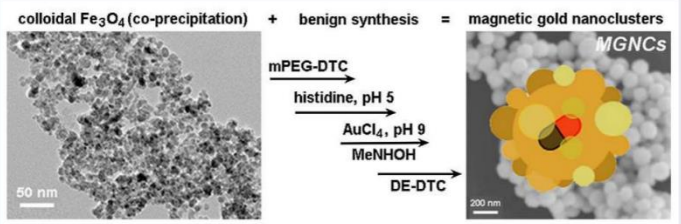

ARTICLE HISTORY
Received 12 October 2016
Revised 31 January 2017
Accepted 31 January 2017

KEYWORDS
Gold nanoparticles; magnetic properties; synthesis; composite materials; plasmon resonance; luminescence; sustainability

CLASSIFICATION
40 Optical; magnetic and electronic device materials; 102 Porous / Nanoporous / Nanostructured materials; 103 Composites; 106 Metallic materials; 203 Magnetics / Spintronics / Superconductors; 204 Optics / Optical applications; 301 Chemical syntheses / processing; 308 Materials resources / recycling; 501 Chemical analyses; 503 TEM, STEM, SEM

1. Introduction

Nanoparticles with hybrid magnetic–plasmonic properties are highly prized for applications in separations, biosensing, and nanomedicine [1–11]. These NPs are often comprised of a superparamagnetic iron-oxide core coated with a shell of metallic Au or Ag, which supports a localized plasmon resonance and a certain degree of chemical protection to the magnetic core. The metallic shells can be functionalized by a variety of surface chemistries, many of which enhance the dispersion and compatibility of NPs in biological media [12–19]. This has enabled the use of Au–Fe_xO_y NPs for isolating and purifying biomolecular species like proteins and DNA, as multimodal contrast agents in biomedical imaging, and as photothermal agents for hyperthermia-mediated cancer therapies [3,8,10,11,20–26]. The optical properties of these nanocomposites can also be exploited for surface-enhanced Raman scattering (SERS) and other plasmon-enhanced processes, for the specific detection of trace analytes in aqueous media [27–29].

Despite their strong technological potential, nearly all syntheses of Au–Fe_xO_y NPs have one or more steps that use nonpolar organic solvents, elevated temperatures, or a high concentration of non-biodegradable surfactants. All of these are negative factors from the perspective of sustainable manufacturing and lifecycle assessment, with significant burdens on the environment, energy consumption, and waste, which translates to higher production costs [30]. Sustainable manufacturing is practiced by chemical industries worldwide, with the intent of meeting the triple bottom-line goals of societal acceptance, cost-effective production, and environmental sustainability. Nano-manufacturing is based on similar principles, but must address inevitable tradeoffs between materials performance and sustainable production while still providing a net technological

CONTACT Alexander Wei alexwei@purdue.edu

advantage. We thus seek alternative, greener methods for synthesizing Au–Fe_xO_y NPs, with minimum concerns for environmental impact upon scaled production.

Recently, we reported a mild method of synthesizing magnetic gold nanoclusters (MGNCs) that is both simple and eco-friendly, and demonstrated their utility for detecting trace organic pollutants by SERS [29]. In this paper we describe an optimized and highly reproducible method for synthesizing MGNCs in aqueous alcohol, based on systematic adjustments in reagent concentrations and reaction conditions. Energy-dispersive X-ray (EDX) imaging by scanning electron microscopy (SEM) supports a heterogeneous distribution of Fe within MGNCs. The magnetization of the MGNCs can be as high as 6 emu g^{-1}, sufficient for their precipitation by handheld magnets to enable applications in biomolecular separations.

2. Materials and methods

All materials were obtained from commercial sources and used as received, unless otherwise noted. Deionized water was obtained from an ultrafiltration system (Milli-Q, Millipore, Temecula, CA, USA) with a measured resistivity above 18 MΩ·cm, and passed through a 0.22-μm filter to remove particulate matter. CS_2 was used as supplied and stored with minimum exposure to air.

Nanomaterials were characterized by transmission electron microscopy (TEM) using a Tecnai-T20 microscope (FEI, Hillsboro, OR, USA). TEM samples were prepared by floating carbon-coated grids on top of an aqueous NP dispersion for 30 min, followed by removal of the grid and drying in air for at least 60 min prior to analysis. Energy-dispersive X-ray (EDX) analysis by scanning transmission electron microscopy (STEM) was performed using a Tecnai G2 T20 microscope (FEI) equipped with a LaB6 filament and X-Max 80 silicon drift detector (Oxford, UK), with data collected by a high-angle annular dark field (HAADF) detector (Fischione, Export, PA, USA) and recorded by a 2 k × 2 k CCD imaging camera (Gatan, Pleasanton, CA, USA) using Inca software (ETAS, Stuttgart, Germany). Atomic absorption spectroscopy (AAS) was performed with a Perkin-Elmer (Waltham, MA, USA) 3110 spectrometer, using materials dissolved in aqua regia. Attenuated total reflectance-infrared (ATR-IR) analyses were performed on powder samples deposited on a ZnSe window, using a Nexus 670 spectrometer (Thermo, Waltham, MA, USA) flushed with N_2 to remove atmospheric CO_2 and moisture. Photoluminescence (PL) imaging was performed on air-dried samples with an Olympus (Tokyo, Japan) FV1000 laser scanning confocal microscope using a 10× confocal objective and 4.5× zoom lens, and three different laser lines with appropriate filters (excitation/emission = 488/505–525 nm; 543/560–620 nm; 635/655–755 nm).

Hydrodynamic size analysis of aqueous dispersions was performed by nanoparticle tracking analysis (NTA) using a Nanosight LM-10 (Malvern Instruments, Worcestershire, UK), with 405-nm laser excitation and distilled, particle-free water stored in polyethylene containers. Three tracking videos were collected per sample with a minimum of 2000 particle tracks per run, yielding hydrodynamic size (d_h) values based on mode peak analysis. Inductively coupled plasma mass spectrometry (ICP-MS) was performed at the University of Illinois. Magnetic properties were measured at room temperature on neat powders using a MPMS-3 magnetometer (Quantum Design, San Diego, CA, USA) in vibrating sample magnetometer mode, with applied magnetic fields up to 10 kOe, and calibrated with colloidal γ-Fe_2O_3 [31]. Extinction spectra were obtained using a Cary-50 visible-near infrared spectrophotometer (Varian, Palo Alto, CA, USA) in transmission mode.

2.1. Synthesis and modification of colloidal iron oxide

Colloidal iron oxide (Fe_3O_4) was prepared by co-precipitation, using 648 mg of $FeCl_3$ (4 mmol) and 398 mg of $FeCl_2$·4 H_2O (2 mmol) dissolved in 5 ml of deaerated, deionized water, added dropwise to 15 ml of a 28% NH_4OH solution over a period of 10 min in a glass test tube, while immersed in an ultrasonic cleaning bath. Colloidal Fe_3O_4 was formed immediately upon addition; care was taken to maintain anaerobic conditions during the dropwise addition of iron salts to the NH_4OH solution. The reaction mixture was then removed from the ultrasonic bath and agitated for 2 min by vortex mixing to generate a homogeneous dispersion. Colloidal Fe_3O_4 was precipitated by applying an external handheld magnet along the walls of the reaction tube, then redispersed in deionized water. This process was repeated several times to remove weakly magnetized colloidal oxides. Final weights of magnetically active materials were obtained after drying the precipitated colloids in an oven, but were otherwise used as freshly prepared dispersions at a concentration of 8 mg ml^{-1}.

To prepare mPEG-coated Fe_3O_4, 20 mg of 5-kDa mPEG-NH_2 was dissolved in 1 ml of dry, deaerated methanol (4 mM) and stirred for 10 min, treated with one equivalent of CS_2 (4 μmol) diluted in methanol and stirred for another 10 min, then treated with triethylamine (4 μmol) and stirred for 30 min at room temperature, resulting in mPEG-dithiocarbamate (DTC). Absorption spectroscopy confirmed DTC formation by the appearance of a doublet at 255 and 295 nm [32]. The freshly prepared mPEG-DTC solution was then combined with 1 ml of colloidal Fe_3O_4 dispersed in water (8 mg ml^{-1}) and incubated at room temperature for 1 h. Aliquots were removed and air-dried for analytical characterization, but otherwise used as-prepared in the next step.

2.2. Synthesis of magnetic gold nanoclusters (MGNCs)

A 0.25-ml aliquot of freshly prepared dispersion of mPEG-DTC-treated colloidal Fe_3O_4 (1 mg) was added to 4 ml of an aqueous solution of L-histidine (1 mg ml^{-1}), adjusted to pH 5–6 using 0.1 M HCl, then incubated at room temperature for 1 h. In a separate container, a 0.6-ml aliquot of 1% w/v $HAuCl_4$ solution was diluted with 14.8 ml deionized water, adjusted to pH 9–10 using 5 M NaOH, then combined with the colloidal Fe_3O_4–histidine solution with vortex mixing and allowed to sit for 20 min. The reaction mixture (now pH 8–9) was treated with 20 mM *N*-methylhydroxylamine (NMH) to initiate reduction, added in five 0.2-ml portions with mixing every 5 min, with a noticeable change in color by the third addition. MGNCs were generated in significant quantities after 2 h at room temperature, and fully formed after 12 h. The reaction gradually increased in acidity to a final range of pH 6–7.

As-produced MGNCs were separated by selective precipitation using a handheld NdFeB magnet producing linear field gradients of 1–3 kG cm^{-1}, followed 15–20 min later by decantation of magnetically unresponsive materials. The retentate was subjected to two more rounds of redispersion into water at twice the original volume with mild sonication, followed by magnetic precipitation, to yield MGNCs that were essentially devoid of non-magnetic gold NPs.

Excess Fe_3O_4 was removed from MGNCs by treating aqueous suspensions with a 0.5 M solution of diethanol-DTC in methanol (DE-DTC; final concentration 2 mM), prepared *in situ* from diethanolamine and CS_2 [32]. In a typical cleansing procedure, 20 µl of 0.5 M DE-DTC was added to 5 ml of redispersed MGNCs (O.D. 0.4), followed by vortex mixing and mild sonication for several seconds, incubation for 1 h at room temperature, then two rounds of magnetic precipitation and redispersion in water.

3. Results and discussion

The co-precipitation of iron salts (commonly referred to as the Massart synthesis) is one of the simplest and most cost-effective approaches for preparing colloidal Fe_3O_4 [33]. However, this method is known to be sensitive to multiple reaction parameters, and often produces colloidal Fe_3O_4 with a broad size polydispersity, making it less suitable for NP syntheses requiring strict size control. On the other hand, the Massart synthesis is ideal from the perspective of sustainable materials chemistry, as it generates no organic waste or toxic byproducts. In our hands, co-precipitation typically yielded polycrystalline aggregates of Fe_3O_4 with domain sizes of 5–6 nm, and we have found these to be a reliable feedstock in the preparation of magnetic gold nanoclusters.

Preliminary studies on the electroless deposition of Au onto colloidal Fe_3O_4 were inspired by the work of Gao and coworkers, who showed that metallization can be induced on surfaces coated with poly-L-histidine via hydroxylamine reduction under basic conditions [11]. We find that the amino acid L-histidine also facilitates the reduction of $HAuCl_4$ onto colloidal Fe_3O_4, but typically yields submicron composites in the absence of other surface-active agents (see below). After testing several different surface modifiers, we determined that treating colloidal Fe_3O_4 with mPEG-DTC (formed *in situ* from 5-kDa mPEG-NH_2 and CS_2 [34,35]) provided the best control in MGNC synthesis, with average cluster sizes close to 100 nm (Figure 1). Optical extinction spectroscopy indicated a broad plasmon resonance band with a maximum at 600 nm, but extending far into the near-infrared region. Previous electron diffraction analysis of MGNCs established the Au component to have an fcc structure [29].

TEM images reveal that the MGNCs are often accompanied by significant amounts of extraneous inorganic material, presumed to be residual iron oxide. To remove this we turned to water-soluble dithiocarbamates (DTCs), which are well known for their chelation of transition-metal ions [36], and for their chemisorption onto metal surfaces [32,37]. DTCs have an especially high affinity for Fe^{2+} and Fe^{3+}, suggesting utility as a digestive deferrating agent. This proved to be the case: treatment of as-prepared MGNC dispersions with DE-DTC, prepared *in situ* from a 2:1 mixture of diethanolamine and CS_2 in methanol, removed all visible oxide from the MGNC surfaces and also from solution (Figure 1(b)). DE-DTC treatment does not introduce any notable changes to the optical or magnetic properties of the final dispersions, indicating that the MGNCs are uncompromised by the cleansing step. Likewise, attenuated total reflectance infrared (ATR-IR) spectroscopy indicates essentially no difference between MGNCs before and after treatment with DE-DTC (Figure 2).

The MGNCs are isotropic with morphologies varying from roughened spheres to raspberry-like clusters, with the latter being most common. TEM analysis indicates a range of grain sizes within MGNCs between 8 and 25 nm; again, treatment with DE-DTC did not appear to have any significant impact on either MGNC morphology or grain size.

Earlier reports have shown that colloidal gold nanoparticles and nanoclusters can produce detectable levels of linear photoluminescence (PL) when excited at visible wavelengths, with emission intensities scaling roughly with particle volumes [38,41]. Analysis by laser scanning confocal microscopy (λ_{ex} 488 nm) yields a strong PL within the spectral window of 505–525 nm; however, no appreciable emissions are observed upon excitation at longer wavelengths (Figure 3). This is in accord with the reported mechanism for PL, which is produced by

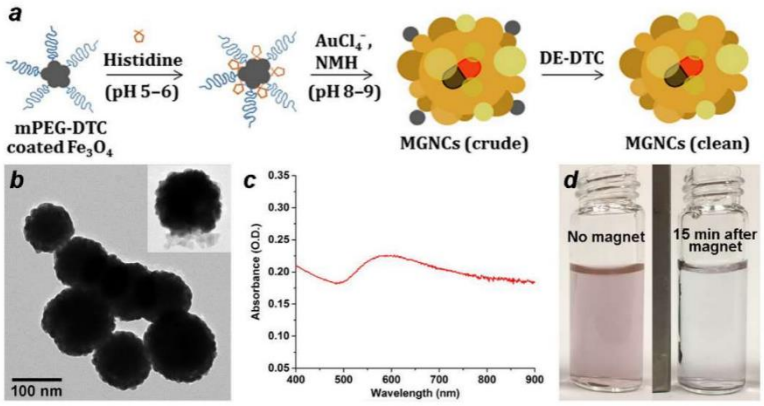

Figure 1. (a) Synthetic scheme for magnetic gold nanoclusters (MGNCs). (b) TEM image of clean MGNCs (*inset*: MGNC prior to DE-DTC treatment). (c) Optical extinction spectrum of MGNCs. (d) MGNCs before and after magnetic precipitation.

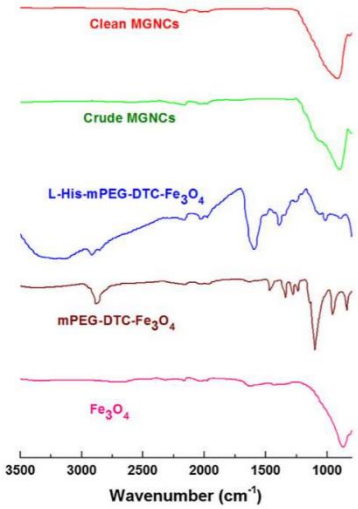

Figure 2. ATR-IR spectra acquired from pelleted samples after each step. Weak signals between 1900 and 2300 cm^{-1} are artifacts from instrumentation.

plasmon-enhanced emissions from excited *d*-band holes within gold nanostructures [38].

Control experiments illustrate the essential roles of both histidine and a peptizing agent for MGNC synthesis. Removal of either from the process results in the formation of small (10–12 nm) Au particles either loosely associated with iron-oxide nanoparticles, or embedded in a poorly dispersible oxide matrix (Figure 4). A weakly coordinating ligand such as histidine is necessary to encourage the adsorption of gold ions onto Fe_3O_4 surfaces, while a strongly anchored dispersant encourages the dissociation of iron-oxide particles from the parent aggregate. While the precise role of mPEG-DTC remains unclear, replacing it with low molecular-weight DTCs does not produce the desired MGNCs. We note that the reaction is sensitive to histidine concentration (0.2 g ml^{-1} after dilution); too much prevents the deposition of Au onto colloidal Fe_3O_4, resulting instead in smaller, non-magnetic NPs. The pH of the Fe_3O_4–histidine solution is also important, as histidine is cationic at pH 5–6 and can adsorb in that form onto Fe_3O_4 surfaces.

The MGNCs are responsive to field gradients produced by handheld NdFeB magnets, enabling their facile separation and decantation from magnetically inactive gold NPs within a 15–20 min period. The exact composition of the iron oxide is unknown but likely to be a mixture of Fe_3O_4 and γ-Fe_2O_3, the latter produced upon oxidation by Au ions. Several experiments were conducted to optimize the incorporation of Fe_xO_y in the MGNCs, in order to achieve higher magnetic moment. The mole ratio of gold to iron (Au/Fe) was varied to evaluate its effect on MGNC formation, size distribution, and magnetic response (Figure 5). A mole ratio of 6–9 produced MGNCs of relatively uniform size and shape, but lower Au/Fe ratios had variable effects on MGNC structures and also produced greater amounts of residual iron oxide, to the extent that their removal was problematic. Conversely, Au/Fe ratios well above 9 produce considerable amounts of non-magnetic colloidal Au (Figure 5(d)), which is readily determined by the residual reddish tint in solution after magnetic precipitation.

The effect of solution pH on MGNC formation was also evaluated at a fixed Au/Fe mole ratio of 9. Reductions performed under relatively acidic conditions (initial pH < 8) produces poorly dispersed MGNCs trapped in a matrix of amorphous iron oxide, whereas reactions performed at an initial pH of 8–9 produces

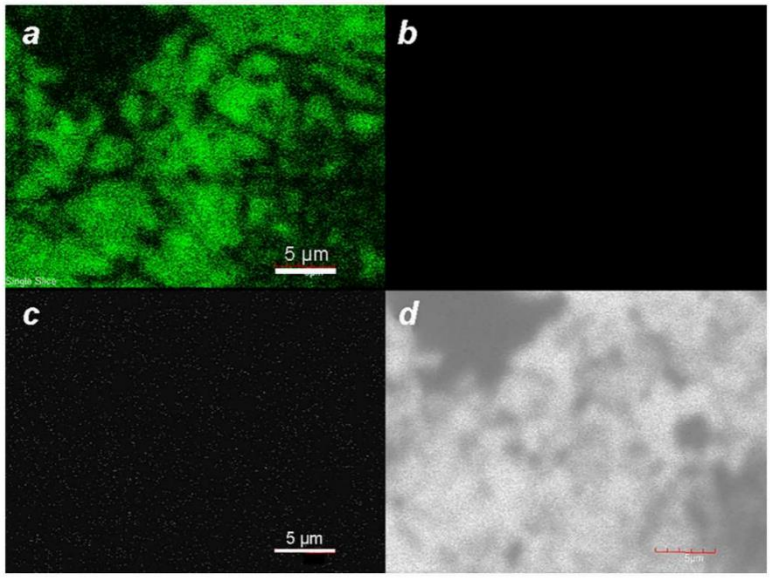

Figure 3. Laser scanning confocal fluorescence of MGNCs at different excitation wavelengths: (a) 488, (b) 546, (c) 647 nm. (d) Corresponding transmission image.

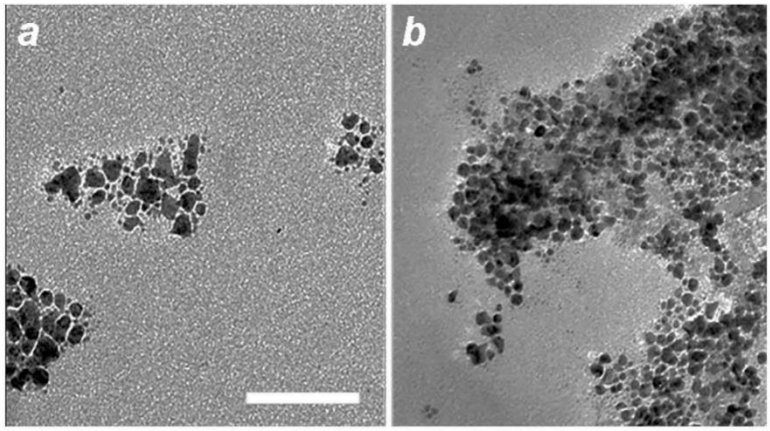

Figure 4. TEM images of (a) Au nanoparticles produced without L-histidine treatment of mPEG-DTC-coated Fe_3O_4 NPs; (b) aggregates produced without mPEG-DTC treatment of histidine-coated Fe_3O_4 NPs. Bar = 50 nm.

well-dispersed MGNCs with a narrower size and shape polydispersity (Figure 6). Reactions performed at pH > 9 generates very small particles and with poor dispersion stability.

All reactions up to this point were performed on a small (1–5 ml) scale for the systematic evaluation of reaction conditions. To determine whether the optimized MGNC synthesis could be reproduced on a larger scale, the reaction was performed in bigger tubes (ca. 20 ml final volume; see Materials and methods), which produced MGNCs very similar in size as those made on a 1–5 ml scale (Figure 7). The dry weight of MGNCs following removal of residual iron oxide (see below) was estimated to be 10 mg (42% yield). The reproducibility rate is 50%, which is acceptable given the heterogeneous nature of the colloidal Fe_3O_4 feedstock. Refinement

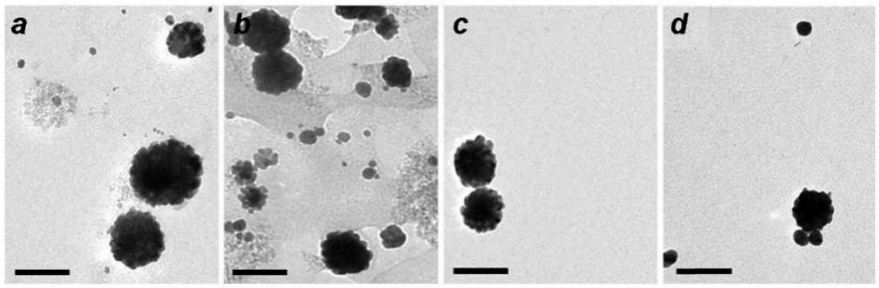

Figure 5. MGNCs prepared with different Au/Fe mole ratios: (a) 2; (b) 4; (c) 9; (d) 27. Bar = 100 nm.

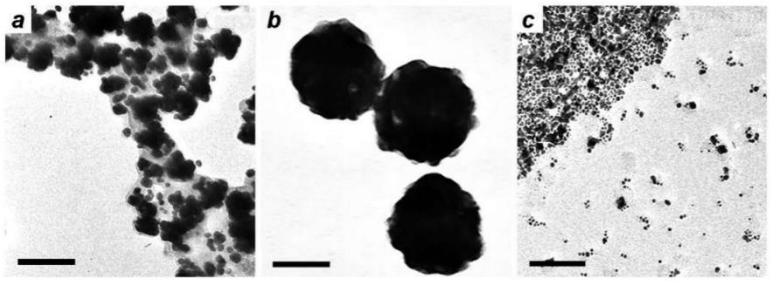

Figure 6. MGNCs synthesized using a fixed Au/Fe mole ratio of 9, with different initial pH values: (a) 6–8; (b) 8–9; (c) 9–10. Bar = 50 nm.

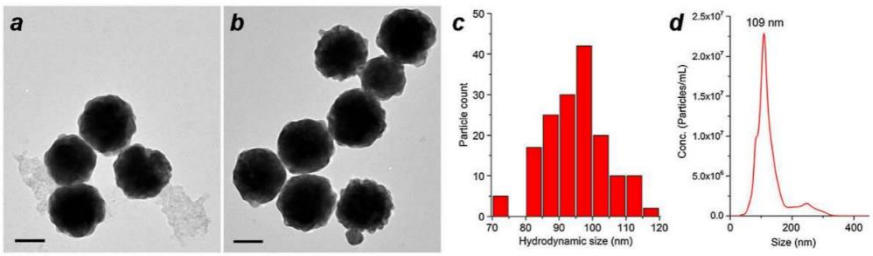

Figure 7. (a, b) TEM images of MGNCs prepared on a 20-ml scale, before and after cleansing with DE-DTC. (c) Size histogram of DTC-treated MGNCs by TEM image analysis (d_{av} = 95 nm). (d) Hydrodynamic analysis of MGNCs by NTA (d_h = 109 nm; standard error = 3 nm); Scale bar = 50 nm.

of co-precipitation conditions may further improve the reproducibility of Au deposition onto colloidal Fe_3O_4 surfaces.

The size distribution of DE-DTC-treated MGNCs prepared on a 20-ml scale was characterized by TEM image analysis ($d = 95 \pm 9$ nm; $N = 161$) and by nanoparticle tracking analysis (NTA; d_h from 3 runs = 109 nm). The size analysis outcomes are similar and validate the accuracy of the latter method, in accord with other studies showing similar matches between TEM and NTA [35,39].

Elemental analysis was performed using ICP-MS and AAS to determine the percentage and distribution of iron within the DTC-cleansed MGNCs. Despite an initial Au/Fe ratio of 9 in the reaction mixture, ICP-MS and AAS both show MGNCs to have much higher mole ratios (Au/Fe = 35.5 and 26.8, respectively), meaning that most of the starting Fe_3O_4 is not incorporated into the product. We presume that (a) the reduction of Au onto histidine-coated Fe_3O_4 is inefficient, relative to its autocatalytic deposition on Au islands formed subsequently, and (b) much iron oxide is lost by the speciation

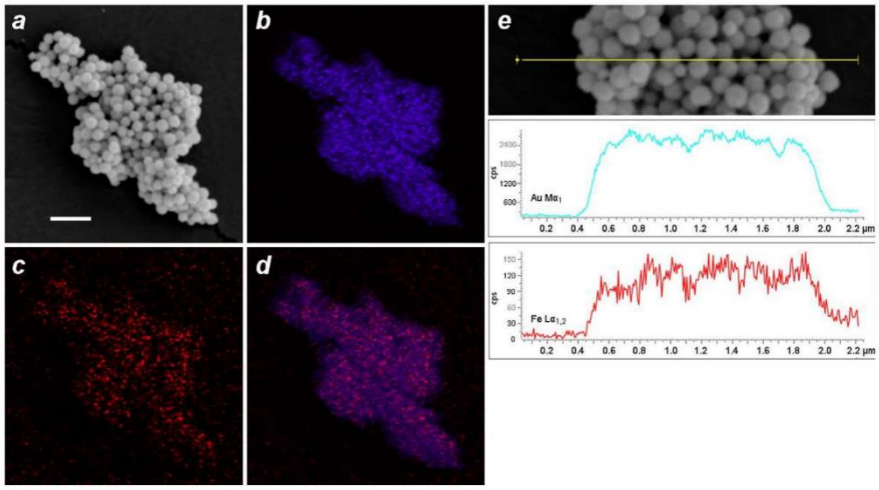

Figure 8. EDX–SEM data for DTC-cleansed MGNCs. (a) Backscattering image (bar = 500 nm), (b–d) elemental mapping for Au ($M\alpha_1$: 2,123 eV), Fe ($L\alpha_{1,2}$: 705 eV), and merged Au/Fe respectively. (e) Linescan across MGNCs, confirming the colocalization of Au and Fe.

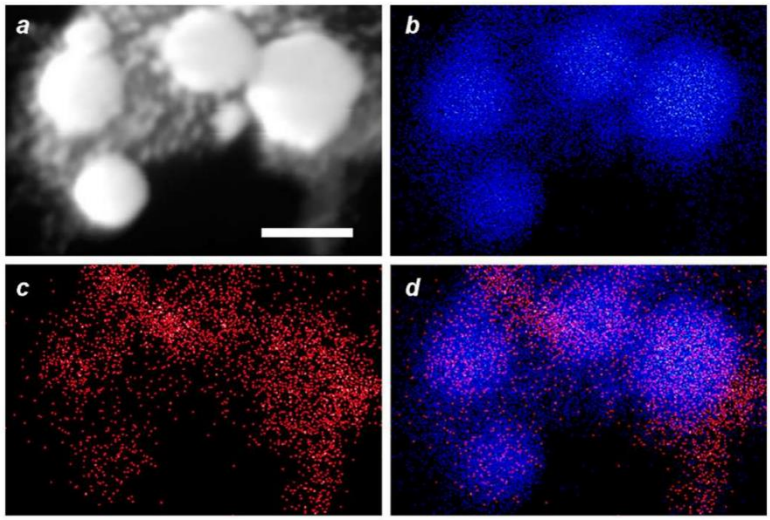

Figure 9. EDX data for MGNCs in HAADF–STEM mode, prior to cleansing by DE-DTC. (a) HAADF–STEM image (bar = 100 nm), (b–d) elemental maps for Au, Fe, and merged Au/Fe respectively. The distribution of Fe within MGNCs is relatively even.

of dissolved Fe upon addition of $AuCl_4$, which is a strong oxidant and a source of halide counterions.

EDX imaging was performed to determine the spatial distribution of Fe within the MGNCs. Low-resolution EDX–SEM imaging of MGNCs cleansed with DE-DTC confirmed colocalization of iron and gold within the MGNCs, but with a low content of Fe (Figure 8). To determine whether a core–shell morphology might be present, a higher resolution analysis was performed on individual MGNCs in HAADF–STEM mode, prior to DE-DTC cleaning (Figure 9). These images indicate a heterogeneous distribution of Fe with significant signal intensities within the MGNCs, but offer no evidence of a well-defined core-shell morphology.

We postulate that Fe_3O_4 is entrapped by the rapid growth and coalescence of Au domains, resulting in

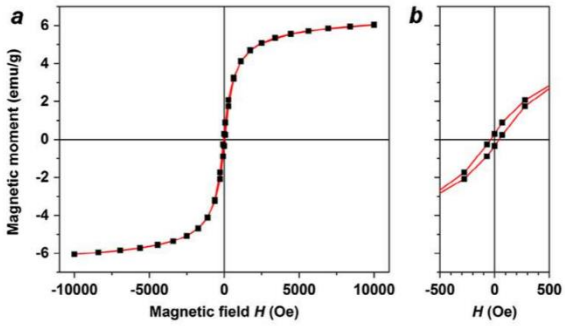

Figure 10. (a) Magnetization curve of MGNCs in powder form, taken at room temperature; (b) expansion of low-field region.

composite Au nanoparticles containing clusters or veins of superparamagnetic iron oxide. We note that a similar deposition mechanism has been described in the formation of Au–Fe_3O_4 'nanoroses', in which 5-nm Fe_3O_4 particles were used to nucleate the deposition and growth of Au clusters [22]. Interestingly, EDX analyses from that study were also unable to confirm the existence of well-defined iron-oxide cores.

Despite the low Fe concentration, the MGNCs have sufficient moment to respond to local field gradients produced by rare-earth magnets (Figure 1(d)). The magnetic properties of MGNCs were characterized in powder form using a superconducting quantum interference device (SQUID) in vibrating sample magnetometry mode, with a field sweep of ± 10 kOe. Several MGNC samples were measured, yielding saturation magnetization (M_S) values between 1.6 and 6.0 emu g^{-1} (Figure 10(a)). This variability in magnetization is to be expected, given the stochastic nature of Fe_3O_4 incorporation into the MGNCs during electroless deposition. On the one hand, this variability may limit the use of MGNCs in situations that require well-defined moment-to-mass ratios; on the other, many applications can tolerate a significant variation in magnetic moment, particularly those that require a magnetomotive function. It is worth mentioning that MGNCs are weakly ferromagnetic at room temperature, with H_C on the order of 35 Oe (Figure 10(b)). The source of coercivity in MGNCs remains to be determined; however, we note that remanent magnetization has been observed in other magnetic gold NPs, including those without any ferromagnetic elements [40].

4. Conclusions

A practical, eco-friendly synthesis of magnetic gold nanoclusters can be performed in aqueous alcohol without the use of harsh reagents, amphiphilic surfactants, or phase transfer from organic solvents. The final particles are produced with a narrow size distribution close to 100 nm, absorb strongly at NIR wavelengths, and can be collected within minutes using handheld magnets. EDX-SEM imaging supports the colocalization of Fe and Au within individual MGNCs. The MGNCs produce significant photoluminescence when excited at 488 nm. Lastly, ongoing studies have confirmed that MGNCs are highly biocompatible with cellular systems, and can thus be used to support a variety of bionanotechnology applications.

Disclosure statement

No potential conflict of interest was reported by the authors.

Funding

This work was supported by the Division of Civil, Mechanical and Manufacturing Innovation [grant number 1344654] and National Cancer Institute [grant number P30 CA023168].

ORCID

Alexander Wei http://orcid.org/0000-0002-8587-1037

References

[1] Mikhaylova M, Kim DK, Bobrysheva N, et al. Superparamagnetism of magnetite nanoparticles: dependence on surface modification. Langmuir. 2004;20:2472–2477.
[2] Wang LY, Luo J, Fan Q, et al. Monodispersed core-shell Fe_3O_4@Au nanoparticles. J Phys Chem B. 2005;109:21593–21601.
[3] Mandal M, Kundu S, Ghosh SK, et al. Magnetite nanoparticles with tunable gold or silver shell. J Colloid Interface Sci. 2005;286:187–194.
[4] Wang L, Bai J, Li Y, et al. Multifunctional nanoparticles displaying magnetization and near-IR absorption. Angew Chem Int Ed. 2008;47:2439–2442.
[5] Pal S, Morales M, Mukherjee P, et al. Synthesis and magnetic properties of gold coated iron oxide nanoparticles. J Appl Phys. 2009;105:07B504.
[6] Xu ZH, Li CX, Kang XJ, et al. Synthesis of a multifunctional nanocomposite with magnetic,

mesoporous, and near-IR absorption properties. J Phys Chem C. 2010;114:16343–16350.

[7] Lim JK, Majetich SA, Tilton RD. Stabilization of superparamagnetic Iron oxide core-gold shell nanoparticles in high ionic strength media. Langmuir. 2009;25:13384–13393.

[8] Smolensky ED, Neary MC, Zhou Y, et al. Fe_3O_4@ Organic@Au: core-Shell nanocomposites with high saturation magnetisation as magnetoplasmonic MRI contrast agents. Chem Commun. 2011;47:2149–2151.

[9] Dong W, Li Y, Niu D, et al. Facile synthesis of monodisperse superparamagnetic Fe3O4 Core@ Hybrid@Au shell nanocomposite for bimodal imaging and photothermal therapy. Adv Mater. 2011;23:5392–5397.

[10] Meledandri CJ, Stolarczyk JK, Brougham DF. Hierarchical gold-decorated magnetic nanoparticle clusters with controlled size. ACS Nano. 2011;5:1747–1755.

[11] Jin Y, Jia C, Huang S-W, et al. Multifunctional nanoparticles as coupled contrast agents. Nat Commun. 2010;1:41.

[12] Yu H, Chen M, Rice PM, et al. Dumbbell-like Bifunctional Au-Fe_3O_4 nanoparticles. Nano Lett. 2005;5:379–382.

[13] Wei Y, Klajn R, Pinchuk AO, et al. Synthesis, shape control, and optical properties of hybrid Au/Fe_3O_4 "Nanoflowers". Small. 2008;4:1635–1639.

[14] Levin CS, Hofmann C, Ali TA, et al. Magnetic–plasmonic core–shell nanoparticles. ACS Nano. 2009;3:1379–1388.

[15] Wei Q, Song H-M, Leonov AP, et al. Gyromagnetic imaging: dynamic optical contrast using gold nanostars with magnetic cores. J Am Chem Soc. 2009;131:9728–9734.

[16] Song H-M, Wei Q, Ong QK, et al. Plasmon-resonant nanoparticles and nanostars with magnetic cores: synthesis and magnetomotive imaging. ACS Nano. 2010;4:5163–5173.

[17] Kim C, Song H-M, Cai X, et al. *In Vivo* photoacoustic mapping of lymphatic systems with plasmon-resonant nanostars. J Mater Chem. 2011;21:2841–2844.

[18] Miao X, Wang T, Chai F, et al. A facile synthetic route for the preparation of gold nanostars with magnetic cores and their reusable nanohybrid catalytic properties. Nanoscale. 2011;3:1189–1194.

[19] Bhana S, Rai BK, Mishra SR, et al. Synthesis and properties of near infrared absorbing magneto-optical nanopins. Nanoscale. 2012;4:4939–4942.

[20] Aaron JS, Oh J, Larson TA, et al. Increased optical contrast in imaging of epidermal growth factor receptor using magnetically actuated Hybrid Gold/Iron Oxide nanoparticles. Opt Express. 2006;14:12930–12943.

[21] Park H-Y, Schadt MJ, Wang L, et al. Fabrication of magnetic core@shell Fe Oxide@Au nanoparticles for interfacial bioactivity and bio-separation. Langmuir. 2007;23:9050–9056.

[22] Ma LL, Feldman MD, Tam JM, et al. Small multifunctional nanoclusters (Nanoroses) for targeted cellular imaging and therapy. ACS Nano. 2009;3:2686–2696.

[23] Mohammad F, Balaji G, Weber A, et al. Influence of gold nanoshell on Hyperthermia of superparamagnetic Iron Oxide nanoparticles. J Phys Chem C. 2010;114:19194–19201.

[24] Xie H-Y, Zhen R, Wang B, et al. Fe_3o_4/Au core/shell nanoparticles modified with Ni^{2+}-Nitrilotriacetic acid specific to Histidine-tagged proteins. J Phys Chem C. 2010;114:4825–4830.

[25] Wang CG, Chen J, Talavage T, et al. Gold Nanorod/Fe_3O_4 nanoparticle "Nano-pearl-necklaces" for simultaneous targeting, dual-mode imaging, and photothermal ablation of cancer cells. Angew Chem Int Edit. 2009;48:2759–2763.

[26] Huang W-C, Tsai P-J, Chen Y-C. Multifunctional Fe_3O_4@Au nanoeggs as photothermal agents for selective killing of nosocomial and antibiotic-resistant bacteria. Small. 2009;5:51–56.

[27] Zhou X, Xu W, Wang Y, et al. Fabrication of cluster/shell Fe_3O_4/Au nanoparticles and application in protein detection via a SERS method. J Phys Chem C. 2010;114:19607–19613.

[28] Hu Y, Sun Y. Stable magnetic hot spots for simultaneous concentration and ultrasensitive surface-enhanced Raman scattering detection of solution analytes. J Phys Chem C. 2012;116:13329–13335.

[29] Kadasala NR, Wei A. Trace detection of tetrabromobisphenol A by SERS with DMAP-modified magnetic gold nanoclusters. Nanoscale. 2015;7:10931–10935.

[30] Kralisch D, Ott D, Gericke D. Rules and benefits of life cycle assessment in green chemical process and synthesis design: a tutorial review. Green Chem. 2015;17:123–145.

[31] Batis-Landoulsi H, Vergnon P. Magnetic moment of γ-Fe_2O_3 microcrystals: morphological and size effect. J Mater Sci. 1983;18:3399–3403.

[32] Zhu H, Coleman DM, Dehen CJ, et al. Assembly of Dithiocarbamate-anchored monolayers on gold surfaces in aqueous solutions. Langmuir. 2008;24:8660–8666.

[33] Massart R. Preparation of aqueous magnetic liquids in alkaline and acidic media. IEEE Trans Magn. 1981;17:1247–1248.

[34] Huff TB, Hansen MN, Zhao Y, et al. Controlling the cellular uptake of gold nanorods. Langmuir. 2007;23:1596–1599.

[35] Mehtala JG, Wei A. Nanometric resolution in the hydrodynamic size analysis of ligand-stabilized gold nanorods. Langmuir. 2014;30:13737–13743.

[36] Hogarth, G. Transition-metal dithiocarbamates: 1978-2003. In: Karlin KD, editor. Progress in Inorganic Chemistry. 53. New York: John Wiley and Sons; 2005. p. 71–561.

[37] Zhao Y, Pérez-Segarra W, Shi Q, et al. Dithiocarbamate assembly on gold. J Am Chem Soc. 2005;127:7328–7329.

[38] Dulkeith E, Niedereichholz T, Klar TA, et al. Plasmon emission in photoexcited gold nanoparticles. Phys Rev B. 2004;70:205424.

[39] Park J, Kadasala NR, Abouelmagd SA, et al. Polymer–iron oxide composite nanoparticles for EPR-independent drug delivery. Biomaterials. 2016;101:285–295.

[40] Nealon GL, Donnio B, Greget R, et al. Magnetism in gold nanoparticles. Nanoscale. 2012;4:5244–5258.

[41] Su YH, Tu S-L, Tseng S-W, et al. Influence of surface plasmon resonance on the emission intermittency of photoluminescence from gold nano-sea-urchins. Nanoscale. 2010;2:2639–2646.